# Anomalous Quartic Gauge Coupling for WWZ Production in an Effective Field Theory Framework

Narasimha Murthy Keshava Prasad Gubbi

Masterarbeit in Physik
angefertigt im Physikalischen Institut

vorgelegt der
Mathematisch-Naturwissenschaftlichen Fakultät
der
Rheinischen Friedrich-Wilhelms-Universität
Bonn

April 2019

I hereby declare that this thesis was formulated by myself and that no sources or tools other than those cited were used.

Bonn, . . . . . . . . . . . . . . . . . . . . . . . . . . . . . . . . . . . . . . . . . . . . . . . . . . . . .
Date Signature

1. Referee: Priv. Doz. Dr. Markus Cristinziani
2. Referee: Prof. Dr. Jochen Dingfelder

Dear Amma,
This work is dedicated to you.
Thank you for believing in me, supporting me and being the amazing person that you are.
Dedicated with Love.

# Abstract

This thesis presents a phenomenological study of the production of *WWZ* events through the inclusion of Anomalous Quartic Gauge Coupling (aQGC) operators. Triboson production studies can test the non-Abelian gauge structure of the Standard Model (SM); possible deviations from the SM predictions would provide hints of new physics at higher energy scales. In certain models with higher dimensional Effective Field Theory (EFT) operators, these couplings can be modified, leading to a significant enhancement of WWZ production cross section. Samples with these operators are generated and checked for deviations in the cross section with respect to SM predictions. The impact of aQGC operators for the production of *WWZ* events is studied in the three lepton channel and discriminating observables are identified.

# Acknowledgements

I would like to thank my supervisor, Priv. Doz. Dr. Markus Cristinziani for providing me the opportunity to carry out my master thesis under his tutelage, in the ERC TopCoup group, Physikalisches Institut, University of Bonn, Germany. The encouragement and guidance provided by him has helped me immensely at different stages of my thesis and also helped maintain a steady working pace, without going astray. I would also like to thank Prof. J. Dingfelder for agreeing to be the second evaluator of my thesis.

I would like to thank all the group members: Andrea, Carlo, Oğul, Sebastian, Vadim and Arshia for a pleasant and helpful working environment in the group. My special thanks are due to Andrea for patiently guiding me in the initial few months of the thesis; I shall cherish his friendship for a long time. My thanks are also due to Sebastian, for the time and effort taken in reviewing this thesis. It is definitely a much better version now due to his numerous comments and suggestions.

I would like to mention the contributions of my close friend Saba Zia Hassan, who always managed to bring a smile in me and has been an immense source of care and helped me through numerous low moments during the time spent in Germany. Another special person deserving mention is Vasanth, whose friendship has meant a lot to me and has always believed in me and is my closest confidant. I shall remember fondly all the times we spent together.

Lastly, but definitely not in the least measure, I would like to thank my parents who have supported me in my desire to study physics in Germany, despite immense amount of personal hardship, sickness and sacrifices. I owe to deep debt of gratitude for their love, care and support.

# Contents

# CHAPTER 1

# Introduction

> I shall be telling this with a sigh
> Somewhere ages and ages hence:
> Two roads diverged in a wood, and I—
> I took the one less traveled by,
> And that has made all the difference
>
> *"The Road Not Taken" by Robert Frost [1]*

Similar to the proverbial less-traveled path chosen by Frost, this study as part of the Master Thesis is the culmination of saga over the past few years across all aspects of my life – emotional, personal and professional. It is the first step (albeit a small one) towards the desire to study physics and contribute as a researcher in the quest to understand how the universe works and to answer the question : "What is the universe made of?".

The quest to comprehend the mysterious universe is an ancient one, from the times of Aryabhatta [2], and has continued over the past two millennia. The progress has been accumulated in systematic and incremental steps, and has led to the development of "The Standard Model (SM) of Particle Physics" [3]. It is a theory (and has been confirmed through experimental evidences) that describes the forces and their interactions in our universe, although gravity has not yet been incorporated in the Standard Model.

The massive vector bosons are the mediators of the weak interactions, and form the focus of this study. They be either charged ($W^{\pm}$) or neutral ($Z^0$), and are associated with several important processes of the SM, and are the focus of active research till this day. The production of three such bosons is predicted by the SM and the evidence for massive tri-boson production was obtained recently [4] with a statistical significance $4\sigma$ standard deviations.

There have been numerous theoretical and experimental efforts in the past three decades, to search for new physics beyond the predictions of the Standard Model. The numerous observables in the Standard Model can be probed for deviations, to search for indications of new physics. The operators of the Effective Field Theory can be used to interpret the deviations from Standard Model predictions, with the coupling constants being free parameters of an effective theory.

The objective of this thesis was to perform a phenomenological study to understand the impact of anomalous Quartic Gauge Coupling operators for the production of $WWZ$ bosons at tree level. The conclusions and insights gained from this study will be useful for future experimental analyses of

Quartic Gauge Coupling operators.

The chapters of the thesis are organized as follows: the theoretical underpinnings of self-coupling of weak bosons and the utility of probing for new physics in the Effective Field Theory framework is provided in Chapter 2. The procedure of producing *WWZ* events at generator level and probe for deviations in cross sections of operators is described in Chapter 3. The selection of events, reconstruction of boson candidates, probing the validity of EFT models at different energy scales and identification of discriminating variables is described in Chapter 4. Lastly, a number of additional figures for different operators has been included in the Appendix.

CHAPTER **2**

# Standard Model of Particle Physics and Beyond

This chapter describes the theoretical underpinnings for the phenomenological study performed in this thesis. It begins with a description of the Standard Model (SM) of Particle Physics in Section 2.1. The need for precision tests of the SM is outlined in Section 2.2. The Effective Field Theory (EFT) and the Anomalous Quartic Gauge Coupling (aQGC) operators as detailed in Section 2.3. Lastly, theoretical considerations for probing the validity of EFT is described in Section 2.4.

The work presented in this thesis represents an effort towards probing this theory, by means of simulating events of aQGC operators for WWZ production and analyzing the impact of these operators. Throughout this chapter, natural units are employed, wherein the speed of light in vacuum ($c$) and the reduced Planck constant ($\hbar$) are both set to $c = \hbar = 1$.

## 2.1 The Standard Model of Particle Physics

The current understanding of nature, i.e., the nature of elementary particles and their fundamental interactions has been encapsulated into an all encompassing theory called Standard Model of Particle Physics. The SM has been developed and expanded over the past eight decades, and has been continually tested experimentally to unprecedented levels of precision. It is the most successful theory built to date, describing three out of four forces found in nature. There are four fundamental forces in nature : Electromagnetism, Strong, Weak and Gravity. The SM describes phenomena related to all other forces, except for gravity.

### 2.1.1 Dramatis Particulae

Just as the section of “Dramatis Personae” would introduce the characters of Shakespeare’s plays, the section on leading characters or “Dramatis Particula”, introduces elementary particles that constitute the fundamental building blocks of nature. A diagrammatic representation of the SM and its important constituents is shown in Figure 2.1. The three main properties of a given particle are: mass, charge and spin. A detailed list of all particles that have been experimentally observed so far and their respective quantum numbers can be found in Reference [5].

The matter-component of the universe broadly classifies the zoo of particles based on spin of the particles, with either integer or half-integer spins. The family of particles with integer spins obeying Bose-Einstein statistics are referred to as "Bosons" while the other family of particles with half-integer spins obeying Fermi-Dirac statistics are referred to as "Fermions".

The building-blocks of the universe are composed of three generations (or families) of both, quarks and leptons (which are both fermions). Every fermion (with spin-$\frac{1}{2}$), has its corresponding anti-particle with opposite charge. A single lepton family unit consists of a charged lepton (unit charge) and its corresponding neutrino. There are three generations of lepton families: "electrons", "muons" and "tauons" are the three charged leptons along with their associated neutrinos. There are also three families of quarks with a total of 18 of them, with fractional charges. These quarks are of six flavors ("up", "down", "strange", "charm", "bottom", and "top") with three colors ("red", "green" and "blue"). The colors are labels of charge for strong interactions, analogous to the electric charge of electromagnetic interactions.

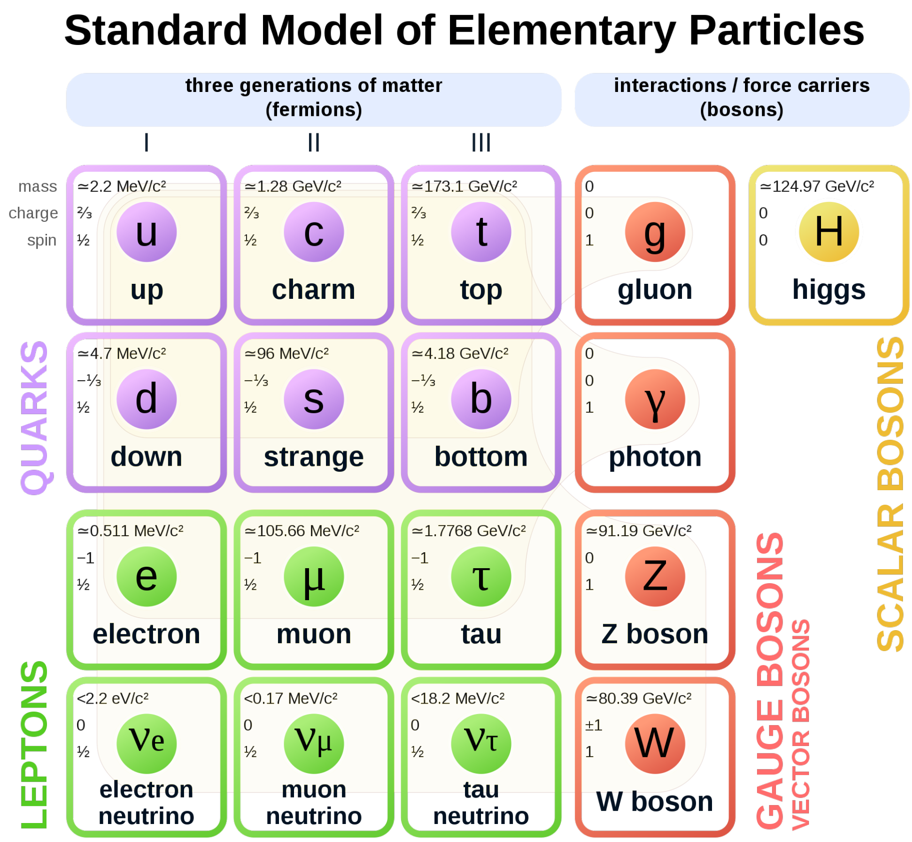


Figure 2.1: Representation of the Standard Model of Particle Physics. Image Source: [6]

Fermions interact via the exchange of force-carrying particles (mediators), called "gauge bosons". These gauge bosons are particles with integer spins (with spin-1 and hence termed as "vector bosons") and can be either massless or massive. The photon ($\gamma$) and gluon (g) are massless mediators of the electro-magnetic and strong forces respectively, while the charged $W$ and neutral $Z$ bosons are the massive gauge bosons mediating weak interactions. The scalar (spin-0) Higgs field, is responsible for providing mass through the "Spontaneous Symmetry Breaking (SSB)" mechanism and also ensures that the SM remains locally gauge invariant.

The SM is a renormalizable Quantum Field Theory (QFT), and typically a QFT is expressed in terms of the Lagrangian formalism. A detailed description of renormalizable theories is beyond the scope of this thesis. A comprehensive explanation of QFT, renormalization and other conceptual details related to it can be found in many excellent textbooks on SM and QFT. For a theoretical treatment on QFT, one can refer to books by Peskin [7], Schwartz [8], while Thomson [3] and Halzen and Martin [9] focus on the phenomenological and experimental aspects of the SM.

It would suffice to understand that the mass dimension for any term in the Lagrangian (composed of fields and derivatives), must be less than or equal to four. Any term with mass dimension greater than four, would render the theory to be non-renormalizable. A very short overview of the Lagrangian formalism and QFT is provided in the following section.

### 2.1.2 Lagrangian Formalism of Quantum Field Theory

The Lagrangian formalism in QFT is borrowed from its classical analogue wherein the two major quantities, namely the action $S$ and the Lagrangian density $\mathcal{L}$, contain the complete information about the system being studied. In classical mechanics, a system is studied as a single localised particle endowed with finite degrees of freedom. However, in quantum mechanics this concept is extended into a wave function and further extended to the concept of a "field" in quantum field theories. The state of a quantum mechanical system is described by a wave function $\psi(x)$, whereas in QFT the particles are defined to be excitations of these local fields $\phi(x)$, where 'x' refers to four dimensional space-time coordinates.

The Lagrangian density, just as in classical field theory, is a function of fields and its space-time derivatives (maximum up to $2^{nd}$ order) and describes the properties and interactions among the various fields $\phi_i(x)$:

$$\mathcal{L}(x) = \mathcal{L}(\phi_i, \partial_\mu \phi_i)(x). \tag{2.1}$$

The action $S$ [9] is then defined to be the integral over all spatial and temporal dimensions of $\mathcal{L}$ :

$$S = \int \left( d^4x \, \mathcal{L}(\phi_i(x), \partial_\mu \phi_i(x)) \right). \tag{2.2}$$

Applying the principle of least action, results in the system evolving along a path for which the action is stationary:

$$\delta S = \delta \left( \int d^4x \mathcal{L} \left( \phi_i(x), \partial_\mu \phi_i(x) \right) \right) = 0. \tag{2.3}$$

For an action that is varied extremally (includes both maxima and minima), and its field variations with fixed boundaries, the Euler-Lagrange differential equations are obtained:

$$\partial_\mu \left( \frac{\partial \mathcal{L}}{\partial(\partial_\mu \phi_i(x))} \right) = \frac{\partial \mathcal{L}}{\partial \phi_i(x)}. \tag{2.4}$$

The Euler-Lagrange equations enable to obtain the Equations of Motion (EOM) for a given system.

Using Noether's Theorem [3], one can obtain the current $J^\mu$ for a general set of fields $\phi_i(x)$ given by

$$J^\mu = \sum_i \partial_\mu \left( \frac{\partial \mathcal{L}}{\partial(\partial_\mu \phi_i(x))} \right) \phi_i(x) - X^\mu. \tag{2.5}$$

where the conserved physical quantities, defined as Noether currents, are conserved ($\partial_\mu J^\mu = 0$).

### 2.1.3 Quantum Electrodynamics

Quantum Electrodynamics (QED) is one of the stellar achievements in the past century, and has been experimentally verified up to extraordinary levels of precision. It is a field theory describing the interaction between light and matter. The Lagrangian for a free, fermionic field $\psi(x)$ of mass $m$ is given by the Dirac Lagrangian:

$$\mathcal{L} = \bar{\psi}(i\partial\!\!\!/ - m)\psi. \tag{2.6}$$

where $\bar{\psi} = \psi^\dagger \gamma^0$ is the adjoint Dirac spinor, $\partial\!\!\!/ = \gamma^\mu \partial_\mu$ as per Feynman slash notation, $\gamma^\mu$ are the 4×4 Dirac matrices that satisfies the Clifford algebra $\left[\gamma^\mu, \gamma^\nu\right] = \gamma^\mu\gamma^\nu + \gamma^\nu\gamma^\mu = 2g^{\mu\nu}$ and $g^{\mu\nu}$ is the metric tensor for Minkowski spacetime. The Euler-Lagrange equation in 2.5, when applied to 2.6, represents the Dirac equation $(i\partial\!\!\!/ - m)\psi = 0$, the relativistic wave equation for all fermionic fields with mass $m$.

The fermionic Lagrangian density in 2.6, respects the $U(1)$ global gauge symmetry, where $\alpha$ is constant (and therefore the phase is space-time independent).

$$\psi(x) \to \psi'(x) = U\psi(x) = \exp{(i\alpha)}\psi. \tag{2.7}$$

Under local gauge transformations, the phase is space-time dependent with '$\alpha = \alpha(x)$', the Lagrangian density of equation 2.6 is not invariant under local gauge transformation as reproduced here,

$$\mathcal{L} \to \mathcal{L}' = \mathcal{L} + \bar{\psi}\gamma_\mu\psi(\partial^\mu\alpha). \tag{2.8}$$

The additional term is due to the fact that the space-time derivatives are not invariant under a local gauge transformation. In order to overcome this lacuna, a "gauge field" ($A_\mu$) is introduced such that it transforms as:

$$A_\mu \to A'_\mu = A_\mu + \frac{1}{e}\partial_\mu\alpha, \tag{2.9}$$

and the space-time derivative is extended to a covariant derivative , through minimal coupling with electric charge $e$ and is defined as:

$$D_\mu \equiv \partial_\mu - ieA_\mu. \tag{2.10}$$

Equation 2.6 is now replaced by a local-gauge invariant Lagrangian given by

$$\mathcal{L}_{Dirac} = \bar{\psi}(iD\!\!\!\!/ - m)\psi. \tag{2.11}$$

Therefore, the principle of local gauge invariance ensures that there is a natural emergence of coupling between the fermionic field $\psi(x)$ and the gauge field $A_\mu(x)$. The EM stress tensor, defined as

$$F^{\mu\nu} \equiv \partial^\mu A^\nu - \partial^\nu A^\mu. \tag{2.12}$$

is invariant under the transformation of the gauge field in equation 2.9. The Lagrangian for free gauge field in Equation 2.13 is also locally gauge invariant. It is to be noted that the mass term for the gauge field is not locally gauge invariant, and hence its mass has been set to $m = 0$.

$$\mathcal{L}_{EM} = -\frac{1}{4}F_{\mu\nu}F^{\mu\nu}. \tag{2.13}$$

By combining the invariant Lagrangians for both, the fermion field and the gauge field, the QED Lagrangian ($\mathcal{L}_{QED}$) reads as follows:

$$\mathcal{L}_{QED} = \bar{\psi}(i\not{D} - m)\psi - \frac{1}{4}F_{\mu\nu}F^{\mu\nu}. \tag{2.14}$$

Unlike QED whose generators commute and such class of theories are referred to as Abelian, a theory wherein the generators of the gauge group do not commute is referred to as non-Abelian gauge theory. Quantum Chromodynamics (QCD) and Electro Weak (EW) theories are non-Abelian in nature. For a more detailed treatment on non-Abelian theories in general and QCD and EW theories in particular can be found in reference [3].

### 2.1.4 Gauge Theory of Electro-Weak Interactions

The Glashow-Salam-Weinberg (GSW) model [10, 11, 12] of EW interactions, also known as *Standard Model of Particle Physics* is a gauge theory that unifies electromagnetic and weak forces.

The electromagnetic processes and weak charged current, unified through the EW theory describes the invariance of $U(1)_Y$ hypercharge and $SU(2)_L$ weak isospin transformations. Based on helicity, fermion fields can be either left-handed ($\psi_L \equiv \frac{1}{2}(1-\gamma_5)$) or right-handed ($\psi_R \equiv \frac{1}{2}(1+\gamma_5)$), where $\gamma_5 = i\gamma^0\gamma^1\gamma^2\gamma^3$ is the helicity operator. These are also called to as "left-chiral" and "right-chiral" fields. The left-chiral fields are doublets with isospin $I = \frac{1}{2}$, while right-chiral fields are singlets with isospin $I = 0$.

Every fermion field can be broken up into left-chiral and a right-chiral part,

$$\psi = \psi_R + \psi_L. \tag{2.15}$$

Therefore, the fermion mass term leads to mixing of left-handed and right-handed fields:

$$\bar{\psi}\psi = \bar{\psi}_L\psi_R + \bar{\psi}_R\psi_L. \tag{2.16}$$

However, electromagnetic vector current does not mix these components,

$$\bar{\psi}\gamma^\mu\psi = \bar{\psi}_R\gamma^\mu\psi_R + \bar{\psi}_L\gamma^\mu\psi_L, \tag{2.17}$$

and by utilizing the helicity operator, one can express the vector-axial (V-A) weak current as,

$$\bar{\psi}_L\gamma^\mu\psi_L = \frac{1}{2}\bar{\psi}\gamma^\mu(1-\gamma_5)\psi. \tag{2.18}$$

thereby leading to the conclusion that only left-chiral fields participate in weak interactions.

The SU(2) transformation of left-handed doublets results in $\psi_L$ being transformed as

$$\psi_L \rightarrow e^{i\beta^a(x)\frac{\tau^a}{2}}\psi_L, \tag{2.19}$$

where $a = 1, 2, 3$ and $\frac{\tau^a}{2}$ are the SU(2) generators. Furthermore, $U(1)_Y$ transformations on $\psi_L$ and $\psi_R$ results in them being changed by a phase factor $e^{i\alpha^a(x)\frac{Y}{2}}$.

The gauge group candidate chosen for EW theory is $SU(2) \otimes U(1)_Y$. The theory requires one gauge field per generator in order to be gauge invariant, and hence the following new gauge fields are introduced: three gauge fields associated with$SU(2)_L$ represented by, $W^i_\mu$, and one gauge field associated with $U(1)_Y$ represented by, $B_\mu$. The coupling constants, $g$ and $g^{'}$ for $SU(2)_L$ and $U(1)_Y$ respectively, are introduced through the covariant derivative $D_\mu \equiv \left(\partial_\mu - igW^j_\mu\frac{\sigma^j}{2} - \frac{i}{2}g'B_\mu\right)$. It is necessary to introduce covariant derivatives in order to preserve gauge invariance.

The field strength tensors for the EW theory are defined as follows: $W_{\mu\nu}$ is the $SU(2)_L$ second rank field strength tensor given by

$$W^i_{\mu\nu} \equiv \partial_\mu W^i_\nu - \partial_\nu W^i_\mu + g\epsilon^{ijk}W^j_\mu W^k_\nu, \tag{2.20}$$

$B_{\mu\nu}$ is the tensor for $U(1)_Y$

$$B_{\mu\nu} \equiv \partial_\mu B_\nu - \partial_\nu B_\mu. \tag{2.21}$$

The free Lagrangian for gauge fields can be written as

$$\mathcal{L}_{\text{gauge}} = -\frac{1}{4}W^i_{\mu\nu}W^{i\mu\nu} - \frac{1}{4}B_{\mu\nu}B^{\mu\nu}. \tag{2.22}$$

The fermion-gauge interaction term is described by,

$$\mathcal{L}_{int} = -\bar{\psi}_L\gamma^\mu\left(\frac{g}{2}\tau^a W^a_\mu + \frac{g^{'}}{2}YB_\mu\right)\psi_L - \bar{\psi}_R\gamma^\mu\frac{g}{2}YB_\mu\psi_R. \tag{2.23}$$

The first term in the equation 2.23, involving $W^1_\mu$ and $W^2_\mu$ can be written as:

$$-\frac{g}{2}\bar{\psi}_L\gamma^\mu\begin{pmatrix} 0 & W^1_\mu - iW^2_\mu \\ W^1_\mu + iW^2_\mu & 0 \end{pmatrix}\psi_L, \tag{2.24}$$

and therefore leads to the conclusion that charged physical gauge bosons can be defined as $W^\pm_\mu \equiv \frac{1}{\sqrt{2}}(W^1_\mu \mp iW^2_\mu)$. A rotation needs to be performed on neutral fields in order to find the correct set of gauge fields that can combine with electromagnetic current.

$$\begin{pmatrix} A_\mu \\ Z_\mu \end{pmatrix} = \begin{pmatrix} cos\theta_w & sin\theta_w \\ -sin\theta_w & cos\theta_w \end{pmatrix}\begin{pmatrix} B_\mu \\ W^3_\mu \end{pmatrix} \tag{2.25}$$

Here, $\theta_w$ is the Weinberg angle and is related to the SU(2) and $U(1)_Y$ coupling constants through the relations:

$$sin\theta_w = \frac{g'}{\sqrt{(g^2 + g'^2)}}, \tag{2.26}$$

and

$$cos\theta_w = \frac{g}{\sqrt{(g^2 + g'^2)}}. \tag{2.27}$$

Through the second term in the equation 2.23, the electromagnetic charge of the neutral current is obtained, i.e, $e = gsin\theta_w = g'cos\theta_w$. The fermions and four gauge bosons, briefly outlined in the EW theory so far are massless. An elaborate treatment of EW theory and the mechanism of spontaneous symmetry breaking (SSB) by which these massless bosons and fermions acquire mass can be referred to in the book by Thomson [3].

### Triple & Quartic Gauge Couplings

The free Lagrangian of gauge bosons in Equation 2.22 results in self-coupling between massive vector bosons, termed as the Triple Gauge Coupling (TGC) and Quartic Gauge Coupling (QGC) processes. It is a direct result of the fact that the gauge EW theory (and thereby the SM itself) is non-Abelian. The interaction term of the gauge boson Lagrangian is given by

$$\mathcal{L}_{\text{gauge,int}} = -\frac{g}{2}\epsilon^{ijk}(\partial_\mu W^i_\nu - \partial_\nu W^i_\mu)W^{j\mu}W^{k\nu} - \frac{g^2}{4}\epsilon^{ijk}\epsilon^{ilm}W^j_\mu W^k_\nu W^{l\mu}W^{m\nu}, \tag{2.28}$$

where the first term leads to triple gauge coupling and the second term leads to quartic gauge coupling among the vector bosons of SM. The self-coupling terms are expanded in terms of their constituent gauge fields, for TGC:

$$\begin{aligned}\mathcal{L}_{\text{TGC}} =& + ie\text{cot}\theta_W[(\partial_\mu W^-_\nu - \partial_\nu W^-_\mu)W^{+\mu}Z^\nu - (\partial_\mu W^+_\nu - \partial_\nu W^+_\mu)W^{-\mu}Z^\nu] \\ & + ie\text{cot}\theta_W W^-_\mu W^+_\nu(\partial^\mu Z^\nu - \partial^\nu Z^\mu) \\ & + ie[(\partial_\mu W^-_\nu - \partial_\nu W^-_\mu)W^{+\mu}A^\nu - (\partial_\mu W^+_\nu - \partial_\nu W^+_\mu)W^{-\mu}A^\nu + W^-_\mu W^+_\nu(\partial^\mu A^\nu - \partial^\nu A^\mu)]\end{aligned} \tag{2.29}$$

and for QGC is as follows:

$$\begin{aligned}\mathcal{L}_{\text{QGC}} =& -\frac{e^2}{2\text{sin}^2\theta_W}\left[(W^+_\mu W^{-\mu})^2 - W^+_\mu W^{+\mu}W^-_\nu W^{-\nu}\right] \\ & - e^2\text{cot}^2\theta_W\left[W^+_\mu W^{-\mu}Z_\nu Z^\mu - W^+_\mu Z^\mu W^-_\nu Z^\nu\right] \\ & - e^2\text{cot}^2\theta_W\left[2W^+_\mu W^{-\mu}Z_\nu A^\mu - W^+_\mu Z^\mu W^-_\nu A^\nu - W^+_\mu A^\mu W^-_\nu Z^\nu\right] \\ & - e^2\left[W^+_\mu W^{-\mu}A_\nu A^\nu - W^+_\mu A^\mu W^-_\nu A^\nu\right].\end{aligned} \tag{2.30}$$

The Feynman diagrams representing the TGC and QGC of the EW gauge bosons are shown in Figure 2.2. Recently, ATLAS obtained evidence for the production of three massive vector bosons [4] with $4\sigma$ standard deviations. A detailed account can be accessed in References [13], [4], [14], [15].

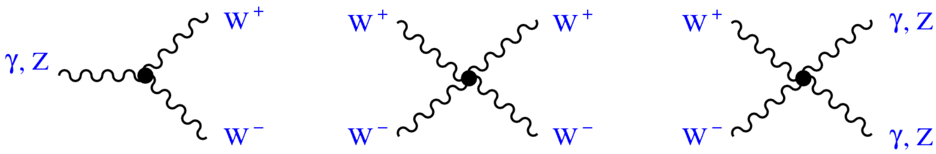


Figure 2.2: Feynman diagrams for the self-couplings of electroweak gauge bosons. Image source: [16]

### 2.1.5 The Standard Model

The Standard Model of particle physics unifies electromagnetic and weak forces into a single electroweak theory and also accounts for interactions of the strong force, thereby providing a description of the interactions of the matter component of the universe. It is also true that the SM is the most accurate and successful theory developed so far in the quest for a complete description of the universe and also has been tested to high levels of precision [5].

The SM Lagrangian, is a combination of a number of fields interacting through rules based on symmetry principles and is part of the Quantum Field Theory framework. It is expressed, in Lagrangian formalism, as:

$$\mathcal{L}_{SM} = -\frac{1}{4}F_{\mu\nu}F^{\mu\nu} + i\bar{\psi}\not{D}\psi + h.c. + \bar{\psi}_i y_{ij}\psi_j\phi + h.c. + |D_\mu\phi|^2 - V(\phi). \tag{2.31}$$

It is incredible that these set of elegant equations, describing the known interactions of the matter in

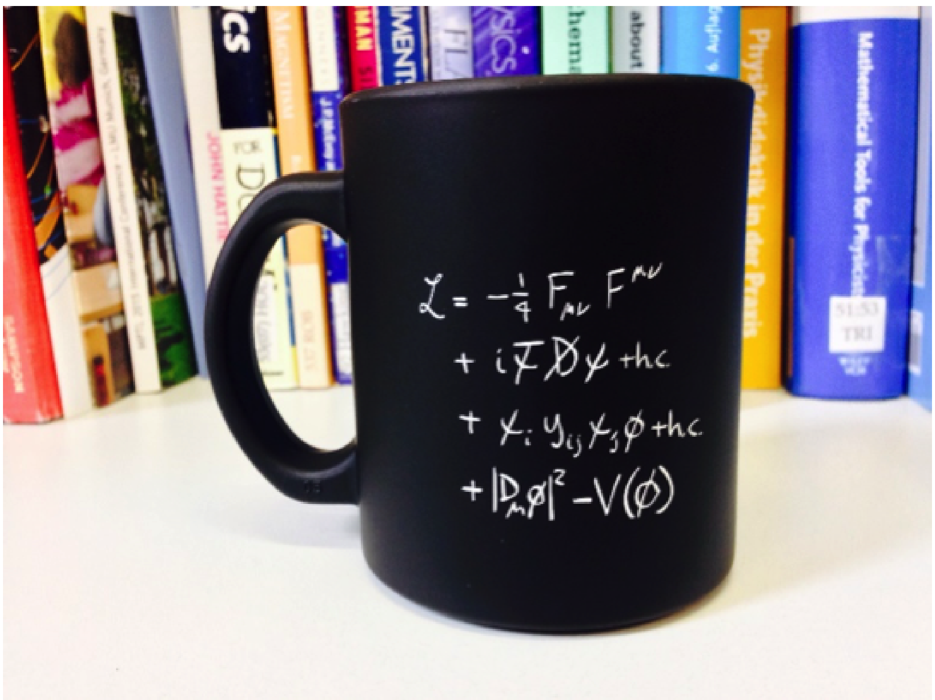

Figure 2.3: The Lagrangian of the SM, succinctly displayed on a coffee mug. Image source: [17]

the universe (the Lagrangian of the Standard Model $\mathcal{L}_{SM}$), can be encapsulated into a single equation that can fit on a coffee mug as displayed in Figure 2.3. However, this crisp and simplified version is rather misleading as it conveniently hides all the gory details. Upon expansion, the full $\mathcal{L}_{SM}$ in terms of its fields and couplings, involves a large number of terms and is both ugly and confusing.

Yet, it is quite clear from multiple instances of unexplained experimental evidence and numerous theoretical considerations that SM is still an incomplete theory and that would be subsumed at some higher energy scale as part of a larger theory. This is confirmed by experimental evidences like non-zero neutrino masses, the baryon asymmetry of the Universe and the existence of Dark Matter (DM), which cannot be explained by the SM. On the theory side, there exists a whole list of arguments pointing in this same direction. For a detailed account on SM being an incomplete theory, refer to References [5], [18] and Chapter 18 in Reference [3].

## 2.2 Electroweak Precision Tests of the SM

Deviations in measurements from the properties of elementary particles in the framework of a beyond-SM theory, can provide hints at new physics that could possibly exist at unexplored energy scales. These new particles can cause deviations either through their existence virtually in quantum loops or by contributions via new amplitudes through the exchange of such unknown heavy particles. It is to be noted that significant theoretical efforts over the years, to calculate the contributions of quantum loop effects of SM and Beyond Standard Model (BSM) particles at Next-to-Leading-Order (NLO) and Next-to-Next-to-Leading-Order (NNLO) has led to dramatic improvements in the predictions from field theories.

The importance of ElectroWeak Precision Tests (EWPT) has increased significantly in recent years, especially in the context of large amounts of data that is being collected at the Large Hadron Collider (LHC). The data collected at increasingly higher luminosities enables to measure SM processes at unprecedented accuracy, turning it into indirect probes of BSM physics. Apart from the Higgs boson, the lack of any new particles being discovered at the LHC is suggestive towards orienting our searches at higher energy scales than the EW scale. New physics effects can be represented through higher dimensional EFT operators. These higher-dimensional operators are sensitive to be probed both by low energy and by high energy measurements, with the two approaches being complementary and affecting each other.

The study of Electro-Weak Precision Observables, through extremely precise measurements of the interactions of EW gauge bosons is a robust and convenient tool to not only test the SM but also acts as an indirect gateway to presently unknown pastures of BSM physics. One of the most popular approaches to extend the SM is via Supersymmetry (SUSY), by extending its symmetry group. A detailed description regarding various benefits and drawbacks of SUSY is beyond the scope of this thesis and the review by Martin in Reference [18] can be referred to for further details. In this thesis, an alternative approach, based on EFT, is adopted to indirectly search for signals of BSM physics.

## 2.3 Effective Field Theory

The EFT approach relies on the fact that, for energy scale beyond that of current collider experiments, unknown degrees of freedom do not manifest directly as sharp resonances but as interactions with the already known particles. These new interactions are added to the Lagrangian in terms of higher-dimensional operators and suppressed by the new physics scale $\Lambda$ and are also invariant under the symmetries of the SM.

The Applequist-Carrazone theorem, in Reference [19] mandates (as a power expansion) that BSM theories reduce to the SM at low energies via decoupling of the heavy particles which have masses of order $\Lambda$. This implies that the Lagrangian of the effective theory $\mathcal{L}_{\text{EFT}}$ would have the $\mathcal{L}_{\text{SM}}$ and also the terms with higher dimensional operators, suppressed by power of $\Lambda$, in order to ensure renormalizability. Hence, the effective Lagrangian can be interpreted as a power series in $\Lambda$. Therefore, $\mathcal{L}_{\text{SM}}$ is the Leading Order (LO) term of the $\mathcal{L}_{\text{EFT}}$ expansion (refer to Reference [20] section 19.3 for a complete review):

$$\mathcal{L}_{\text{EFT}} = \mathcal{L}_{\text{SM}} + \sum_{i=WWW,W} \frac{c_i}{\Lambda^2} O_i + \sum_{j=0,1} \frac{f_{S,j}}{\Lambda^4} O_{S,j} + \sum_{j=0,\ldots,9} \frac{f_{T,j}}{\Lambda^4} O_{T,j} + \sum_{j=0,\ldots,7} \frac{f_{M,j}}{\Lambda^4} O_{M,j} \tag{2.32}$$

while $O_i$ are the six dimensional operators and $O_{S,j}$, $O_{T,j}$, $O_{M,j}$ are the eight dimensional operators in terms of $\Lambda$. The coefficients $c_i$ and $f_{i,j}$ are the respective dimensionless coupling constants (Wilsonian coefficients). In the limit of $\Lambda \to \infty$, the $\mathcal{L}_{\text{EFT}}$ reduces to $\mathcal{L}_{\text{SM}}$. Also, by imposing conservation of baryon and lepton numbers, only even dimensional operators are allowed in the effective Lagrangian $\mathcal{L}_{\text{EFT}}$. The coupling strengths are the free parameters in the effective theory, which can be utilized in further constraining the coefficients of these higher dimensional operators.

### 2.3.1 Quartic Gauge Coupling (QGC): Non-Standard EW Interactions

The $\mathcal{L}_{\text{SM}}$ itself contains both Triple Gauge Coupling (TGC) and Quartic Gauge Coupling (QGC). However, the largest contributions to new physics would be from six dimensional operators which could give rise to both TGC and QGC. The eight dimensional operators are the sub-leading contributors and QGC arises genuinely due to interactions between such eight dimensional operators.

The inclusion of eight dimensional operators, results in *anomalous* couplings in the quartic interactions of gauge bosons, and hence these operators are referred to as anomalous Quartic Gauge Coupling (aQGC) operators. The aQGC operators are defined with operator bases based on conventions in Reference [20].

The effective Lagrangians that conserve parity and leading to genuine quartic interactions between EW gauge bosons [21] are listed below. The Higgs boson $\Phi$ belongs to the $SU(2)_L$ doublet and denoting $U$ by an arbitrary $SU(2)_L$ transformation, the various components in the effective Lagrangian transform as :

- $\Phi$ transforming as $\Phi \to \Phi' = U\Phi$
- $D_\mu\Phi$ transforming as $D_\mu\Phi \to D'_\mu\Phi' = UD_\mu\Phi$
- $\hat{W_{\mu\nu}} \equiv \sum_j W^j_{\mu\nu}\frac{\sigma^j}{2}$ transforming as $\hat{W_{\mu\nu}}' \equiv U\hat{W_{\mu\nu}}U^\dagger$
- $B_{\mu\nu}$ transforming as $B'_{\mu\nu} = B_{\mu\nu}$

There are three classes of such operators – Scalar, Tensor and Mixed operators based on the combination of various tensors in tables 2.1, 2.2, 2.3. The coupling constants have units of $\text{GeV}^{-4}$.

| Label | Scalar Operators |
|---|---|
| S0 | $\mathcal{O}_{S,0} = [(D_\mu\phi)^\dagger D_\nu\phi] \times [(D^\mu\phi)^\dagger D^\nu\phi]$ |
| S1 | $\mathcal{O}_{S,1} = [(D_\mu\phi)^\dagger D^\mu\phi] \times [(D_\nu\phi)^\dagger D^\nu\phi]$ |

Table 2.1: Eight dimensional scalar operators [20].

| Label | Tensor Operators |
|---|---|
| T0 | $\mathcal{O}_{T,0} = \mathrm{Tr}[W_{\mu\nu}W^{\mu\nu}] \times \mathrm{Tr}[W_{\alpha\beta}W^{\alpha\beta}]$ |
| T1 | $\mathcal{O}_{T,1} = \mathrm{Tr}[W_{\alpha\nu}W^{\mu\beta}] \times \mathrm{Tr}[W_{\mu\beta}W^{\alpha\nu}]$ |
| T2 | $\mathcal{O}_{T,2} = \mathrm{Tr}[W_{\alpha\mu}W^{\mu\beta}] \times \mathrm{Tr}[W_{\beta\nu}W^{\nu\alpha}]$ |
| T5 | $\mathcal{O}_{T,5} = \mathrm{Tr}[W_{\mu\nu}W^{\mu\nu}] \times [B_{\alpha\beta}B^{\alpha\beta}]$ |
| T6 | $\mathcal{O}_{T,6} = \mathrm{Tr}[W_{\alpha\nu}W^{\mu\beta}] \times [B_{\mu\beta}B^{\alpha\nu}]$ |
| T7 | $\mathcal{O}_{T,7} = \mathrm{Tr}[W_{\alpha\mu}W^{\mu\beta}] \times [B_{\beta\nu}B^{\nu\alpha}]$ |
| T8 | $\mathcal{O}_{T,8} = B_{\mu\nu}B^{\mu\nu}B_{\alpha\beta}B^{\alpha\beta}$ |
| T9 | $\mathcal{O}_{T,9} = B_{\alpha\mu}B^{\mu\beta}B_{\beta\nu}B^{\nu\alpha}$ |

Table 2.2: Eight dimensional tensor operators [20].

| Label | Mixed Operators |
|---|---|
| M0 | $\mathcal{O}_{M,0} = \mathrm{Tr}[W_{\mu\nu}W^{\mu\nu}] \times [(D_\beta\phi)^\dagger D^\beta\phi]$ |
| M1 | $\mathcal{O}_{M,1} = \mathrm{Tr}[W_{\nu\beta}W^{\mu\nu}] \times [(D_\beta\phi)^\dagger D^\mu\phi]$ |
| M2 | $\mathcal{O}_{M,2} = [B_{\mu\nu}B^{\mu\nu}] \times [(D_\beta\phi)^\dagger D^\beta\phi]$ |
| M3 | $\mathcal{O}_{M,3} = [B_{\mu\nu}B^{\nu\beta}] \times [(D_\beta\phi)^\dagger D^\mu\phi]$ |
| M4 | $\mathcal{O}_{M,4} = [(D_\mu\phi)^\dagger W_{\beta\nu}D^\mu\phi] \times B^{\beta\nu}$ |
| M5 | $\mathcal{O}_{M,5} = [(D_\mu\phi)^\dagger W_{\beta\nu}D^\nu\phi] \times B^{\beta\mu}$ |
| M6 | $\mathcal{O}_{M,6} = [(D_\mu\phi)^\dagger W_{\beta\nu}W^{\beta\nu}D^\mu\phi]$ |
| M7 | $\mathcal{O}_{M,7} = [(D_\mu\phi)^\dagger W_{\beta\nu}W^{\beta\mu}D^\nu\phi]$ |

Table 2.3: Eight dimensional mixed operators [20].

## 2.4 Validity of the EFT Model

One of the important consequences of the inclusion of EFT operators is that the cross-section $\sigma(E)$ grows proportionally with energy $E$ [22]. This can be explained by the fact that in Minkowski space (four space-time dimensions), field theories with higher dimensional operators (with mass dimensions d > 4 ) are sensitive to the UV cut-off of the theory $\Lambda$.

It is extremely important to ensure that the EFT remains in the region $E < \Lambda$ , in order to ensure the validity of power expansion of the effective Lagrangian. If the EFT power expansion would itself be invalid or unreliable, it would be an arduous task to interpret the constraints in any explicit BSM model.

To ensure that EFT analyses remain in their validity region, a kinematic cut ($E_{Cut}$) is proposed, for the events being analyzed, so that the condition $E < E_{Cut} < \Lambda$ is always guaranteed. The application of a kinematic cut has been proposed in References [22], [23] and also recommended by the Top LHC WG group in Reference [24]. Though a cut is advocated to be imposed on the events, no specific value of $E_{Cut}$ has been specified. Therefore, the cut is model dependent and is driven by phenomenological considerations and would probe the validity of the given EFT at $\Lambda = E_{Cut}$.

CHAPTER **3**

# Simulation Setup

This chapter provides an overview of the tools employed for undertaking the simulation study in this thesis. The array of software tools utilized is described in Section 3.1 with a brief overview of FeynRules, UFO models and Rivet. The event generator called MadGraph5 is detailed in Section 3.2. Lastly, the sensitivity study carried out on various aQGC operators is described in Section 3.3.

## 3.1 Software Tools

### 3.1.1 FeynRules

The FeynRules package [25] based on Mathematica [26], is the first step in transforming a given physics theory/model into a format that is comprehensible for computers. These models, can be utilized for developing simulations and analyzing the data acquired for a given model for phenomenological studies and experimental analyses.

All particle physics theories are Quantum Field Theories (briefly described in Section 2.1.2), which are expressed in Lagrangian formalism. These Lagrangians are composed of fields (scalar/fermion/boson) and derivatives of fields, vertices, couplings and parameters along with respective Feynman rules regarding the particular process of interest. Every process involves possibly multiple Feynman diagrams and consequently Feynman amplitudes. The book by Thomson [3] can be referred to for an explanation and procedure to arrive at the respective amplitudes. The landscape of Beyond Standard Model (BSM) physics, involves a multitude of theoretical models and their implementation into MC event generators remains a demanding and time-consuming affair.

The FeynRules package is a tool in this regard, which helps in converting particle theories into the Universal FeynRules Output (`UFO`) format output. This package enables to obtain Feynman rules in momentum space associated with the Lagrangian for any QFT physics models. The implementation of a general model that is input by the user, requires the model to respect the properties of Lorentz invariance, gauge invariance and locality. The utility and flexibility of FeynRules has dramatically increased from the time of its introduction, with many additional features being incorporated recently that includes: addition of two-component fermions, spin-$\frac{3}{2}$ and spin-2 fields, inclusion of superspace notation, SUSY calculations and also a new interface for `UFO` formats.

Upon implementation of these models by the FeynRules package, the output obtained from it in terms of `UFO` format is fed as input to MC event generators like `MadGraph5` [27], `Sherpa` [28] and

Whizard [29] among the many event generators available for the High Energy Physics community today. Therefore, the FeynRules package is an important cog in the wheel of moving from theoretical models to developing simulations and finally validation of experimental data with increasingly high levels of precision.

### 3.1.2 UFO Models

The Universal FeynRules Output [30] is the output obtained in a general purpose format after implementing a given physics model thr ough theFeynRules package, as explained above. A major advantage in utilizing this format is that it does not make any *apriori* assumptions nor restricts the different structures that could be included in a given model. Therefore, this flexible format enables to encode all relevant information about the model in an abstract form and can be easily accessed by other tools.

A set of objects in the Python [31] programming language, stores the information regarding particles, parameters and the respective vertices of the given model. The properties of above listed physics structures are associated with a list of attributes. The representation of the model information in this manner has significant benefits over other conventional text table-based format. This can be illustrated from the fact that a new representation enables the user to include any additional information directly as a new attribute in the respective object.

Currently, the UFO format is being used by MadGraph5 [27] and Herwig++ [32]. The UFO model, for the current study of aQGC operators (with particle containers that include all five flavours of quarks except the top quark), is obtained as an open source resource from Reference [21].

### 3.1.3 Rivet

The Robust Independent Validation of Experiment and Theory or Rivet is a platform [33, 34], to validate the output from various Monte Carlo event generators. The advantage of Rivet is best expressed through the quote from Reference [34]: “Rivet is a C++ class library, which provides the infrastructure and calculational tools for particle-level analyses for high energy collider experiments, enabling physicists to validate event generator models and tunings with minimal effort and maximum portability”. The feature of Rivet being “generator-agnostic” [35] makes it an attractive tool for theorists, phenomenologists and experimentalists for building their analysis with Rivet. Its widespread usage can also be attributed to the fact that Rivet preserves the analysis code for various collider experiments across the world.

Depending on requirements of the analysis tasks, a script (defined as Rivet routine henceforth) for analyzing the events is developed by utilizing the numerous classes, particle-containers and other computational infrastructure provided by Rivet. The events (generated as output from event generators) is input into Rivet routine, for undertaking the analysis of events. The Rivet routine includes various stages of analyzing events like object definition, event selection, reconstruction of objects from decayed final states and also producing histograms of all relevant observables.

In this study, the events for analysis were generated through MadGraph5 generator (described in the following section) and the Rivet routine that was developed for analyzing these events is provided in Appendix B. The procedure involved in the development of the Rivet routine and the details regarding the analysis of events will be described in greater detail in Chapter 4.

## 3.2 MadGraph

The objective behind collider-based experiments, like the Tevatron [3] or Large Hadron Collider [3], is to gain a deeper understanding of the fundamental building blocks of matter and their interactions. These experiments are built to verify the claims and predictions of SM and also to probe the existence of phenomena beyond SM physics. The probe for new physics in these experiments and the interpretation of their results, rely extensively on our capabilities to perform simulations for both the signals and their backgrounds to increasingly higher orders of precision. The simulation of physics processes is carried out by generating "events" through event generators like MadGraph5. These events encapsulate all relevant physical phenomena related to the given process of interest. A set of events are referred to as "event-samples/samples".

MadGraph5 [27] is the upgraded avatar from its earlier version of the MadGraph generator [36] and has been built using the Python programming language. A step-by-step tutorial explaining the simulation of events is available from the twiki in Reference [37]. The script for simulating events for this study is available in Appendix B.

A number of attractive features to enhance the capabilities of MadGraph has been incorporated recently. These include a novel and efficient algorithm for improved performance and a new user-friendly interface for the user. It also provides the option of obtaining output in several formats along with full compatibility with FeynRules. This feature of MadGraph5 potentially ensures the implementation of the entire landscape of physics models, as long as the model is written in the form of a Lagrangian.

The input parameters for generating events for a given process is included through inbuilt tools of MadGraph called run_card and parameter_card. All model independent parameters are included in the run_card. These include the different parameters of the incoming beam like energy, particle type, pdf, polarization and also includes the cuts to be imposed at the parton level itself. The external parameters of the model are included in the parameter_card.

## 3.3 Sensitivity Study of aQGC

The triple gauge couplings as predicted by the SM were described in Section 2.1.4. First evidence for the production of three massive vector bosons from a single $pp$ collision was observed with a significance of 4.0 standard deviations [14, 15]. Triboson production studies provide a handle to probe the non-Abelian gauge structure of the SM.

The possible deviations in comparison with the SM predictions would provide hints of new physics at higher energy scales. In certain models with higher dimensional EFT operators (like eight dimensional aQGC operators in the current study), these couplings can be modified, leading for instance to a significant enhancement of the *WWZ* production cross section. These modified couplings are referred to as "anomalous couplings". The evidence for the production of three massive vector bosons is the motivation behind undertaking a sensitivity study on aQGC operators. The sensitivity study involves compiling the most constrained limits from various analyses for all aQGC operators that contribute to *WWZ* production. These operators are then probed for deviations in cross-sections with respect to the SM cross section ($\sigma_{\mathrm{SM}}$).

### 3.3.1 Generation of events

The JobOption (JO) for the generation of events, along with the respective `run_card` and `parameter_card` for a given EFT operator is provided as an example in Reference [38]. It is also ensured in the JO to obtain the output as a root file. 10000 events per sample are generated on the grid. An example of the respective JO employed for generation of event samples is given in Reference [38].

The generation of event samples for respective operators is simulated at Leading Order with `MadGraph5` v2.6.2 and involves the following steps:

1. Importing the `UFO` Model: The `UFO` model (updated to the five flavour scheme) contains the SM Lagrangian along with the Lagrangian for respective aQGC operators (enlisted in tables 2.1, 2.2, 2.3) is obtained from Reference [21]. This can be input into our JO via the `import` command. Also, the particle container is defined by including three flavors of leptons and five flavors of quarks (the sixth flavor of quark is not kinematically accessible).

2. Process Generation: The relevant process to be generated ($pp > W^-W^+Z$) is specified along with the highest order of the couplings. The Quantum Electrodynamics (QED) coupling is a combination of both QED and Electro-Weak (EW) couplings while first order coupling for New Physics (NP) is included.

3. Decay via `MadSpin`: The `MadSpin` [39] program is called for decaying the vector bosons providing spin correlations. The $W^-$ and $W^+$ bosons are allowed to decay into all possible combinations of final states, while the Z boson is forced to decay into leptons with opposite charge. The leptons referred to at the generation stage include all the three flavors of leptons.

4. Showering: The `Pythia v8.2.10` [40] package is utilized for showering, underlying event simulation and hadronization and the `NNPDF30_lo_as_0118` set (obtained from References [41, 42]) has been utilized for the provision of Parton Distribution Functions [43].

5. Coupling strength: Then the events are generated by including the appropriate `run_card` and also by providing the values of the coupling strengths in the `parameter_card` for the respective operator in the JO.

6. Filters: Three-lepton filters are included in order to obtain events which have exactly three charged leptons and other events are rejected. The filter efficiency was found to be 44.71% for the total number of events. It is the value obtained via : 2 * BF ($W \rightarrow \ell\nu$) * BF($W \rightarrow q\bar{q}$).

Hereafter, the following nomenclature will be used:

- Leptonic $Z$ Boson: $Z \rightarrow \ell^+\ell^-$
- Leptonic (*W_Lep*) $W$ Boson: $W \rightarrow \ell\nu$
- Hadronic (*W_Had*) Boson: $W \rightarrow q\bar{q}$

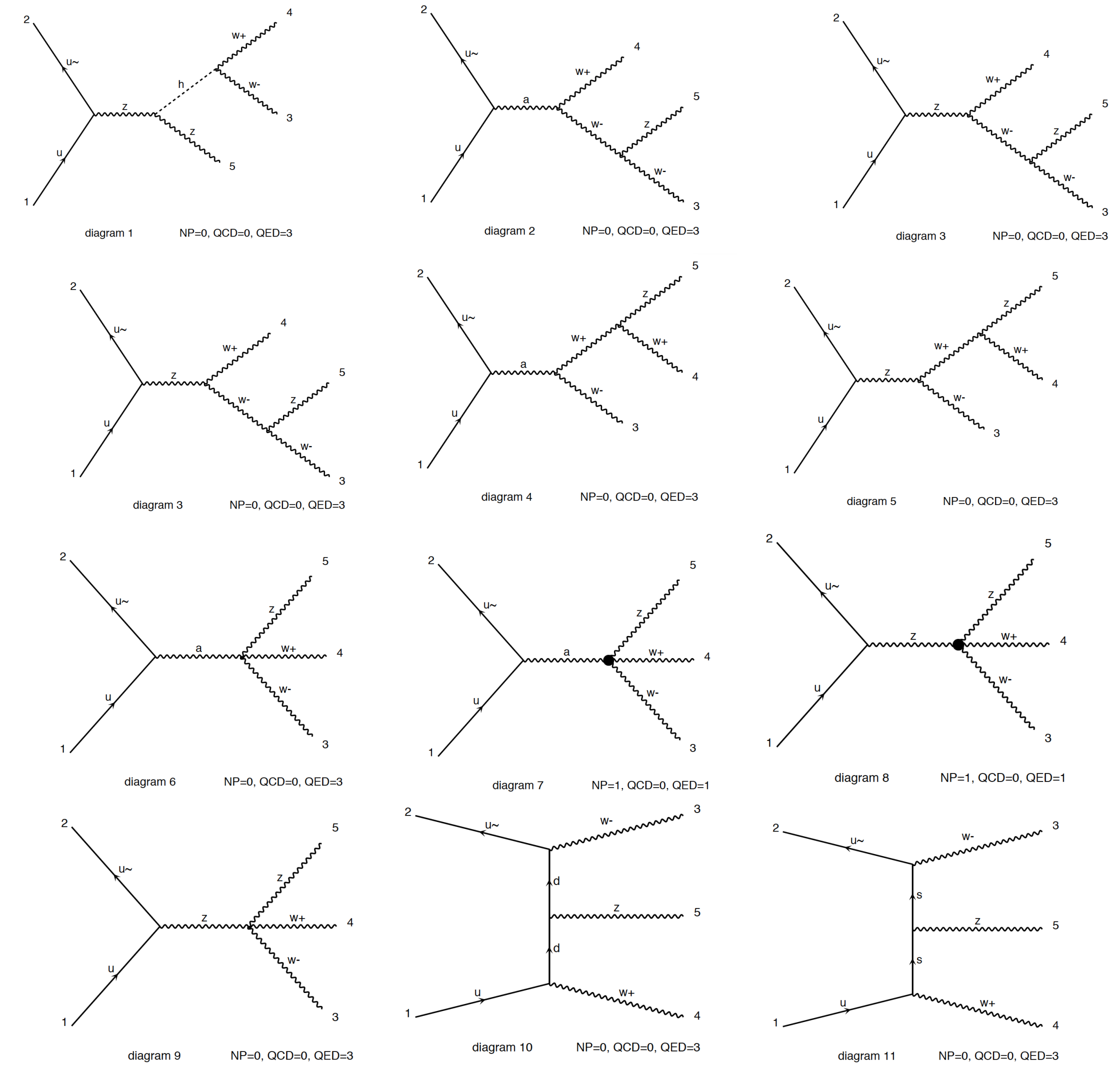


Figure 3.1: Feynman diagrams for production of *WWZ* after inclusion of aQGC operators as produced by `MadGraph5`

.

### 3.3.2 Feynman Diagrams

The Feynman diagrams produced by the `MadGraph5` generator for the production of *WWZ* are displayed in Figure 3.1. It can be confirmed through the coupling of NP being equal to one (production of *WWZ* at leading order), that the diagrams with a highlighted vertex are indicative of the additional diagrams produced due to the inclusion of aQGC operators.

### 3.3.3 Deviations from the SM

The operators that contribute to the production of *WWZ* are enlisted and defined in Section 2.3.1. The coupling strength of the operators, when set to zero, would result in the effective Lagrangian reduce

| Operator | Limits ( $\mathrm{TeV}^{-4}$) | $\sigma_{\mathrm{aQGC}}$(fb) | Deviation= ($\Delta\sigma/\sigma_{\mathrm{SM}}$)*100 (% ) |
|---|---|---|---|
| T0 | [-0.46 - 0.44] | 90.39 | 1.56 |
| T1 | [-0.61 - 0.61] | 90.16 | 1.3 |
| T2 | [-1.2 - 1.2] | 90.5 | 1.66 |
| T5 | [-3.8 - 3.8] | 96.31 | 8.21 |
| T6 | [-2.8 - 3.0] | 89.58 | 0.65 |
| T7 | [-7.3 - 7.7] | 89.58 | 0.65 |

Table 3.1: The best limits for tensor operators as obtained from Reference [45].

| Operator | Limits ($\mathrm{TeV}^{-4}$) | $\sigma_{aQGC}$(fb) | Deviation= ($\Delta\sigma/\sigma_{\mathrm{SM}}$)*100 (%) |
|---|---|---|---|
| M0 | [-4.2 - 4.2] | 91.3 | 2.58 |
| M1 | [-16 - 16] | 99.02 | 11.25 |
| M2 | [-26 - 26] | 135.8 | 52.58 |
| M3 | [-43 - 44] | 131.5 | 47.5 |
| M4 | [-40 - 40] | 180.31 | 100.2 |
| M5 | [-65 - 65] | 189.4 | 112.8 |
| M7 | [-13 - 13] | 91.94 | 3.3 |

Table 3.2: The best limits for Mixed operators as obtained from [46, 47, 48, 49].

| Operator | Limits ($\mathrm{TeV}^{-4}$) | $\sigma_{\mathrm{aQGC}}$(fb) | Deviation= ($\Delta\sigma/\sigma_{\mathrm{SM}}$)*100 (%) |
|---|---|---|---|
| S0 | [-118.75 - 150] | 89.85 | 0.95 |
| S1 | [-181.75 - 231.25] | 91.69 | 3.02 |

Table 3.3: The best limits for Scalar operators was obtained from [50].

to the SM Lagrangian and thereby would provide the value of $\sigma_{\mathrm{SM}}$ at tree level which was found to be 89 fb. The $\sigma_{\mathrm{SM}}$ refers to production of $WWZ$ process at tree level $\sigma(pp \rightarrow WWZ)$.

The best constrained limits for various TGC and QGC couplings from both ATLAS and CMS searches are available in Reference [44] and quoted in Tables 3.1, 3.2 and 3.3. The negative values of the limit, when provided as input in the `parameter_card`, will not affect the cross section, since the matrix element is squared in expression for differential cross sections ($\frac{d\sigma}{d\Omega}$) for a given process.

For the cross sections enlisted above, the coupling strength is obtained by calculating the average from absolute values of best limits in the Tables 3.1, 3.2 and 3.3 and then included in the `parameter_card`. After generating the respective aQGC sample, the value of $\sigma_{\mathrm{aQGC}}$ is tabulated. The variation in cross section in comparison to SM is obtained as $\Delta\sigma$ by taking the difference between $\sigma_{\mathrm{aQGC}}$ and $\sigma_{\mathrm{SM}}$. The relative deviation is then calculated as the ratio $\Delta\sigma/\sigma_{\mathrm{SM}}$.

From the values of the best limits, the tensor and scalar operators are better constrained than the mixed operators. However, from the deviations in cross-sections that were observed after the generation of events, it can be seen that the mixed operators have the highest deviations while the tensor and scalar operators do not deviate from $\sigma_{\mathrm{SM}}$ significantly. Therefore, samples of mixed operators are chosen for performing the analysis through the custom-built `Rivet` routine which will be described in the next chapter.

CHAPTER **4**

# Sensitivity to aQGC in *WWZ* Production

The simulation and generation of events was carried out and described in the previous chapter. This chapter details the phenomenological study and the figures obtained for respective aQGC operators. Section 4.1 describes the physics objects involved and the event selection of three charged leptons (oppositely charged leptons $\ell^+\ell^-$) from a $Z$ boson and (other lepton and neutrino $\nu$) from a $W$ boson and two jets ($q\overline{q}$) in the final state. The reconstruction of candidates for three bosons from the selected events is outlined in Section 4.2. The imposition of kinematic cuts on important observables and its impact is discussed in Sections 4.3 and 4.4. Section 4.5 displays figures for a set of discriminating variables. Also, a statistical test is performed to quantify the discriminating power of these variables.

The EFT Lagrangian for aQGC operators, for a given energy scale $\Lambda$, includes terms from both SM and higher dimensional operators to the triple gauge coupling of the SM Lagrangian. Tri-boson production is a rare process as predicted by the Standard Model. It involves self-interaction among the weak bosons through triple and quartic gauge boson couplings (as specified in Section 2.1.4), which are sensitive to contributions from unknown particles and/or interactions. The objective of this study is to understand how the *WWZ* production is affected by the inclusion of aQGC operators and to identify discriminating variables that can be useful for future analyses.

In this study, the samples generated without aQGC operators are referred to as SM samples while those that are generated including them are referred to by the name of the respective operators. Hence, the aQGC samples include both SM and higher-dimensional operator components.

The values of deviations in cross-section for these higher-dimensional EFT operators provided in Section 3.3.3, indicate that the limits on scalar and tensor operators are tightly constrained, while there is further scope for constraining the mixed operators. The M5 operator is chosen for undertaking this study, since its inclusion results in the largest deviations of cross-sections as shown in Table 3.2.

In the case of other operators, their structure (as defined in Section 2.3.1) and the deviations impacts the nature of distributions for various observables. Therefore, the same analysis is performed on other operators (apart from M5) with significant effects in the total cross section and their behavior can be seen in Appendix A for the M2 and T5 operators (without descriptions).

## 4.1 Event Selection

`Rivet` (introduced in Section 3.1.3) is a tool to define physics objects like jets, leptons, neutrinos and photons, isolate them based on analysis strategy and to produce histograms for these observables. It is also possible to define cuts to make the objects suitable for our analysis.

The steps involved in the analysis are described below. Also, there are a number of `Rivet` classes that are inherited from the `Rivet` name-space thereby enabling increased functionality and flexibility in developing an analysis through the `Rivet` routines. The script for the `Rivet` routine and the list of Rivet classes inherited is referred in Appendix B.

### 4.1.1 Object Definition

A "cut" is a requirement on kinematic variables that needs to be fulfilled for the event to be accepted. Else the event is rejected (vetoed). These cuts are useful to obtain events with the exact final states relevant for this study. "Baseline-cuts" are cuts placed on generic entities (like jets, leptons, neutrinos) to be well-defined physics objects. These entities are the building blocks for obtaining the reconstructed boson candidates. It enables in reducing the number of fakes with the help of these cuts.

For leptons, a $p_{\mathrm{T}} > 10$GeV and $|\eta| < 2.5$ are required, while for jets the corresponding cuts are $p_{\mathrm{T}} > 25$GeV and $|\eta| < 5.0$. The leptonic tau decay is allowed and "leptons" are referred to as `electrons` and `muons` only, for the purposes of this analysis. Jets are reconstructed from the $anti - k_T$ jet clustering algorithm [51] as per its implementation using FastJet [52] with a distance parameter of $R = 0.4$. There are no constraints placed on neutrinos.

The values of these baseline cuts is that they follow standard ATLAS selections and is dictated by acceptance, reconstruction, fake rejection etc. Furthermore, imposing baseline-cuts reduces smearing of the peaks of invariant masses and ensures good quality candidates for the reconstruction of bosons.

### 4.1.2 Jet and Lepton Selections

Every event is required to have at least one jet, else the event is vetoed. The number of jets in each event is displayed in Figure 4.1 for both the M5 and SM samples. It is to be noted that this figure is filled for events with all jets.

The former has a large number of events with a single jet while the latter has two or more jets in the majority of events. In certain cases, its possible that due to its boosted nature of the $W$ boson, decays into a pair of collimated jets with a small opening angle between them. This pair of jets, being very close in the jet cone, is reconstructed as "merged-jet" or a single-jet by the $anti - k_T$ algorithm for the M5 sample. The invariant mass for events with exactly one jet (which could be a merged jet) is shown in Figure 4.2.

The SM sample has many single jets in the low mass region, while the peak at $M_W = 80$ GeVconfirms that the M5 sample contains $W$ bosons reconstructed as single-jets by the $anti - k_T$ algorithm. Hence, those events with single jets which are close to $M_W$ are retained, for events with a single jet with an invariant mass in range of 50–110 GeV. This jet is chosen as the candidate for the $W$ boson that decays hadronically.

#### Lepton Selection

At least three charged leptons in the final state are required in every event. These leptons are obtained after applying the baseline cuts for all entities from the `dressedleptons` container that is provided by Rivet. The `dressedleptons` are bare leptons that are clustered together with photons [53].

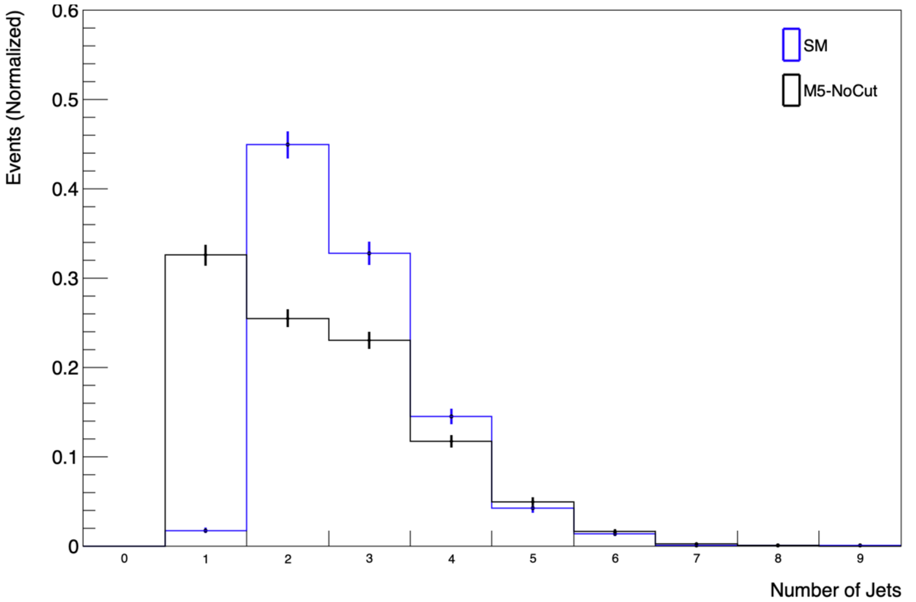


Figure 4.1: The number of jets after requiring at least one jet with $p_{\mathrm{T,Jet}} > 25\mathrm{GeV}$ for the SM and M5 samples before imposing jet selections, with only the statistical uncertainties being displayed. The events are normalized to one.

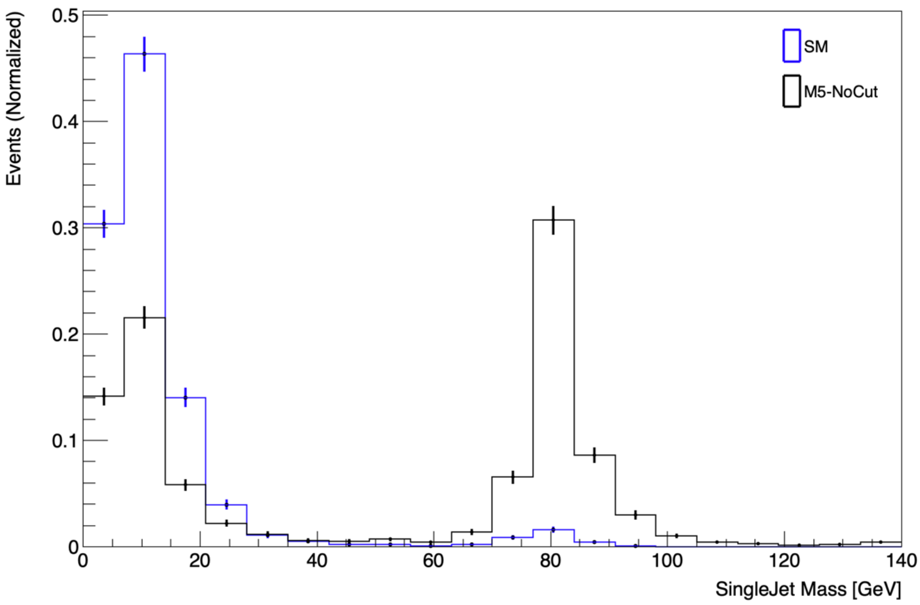


Figure 4.2: Single jet requiring $p_{\mathrm{T,Jet}} > 25$ GeVfor the SM and M5 samples, with only the statistical uncertainties being displayed. The last bin contains overflow. The events are normalized to one.

Neutrinos could originate from either a $W$ boson decay or from tau decays. They are obtained from the `neutrinos` container provided by `Rivet`. Only one neutrino is present in the majority of events and the neutrino with highest transverse momenta is utilized for reconstruction purposes in our analysis.

Exactly three leptons are present in the majority of events. However, additional leptons are observed in few instances (four or five leptons in certain events). This is due to the presence of virtual photons in the initial state radiation, decaying into leptons and thereby leading to additional leptons in the final state. Also, jets can be mis-reconstructed as leptons in few instances.

In conclusion, only the objects that have passed the baseline-cuts are eligible to be defined as jets, leptons or neutrinos. Each event must contain at least one jet, a minimum of three charged leptons and at least one neutrino associated with it.

### 4.1.3 Event Selection Summary

Figure 4.3 shows the cut flow , i.e, the number of events that remain after passing subsequent conditions, imposed during the event selection. The number of events remaining after each requirement is displayed in the three bins of the histogram. The first bin contains the total number of events without applying any conditions, the second bin contains the number of events after the jet selection (at least one jet and $p_{\mathrm{T}} > 25\mathrm{GeV}$) and the last bin contains events that have passed the lepton selection (minimum of three leptons in every event) along with choosing the neutrino with highest transverse momenta.

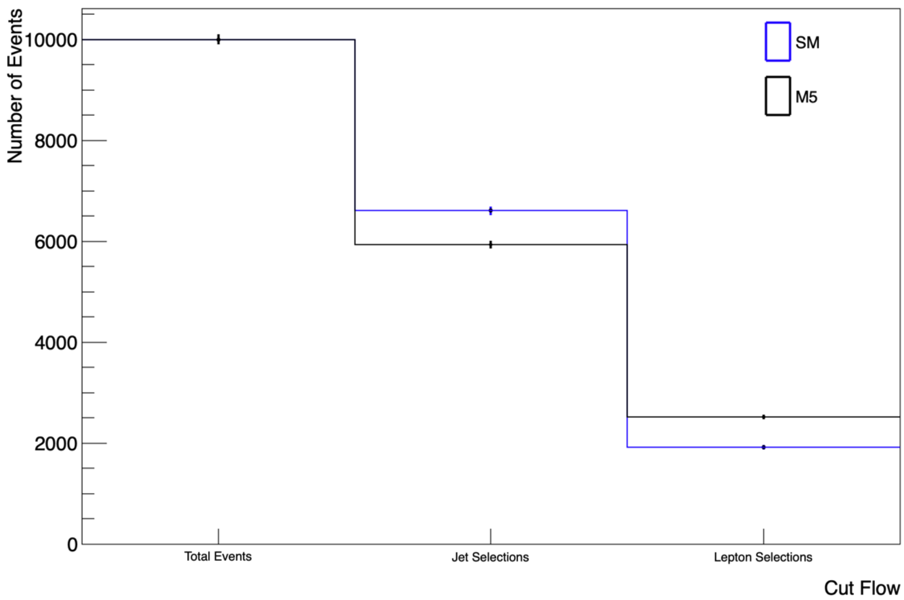


Figure 4.3: Total number of events, events passing jet constraints and passing lepton requirements for the SM and M5 samples, with the statistical uncertainties being displayed.

There are more SM events passing the jet selection criteria than the M5 events while the opposite is true after the lepton selection. In the M5 sample, bosons are boosted and thereby also the leptons from tau decays are boosted, which would easily satisfy the baseline cuts for jets. Hence, more leptons are found for the M5 sample than in the case of SM. In the case of jets, the baseline cuts were more stringent than leptons resulting in many jets that are low in transverse momentum being rejected. It results in fewer selected jets for the M5 sample than for the SM sample.

## 4.2 Event Reconstruction

The procedure for reconstruction of the bosons from their decay products is outlined below. The figures for the reconstructed candidates do not reveal any differences between the SM and aQGC samples. Hence, these figures are useful to verify that ancestors of decayed final state particles are indeed $W^- W^+ Z$ bosons and also serves to prove the efficacy in the reconstruction mechanism.

### 4.2.1 Hadronic *W* Boson Candidate

There are a number of events with two or more jets as seen in Figure 4.1. The invariant mass for each jet pair is calculated and the invariant mass of jet pair being closest to $M_W$ is chosen as the hadronically decaying $W$ boson candidate. The figure displaying all possible invariant masses of dijets, is shown in Figure 4.4.

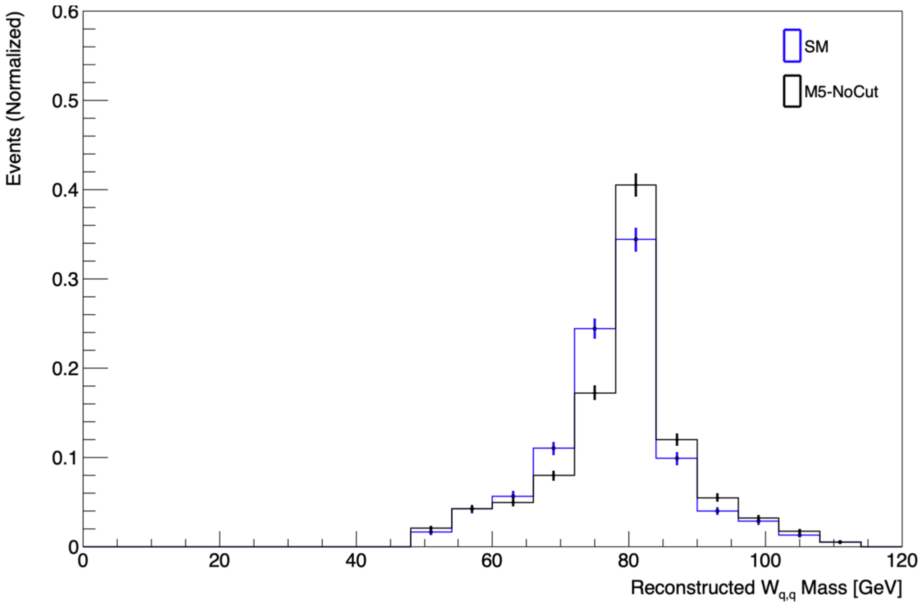


Figure 4.4: The reconstructed invariant mass of all possible candidates from pairs of jets, for SM and M5 samples with only the statistical uncertainties being displayed. The events are normalized to one.

### 4.2.2 Leptonic *Z* Boson Candidate

The leptons, which reconstruct the $Z$ boson, must qualify a precondition that they be of same flavor and opposite charge. The reconstruction is performed by summing over the four momenta of lepton pairs. The $Z$ boson candidate is selected based on an invariant mass criterion, such that the candidate's mass is closest to mass of $Z$ boson (abbreviated as $M_Z$ with $M_Z = 91.2$ GeV[5]). This is similar to the case of reconstructed $W$ boson candidates using pairs of jets. The figure displaying the reconstruction of all possible $Z$ boson candidates is provided in Figure 4.5.

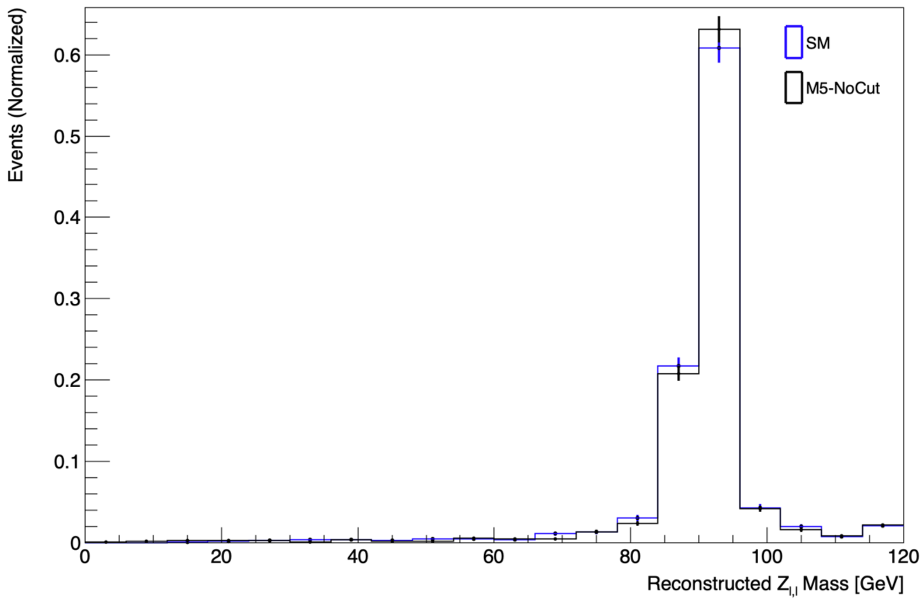


Figure 4.5: The reconstructed invariant mass of all possible pairs of opposite-sign-same-flavored leptons closest to mass of $Z$ boson, for SM and M5 samples with the statistical uncertainties being displayed. The last bin contains overflow. The events are normalized to one.

### 4.2.3 Leptonic *W* Boson Candidate

Based on the event selection specified earlier, after obtaining candidates for $W$ and $Z$ bosons (that decays hadronically and leptonically respectively), the neutrino and a lone lepton remain unused so far for reconstruction. The $W$ boson candidate that decays leptonically is reconstructed by choosing the remaining lepton along with the neutrino with the hardest-$p_{\mathrm{T}}$. The invariant mass for the candidate is checked to be closest to that of $M_{\mathrm{T}}^{W}$. In certain instances when there are more than one remaining-leptons available, the lepton with hardest $p_{\mathrm{T}}$ is selected to perform the reconstruction of the candidate as displayed in Figure 4.6.

## 4.3 Key Observables and Implementation of Kinematic Cuts

Two key observables, $H_{\mathrm{T}}$ and the invariant mass of the entire system, abbreviated henceforth as `InvMass_WWZ` are defined below. Their importance is due to the fact that these observables are defined by including all the constituents of the system. This makes them suitable candidates for placing requirements and they are advantageous in the context of this study, since they allow to impose a kinematic requirement on a minimal number of observables while being a measure of all the constituents of the system. The procedure for generating different samples after placing cuts is outlined in the following section. Furthermore, various kinematic observables as a function of cuts on the two key observables are shown.

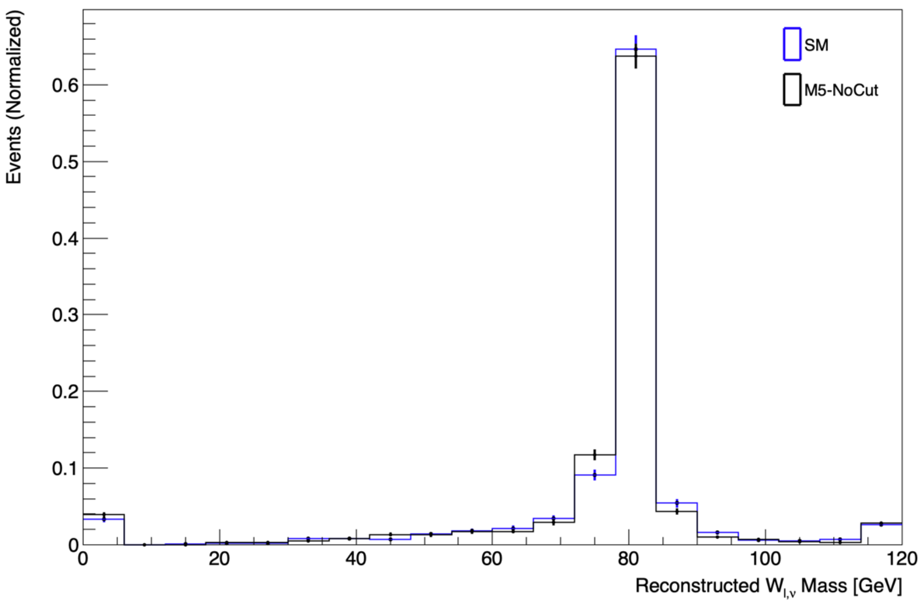


Figure 4.6: The reconstructed invariant mass from the remaining lepton with the highest transverse momentum and the hardest neutrino, for the SM and M5 samples with only the statistical uncertainties being displayed. The last bin contains overflow. The events are normalized to one.

### 4.3.1 Key Observables

The variable $H_T$ is defined as:

$$H_{\mathrm{T}} = \sum_{\text{visible particles}} p_{\mathrm{T}} \tag{4.1}$$

where the visible particles includes all jets and leptons. It is to be noted that the contributions of neutrinos are not included. The distribution for $H_{\mathrm{T}}$ is displayed in Figure 4.7.

The invariant mass of the entire system is shown in Figure 4.8. Since the $W$ boson candidate is reconstructed through contribution from neutrino with hardest-$p_{\mathrm{T}}$, consequently the `InvMass_WWZ` includes contributions from the neutrinos as well and is therefore the key difference between the above mentioned observables. The inclusion of contributions from neutrinos results in a large amount of overflow for the invariant mass of the system.

### 4.3.2 Implementing Kinematic Cuts

As mentioned earlier, the EFT Lagrangian includes both, SM and aQGC terms (the M5 operator is defined in Table 2.3) for the triple gauge coupling of the SM Lagrangian. In the M5 sample, the inclusion of such EFT operators is the cause for the leptonic $W$, leptonic $Z$ and hardonic $W$ bosons and its respective decay products to be boosted in their final states. This can be inferred from the high-$p_{\mathrm{T}}$ tail of the M5 sample, which is shown up to 5000 GeVin Figure 4.7. In the case of the SM sample, the decay products are not since they lack EFT operators and therefore $H_{\mathrm{T}}$ and `InvMass_WWZ` are limited to values below 2500 GeV.

$H_{\mathrm{T}}$ is an important observable for this analysis and different cuts are imposed on it in order to

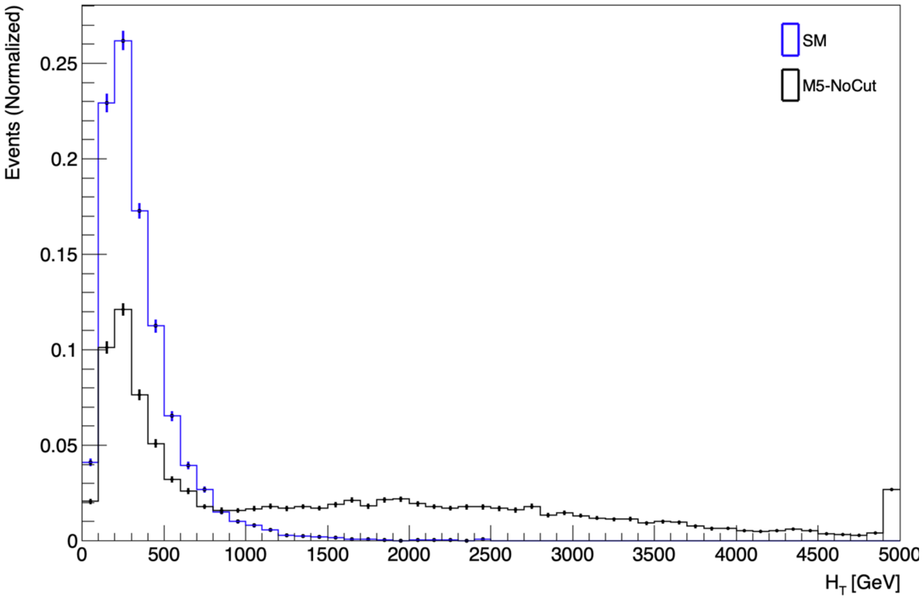


Figure 4.7: $H_{\mathrm{T}}$ for SM and M5 samples, with the statistical uncertainties being displayed. The last bin contains the overflow. The events are normalized to one.

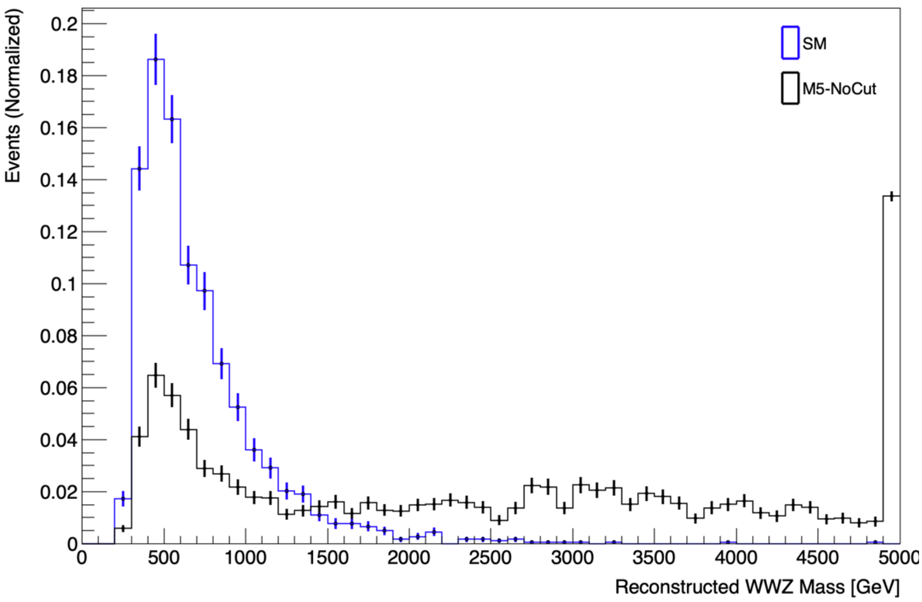


Figure 4.8: The invariant mass of the *WWZ* system for SM and M5 samples, with the statistical uncertainties being displayed. The last bin contains overflow. The events are normalized to one.

probe the validity of the effective theory (as described in section 2.4). The imposition of cuts also has a bearing on kinematics of other observables. The impact of cuts enables us to understand the energy scales at which these higher dimensional operators become relevant and facilitates in constraining the limits of these operators to high levels of precision. The cuts on $H_{\mathrm{T}}$ also help in

| Sample | Kinematic Cut | Color (In Figures) | Definition (in text) |
|---|---|---|---|
| SM | No Cut | Blue | `SM` |
| M5 | No Cut | Black | `M5-NoCut` |
| M5 | 3 TeV | Red | `M5-3TeVCut` |
| M5 | 1 TeV | Orange | `M5-1TeVCut` |

Table 4.1: Sample definitions and kinematic cuts.

identifying discriminating variables that could be exploited during experimental analysis to (dis)prove the existence of said process in an EFT framework.

After placing the cuts on $H_{\mathrm{T}}$, the `Rivet` routine is run on the generated event samples (as described in 3.3.1 ). The distributions for each observable, with different cuts, is displayed in the same histogram for comparison with the sample from SM in Figure 4.10. These `Rivet` analyzed samples are defined on the basis of cut values shown in the Table 4.1. Although similar cuts were placed on the `SM` sample too, these samples are not included in the figures since they do not display a marked difference in its distributions with or without the cuts.

It could be argued that, since both, $H_{\mathrm{T}}$ and `InvMass_WWZ` contain boosted final state entities, they are both well suited for placing kinematic cuts in order to check the validity of EFT. A two dimensional figure for `InvMass_WWZ` against $H_{\mathrm{T}}$ in Figure 4.9 reveals a (nearly) linear correlation between the two variables. This implies that the cuts would be equally valid for either of these observables. However, the key difference between these two variables is that $H_{\mathrm{T}}$ does not include contribution from neutrinos. This exclusion is important since the contributions from neutrino cannot be measured and is referred to as the Missing Transverse Energy ($E_T^{miss}$). Therefore, it was decided to place cuts on $H_{\mathrm{T}}$ as it does include the contributions from neutrinos.

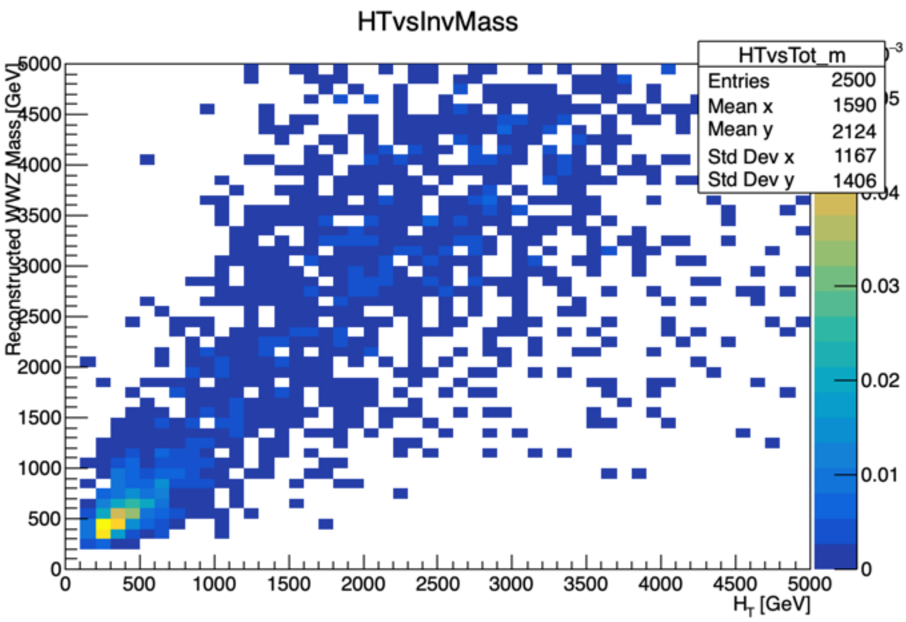


Figure 4.9: `InvMass_WWZ` Vs $H_{\mathrm{T}}$ for the M5 sample

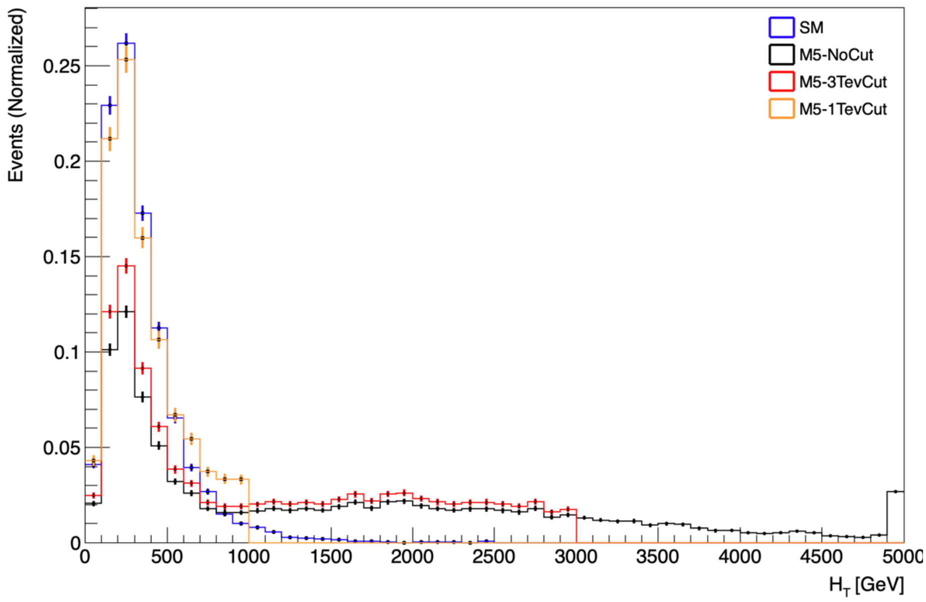


Figure 4.10: $H_{\mathrm{T}}$ for the SM (blue), `M5-NoCut` (black), `M5-3TeVCut` (red) and `M5-1TeVCut` (in orange) samples, with only the statistical uncertainties being displayed. The last bin contains the overflow. The events are normalized to one.

In the high-$p_{\mathrm{T}}$ region, the `M5-NoCut` sample displays a long tail, while the `SM` sample does not in this region beyond $H_{\mathrm{T}} = 3$ TeV. This is the motivation behind choosing a first cut of $\Lambda = 3$TeV. The limits on operators mentioned in Table 3.2 are normalized to $\Lambda = 1$ TeV, motivating a second cut at this value. $\Lambda$ is the energy scale at which the validity of the EFT is being probed.

The `M5-3TeVCut` also displays a high-$p_{\mathrm{T}}$ tail, until its sharp cut off at $H_{\mathrm{T}} = 3$ TeV. On the other hand there is a near-identical overlap in the low-$p_{\mathrm{T}}$ region, between the `SM` and `M5-1TeVCut` samples, including their peaks in the range of 300 – 400 GeV. This indicates that the aQGC samples dominates in the high-$p_{\mathrm{T}}$ region while `SM` is dominant in the low-$p_{\mathrm{T}}$ region, with large fluctuations indicating interference effects in the intermediate energy scales between 700 – 3000 GeV.

The extremely close overlap of `SM` and `M5-1TeVCut` shows that $H_{\mathrm{T}} = 1$TeV proves to be a stringent cut on the effective theory and reduces the impact of aQGC operators on kinematics significantly and at this energy scale the effective theory is nearly identical to the SM itself. It can be further understood that the boosting of the bosons due to the inclusion of EFT operators is nullified to a large extent by placing stringent cuts on EFT models and thereafter such EFT models are a good approximation to SM itself (since SM term is the LO term in the perturbative expansion of EFT).

## 4.4 Replicated Figures - Post Kinematic Cuts

A number of kinematic distributions can be obtained from the three reconstructed boson candidates, and are described below. These variables form a set of discriminating observables useful to indicate the presence of aQGC. It is important to identify such observables in order to achieve the main objective of this thesis: to understand how the $W^-W^+Z$ production is affected due to the presence of EFT operators. The impact on kinematic observables due to the imposition of cuts is seen by comparing

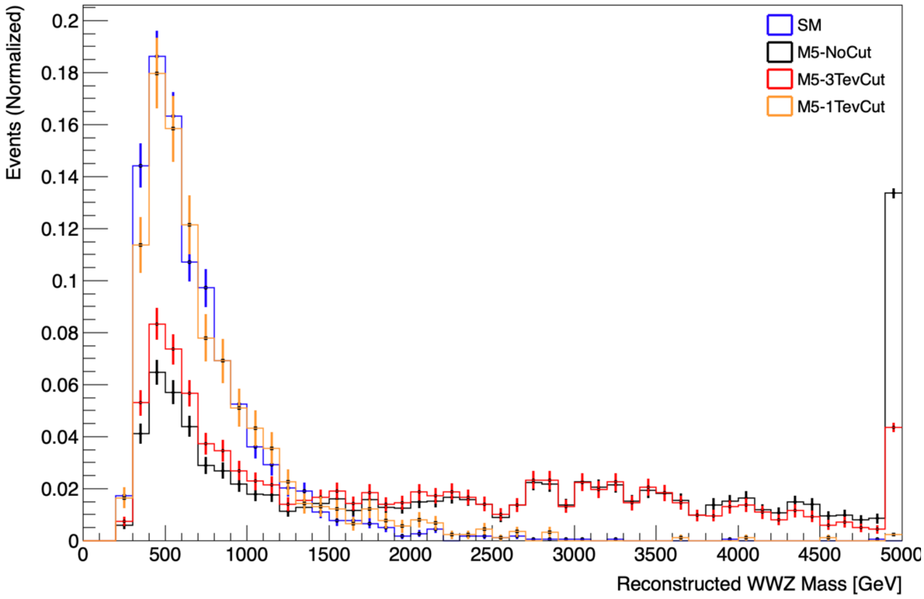


Figure 4.11: The invariant mass of the *WWZ* system for SM (blue), `M5-NoCut` (black), `M5-3TeVCut` (red) and `M5-1TeVCut` (orange) samples, with the statistical uncertainties being displayed. The last bin contains the overflow. The events are normalized to one.

both samples with cuts and without cuts in the same distribution. Therefore, these histograms are shown again in the following subsection by also including the samples with cuts as defined in Table 4.1.

The cut-flow histogram in Figure 4.12 shows that all the M5 samples with cuts have a reduced number of events after passing jet and lepton selection in comparison to the `SM` sample. The `M5-1TeVCut` sample is the most affected with least number of jet and lepton events in comparison to other samples. This indicates that the kinematic cut affects not just the nature of distributions of observables but also event selections.

In the distribution showing the number of jets in Figure 4.13, the `M5-3TeVCut` and `M5-NoCut` samples have many single-jets compared to SM. This is due to the imperfect resolution of boosted jets by the $anti - k_T$ algorithm. Also, nearly half of all events have precisely a pair of jets for `SM` while it is reduced for the boosted samples. The more boosted a sample is (like `M5-NoCut`), the lesser the number of events with well resolved jets.

From the invariant masses of single jets in Figure 4.14, it can be understood that the cuts result in smaller number of single jet events that could be candidates for $W$ boson. This is an indication that imposing cuts could impact on the boosted nature of EFT operators. This can be seen from the similar behavior of the `SM` and `M5-1TeVCut` samples. They populate the low mass region, while the boosted samples are dominant at higher values. It reconfirms that EFT operators causes boosting of jets and hence few of these single jets could themselves be candidates for the hadronically decaying $W$ boson.

The reconstruction of boson candidates was described in Section 4.2. The same procedure is repeated for the reconstruction of samples of the `SM`, `M5-1TeVCut`, `M5-3TeVCut` and `M5-NoCut` and displayed in Figures 4.15, 4.16 and 4.17. There is no discernible difference between the distributions and hence reconstructed invariant masses will not be useful variables for discriminating between aQGC and SM. The small peak close to zero seen in Figure 4.17 is due to extremely low-$p_T$ neutrinos as they do not need to pass any baseline cut.

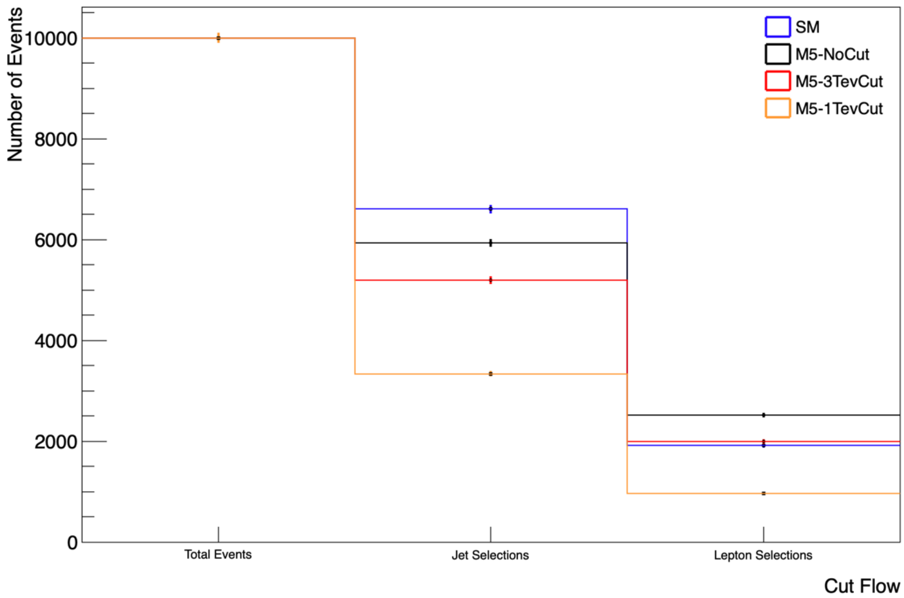


Figure 4.12: The total number of events in the first bin, events passing jet constraints in the second bin and after lepton requirements in the third bin for `SM` (blue), `M5-NoCut` (black), `M5-3TeVCut` (red) and `M5-1TeVCut` (orange) samples, with only the statistical uncertainties being displayed.

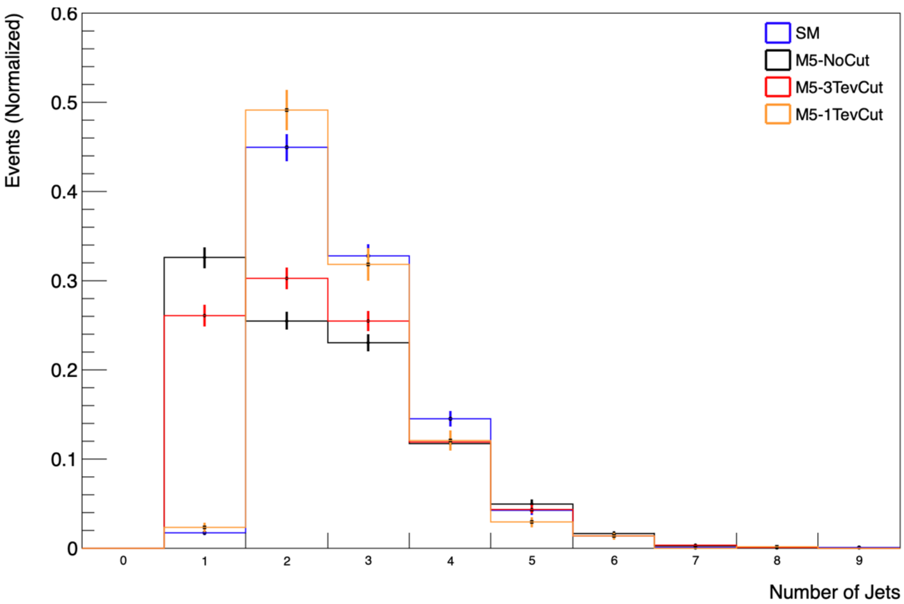


Figure 4.13: The number of jets after requiring at least one jet and $p_{\mathrm{T,Jet}} > 25$ GeV for `SM` (in blue), `M5-NoCut` (in black), `M5-3TeVCut` (in red) and `M5-1TeVCut` (in orange) samples, with only the statistical uncertainties being displayed. The events are normalized to one.

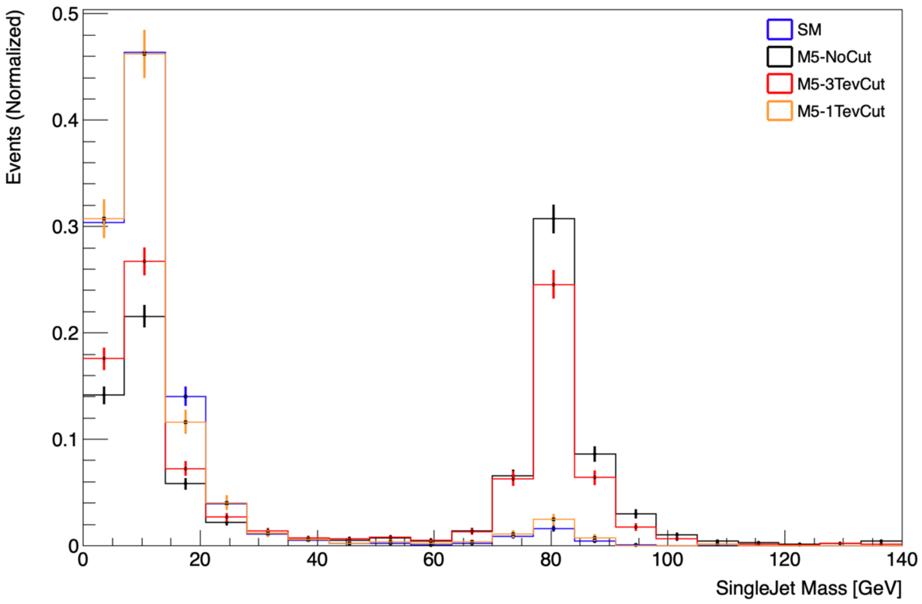


Figure 4.14: The invariant mass of the jet for events with one jet after requiring $p_{\mathrm{T,Jet}} > 25$ GeV for `SM` (blue), `M5-NoCut` (black), `M5-3TeVCut` (red) and `M5-1TeVCut` (orange) samples, with only the statistical uncertainties being displayed. The last bin contains overflow. The events are normalized to one.

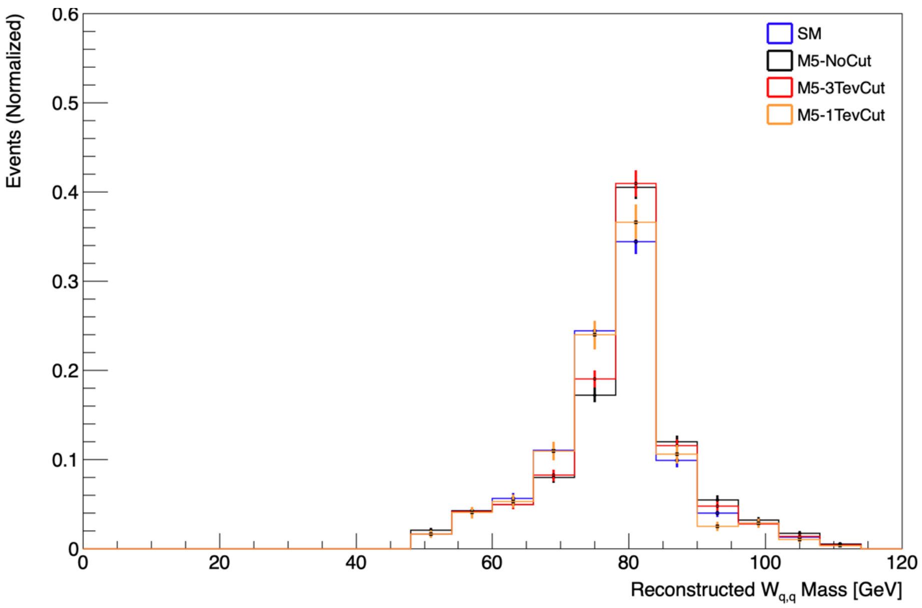


Figure 4.15: The invariant mass of all possible pairs of jets, for the `SM` (blue), `M5-NoCut` (black), `M5-3TeVCut` (red) and `M5-1TeVCut` (orange) samples, with only the statistical uncertainties being displayed. The events are normalized to one.

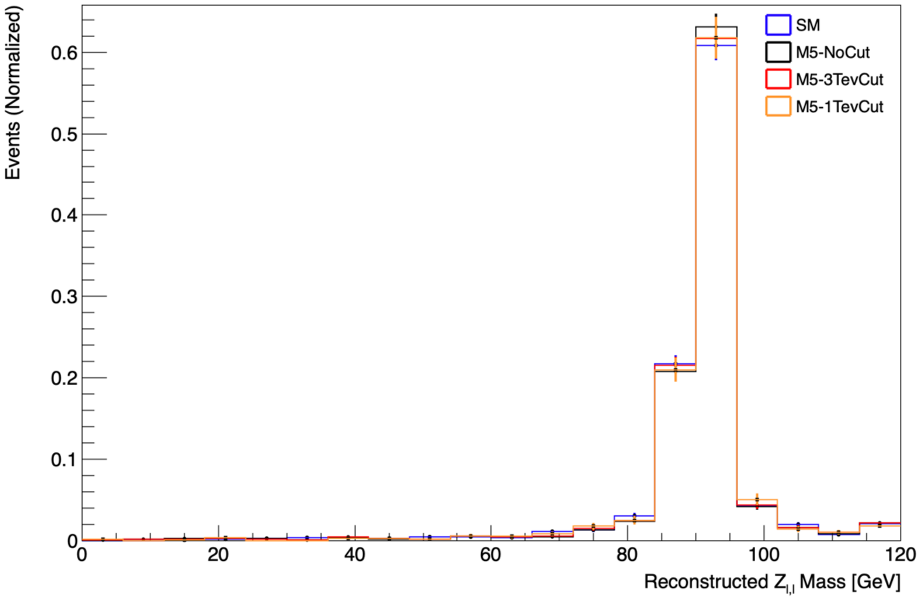


Figure 4.16: The invariant mass of all possible pairs of opposite-sign-same-flavored leptons, for the `SM` (blue), `M5-NoCut` (black), `M5-3TeVCut` (red) and `M5-1TeVCut` (orange) samples, with only the statistical uncertainties being displayed. The events are normalized to one.

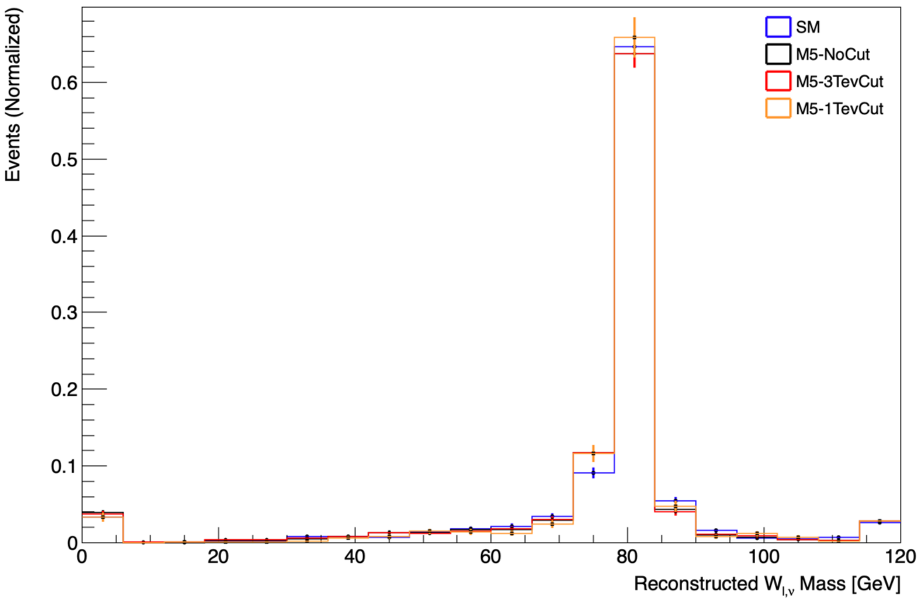


Figure 4.17: The invariant mass of the candidates from the hardest remaining lepton and the hardest neutrino, for the `SM` (blue), `M5-NoCut` (black), `M5-3TeVCut` (red) and `M5-1TeVCut` (orange) samples with only the statistical uncertainties being displayed. The events are normalized to one.

## 4.5 Discriminating Variables

The identification of discriminating variables is necessary to establish the sensitivity to aQGC operators. From the figures of invariant masses (Figures 4.15, 4.16 and 4.17), it can be seen that only tiny differences are observed in the behavior between the `SM` and different `M5` samples. Therefore, the invariant mass is unsuitable as a discriminating variable.

Since the M5 (or other aQGC) sample is boosted, the transverse momenta of the constituent objects and the differences in their angular values, are a very useful discriminants. Due to the effects of the cuts on the EFT samples, the distributions of `M5-3TeVCut` and `M5-1TeVCut` have lower peaks and shorter $p_T$ tails and consequently will be less discriminating than the `M5-NoCut` sample. Therefore, it would be beneficial to use samples without placing any cuts for comparing with SM, in order to obtain a large discrimination between the two samples. Though the discrimination is clearly visible for certain variables, a statistical test will be employed for quantifying the discriminating power of these variables (Section 4.5.4).

### 4.5.1 Transverse Momentum of Boson Candidates

The reconstruction of candidates for the three bosons was described in Section 4.2. Once the candidate have been obtained, it is possible to access a number of kinematic quantities including the transverse momenta and angular variables. The bosons are boosted due to the inclusion of EFT operators. These bosons are reconstructed with different constituents. Therefore, combining both features mentioned above, this provides a handle to understand the impact of EFT operators. The transverse momenta of the candidates discriminate the aQGC models against `SM` as displayed in Figures 4.18, 4.19, 4.20.

In the figures listed above, the EFT operator samples (`M5-NoCut` (black), `M5-3TeVCut` (red) and `M5-1TeVCut` (orange)) have shorter tails in the case of leptons as compared to jets. The cuts imposed on the samples affect on their respective distributions. This can be clearly seen from the reduced overflow in the last bin for `M5-3TeVCut` compared to `M5-NoCut` sample. The `M5-1TeVCut` is significantly impacted from the cut as can be seen by its exponential decrease similar to the behavior of `SM`, apart from its tail being non-existent in the region beyond 1200 GeV.

### 4.5.2 Transverse Momentum of Leading Objects

An object (jet/lepton) with highest value of transverse momenta is referred to as a leading object. The distributions of such leading objects are useful to gain an understanding of the behavior of individual objects after imposing the kinematic cuts. The leptons and jets are identified based on the MC particle numbering scheme defined in Reference [54]. The transverse momenta of the leading objects will prove to be useful in discriminating against `SM`.

The leading `electron`, leading `muon` and leading `jet` is displayed in Figures 4.21, 4.22, 4.23 respectively. These distributions mimic the trend as seen in Figure 4.10. The high-$p_T$ tail is found to be longer in the case of the leading jet as compared to the leading leptons. This is also seen through the overflows for each figure, with larger overflows in the case of jets than leptons.

This indicates that the kinematic cut affects leptons much more than jets. It must be noted that in the case of leptons, there are three charged leptons in every event. On the other hand, the majority of the events (nearly 60% of events for the `M5-NoCut` sample) have either single-jets or a pair of jets. Therefore, statistically, the leptons are more susceptible to be affected by kinematic cuts than jets.

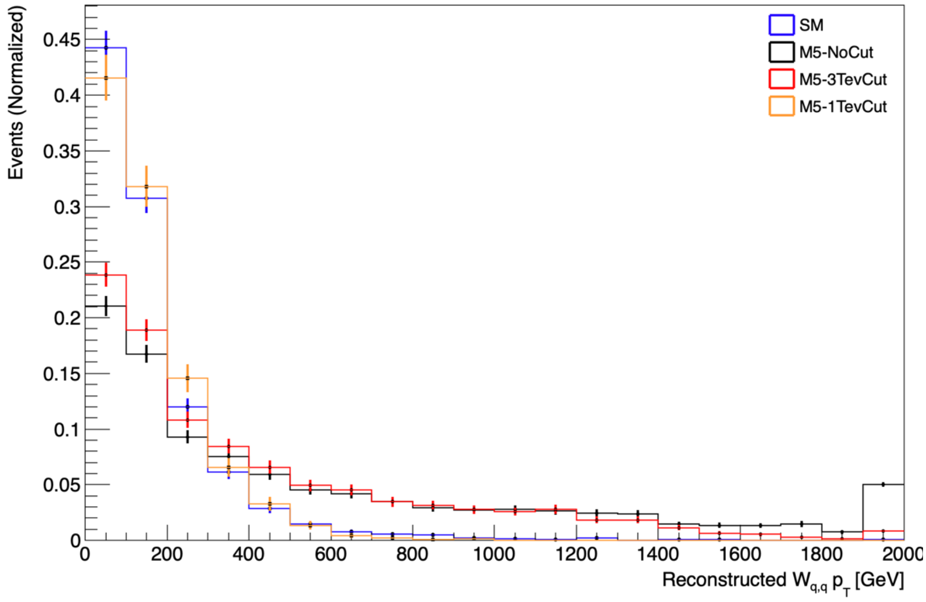


Figure 4.18: Transverse momentum of the hadronically decaying $W$ boson candidate for the `SM` (blue), `M5-NoCut` (black), `M5-3TeVCut` (red) and `M5-1TeVCut` (orange) samples, with only the statistical uncertainties being displayed. The last bin contains overflow. The events are normalized to one.

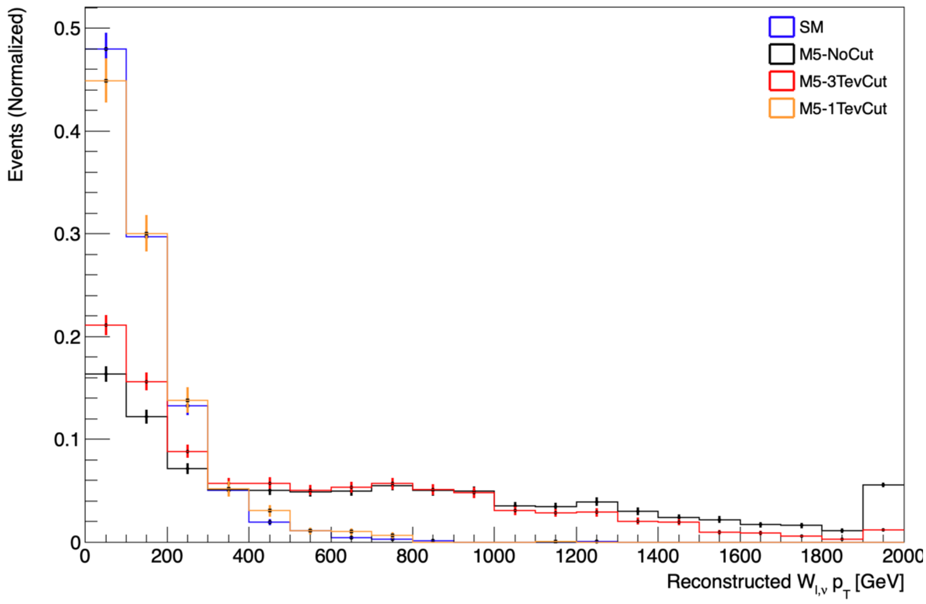


Figure 4.19: Transverse momentum of the leptonically decaying $W$ boson candidate for the `SM` (blue), `M5-NoCut` (black), `M5-3TeVCut` (red) and `M5-1TeVCut` (orange) samples, with only the statistical uncertainties being displayed. The last bin contains overflow. The events are normalized to one.

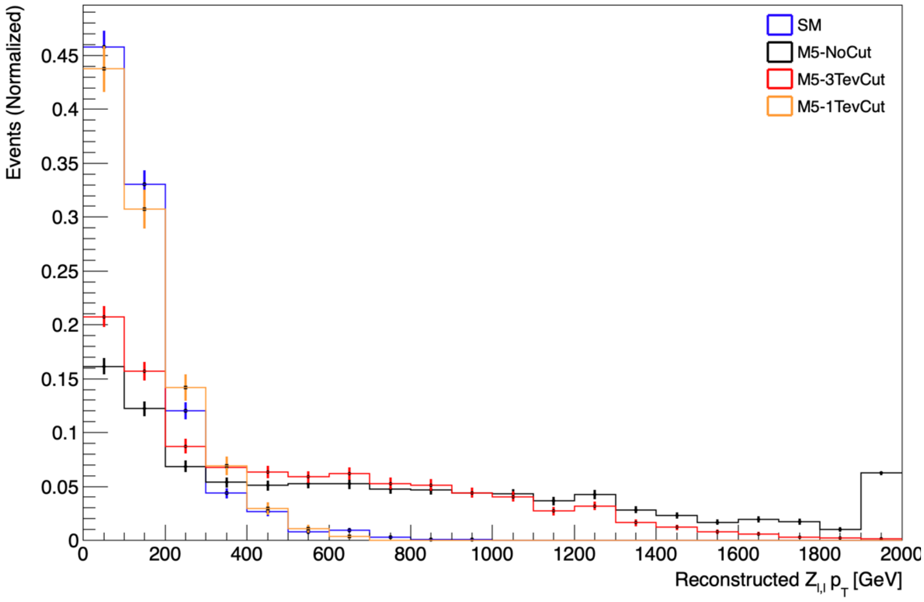


Figure 4.20: Transverse momentum of the leptonically decaying $Z$ boson candidate for the `SM` (blue), `M5-NoCut` (black), `M5-3TeVCut` (red) and `M5-1TeVCut` (orange) samples, with only the statistical uncertainties being displayed. The last bin contains overflow. The events are normalized to one.

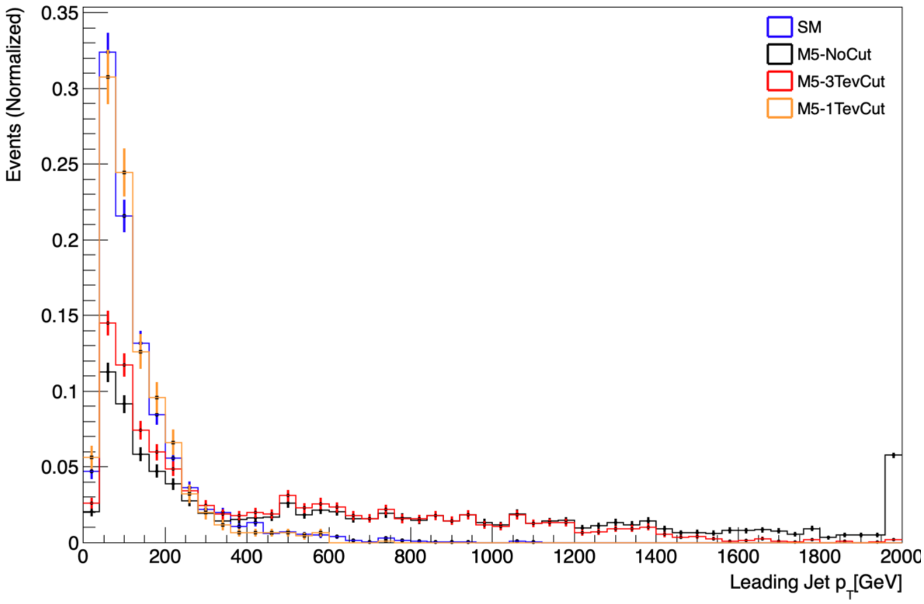


Figure 4.21: Transverse momentum of the leading jet candidate for the `SM` (blue), `M5-NoCut` (black), `M5-3TeVCut` (red) and `M5-1TeVCut` (orange) samples, with only the statistical uncertainties being displayed. The last bin contains overflow. The events are normalized to one.

### Missing Transverse Energy

In experimental particle physics, missing transverse energy ($E_T^{miss}$) is the energy that cannot be detected in a particle detector. Though undetected in the detectors, its presence can be inferred from

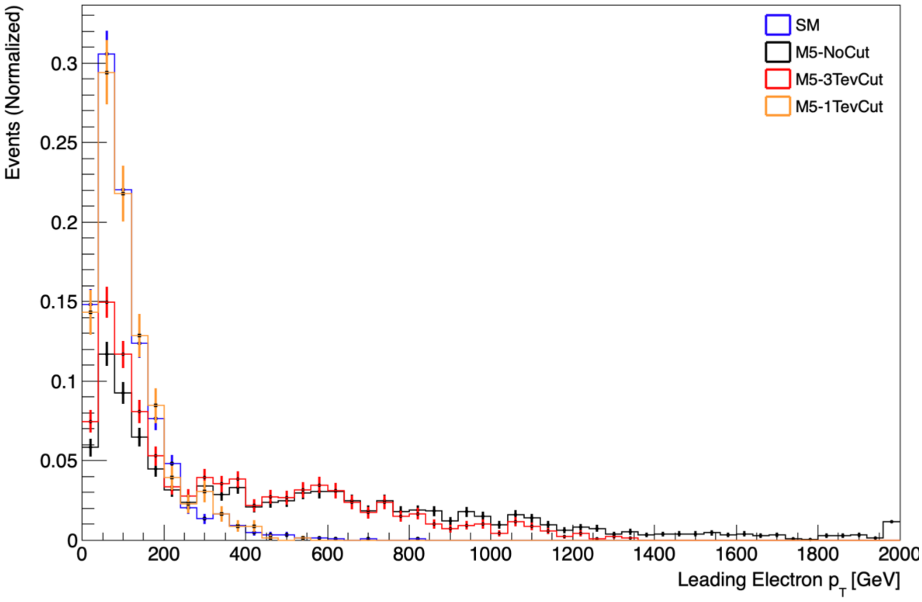


Figure 4.22: Transverse momentum of the leading electron candidate for the `SM` (blue), `M5-NoCut` (black), `M5-3TeVCut` (red) and `M5-1TeVCut` (orange) samples, with only the statistical uncertainties being displayed. The last bin contains overflow. The events are normalized to one.

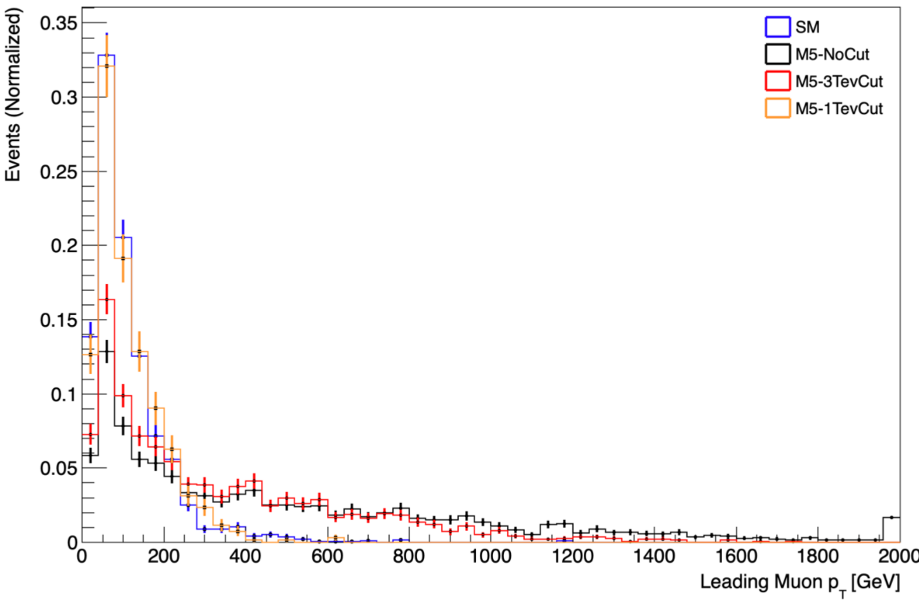


Figure 4.23: Transverse momentum of the leading muon candidate for the `SM` (blue), `M5-NoCut` (black), `M5-3TeVCut` (red) and `M5-1TeVCut` (orange) samples, with only the statistical uncertainties being displayed. The last bin contains overflow. The events are normalized to one.

the laws of conservation of energy and conservation of momentum. $E_T^{miss}$ is carried by particles, like neutrinos, quantifies the momentum of invisible particles that cannot be detected. It is displayed in

Figure 4.24. The behavior of the M5 samples continues to follow the same pattern as earlier, with slightly lower overflows for `M5-3TeVCut` than `M5-NoCut`. Also, the `M5-1TeVCut` sample behaves similar to `SM` with slightly longer tail in transverse momenta.

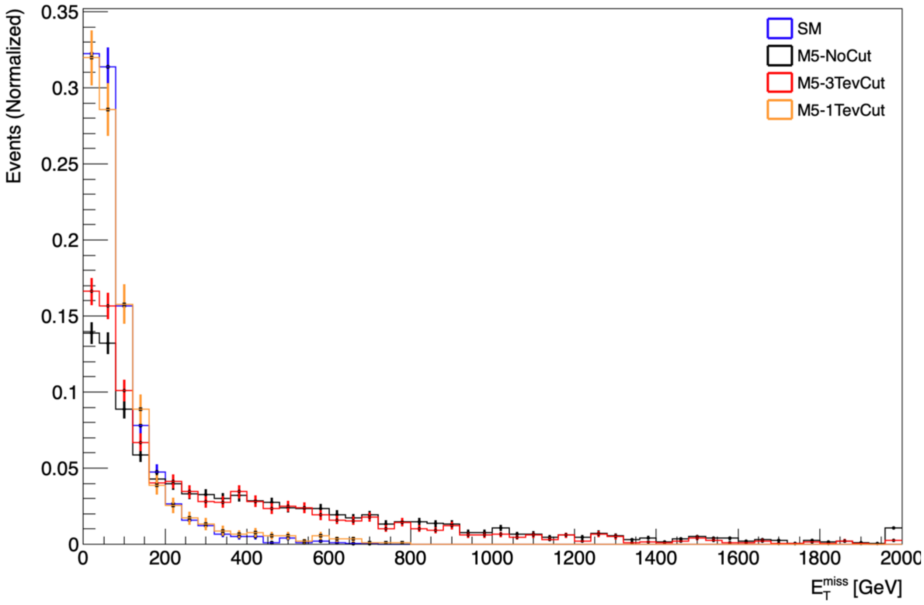


Figure 4.24: The missing transverse energy ($E_T^{miss}$) for `SM` (blue), `M5-NoCut` (black), `M5-3TeVCut` (red) and `M5-1TeVCut` (orange) samples, with only the statistical uncertainties being displayed. The last bin contains overflow. The events are normalized to one.

### 4.5.3 Angular Variables

Similar to the transverse momenta of the candidates of three bosons, the angular variables ($\phi$, $\eta$ and $\Delta R$ defined in References [3, 8] of individual jets and individual leptons that are involved in the reconstruction of bosons, are also useful for their discriminating power against `SM`.

The values of $\phi$ would directly impact the values obtained for $p_T$ for the given system. For example, in the case of two-body decay like a $\rightarrow$ b + c, its useful to obtain the difference in $\Phi$ for final state particles "b" and "c". The $\Delta\phi$ is obtained by taking the difference in $\phi$ for constituent objects that were utilized in the reconstruction of respective candidates for bosons. Figure 4.25 displays $\Delta\phi$ between the pair of jets that constitute the hadronically decaying $W$ boson candidate and Figure 4.26 displays $\Delta\phi$ between the remaining lepton and $E_T^{miss}$ for leptonically decaying $W$ boson. Lastly, between the pair of leptons decaying from $Z$ boson in the Figure 4.27.

There are a larger number of events at $\Delta\phi = 0$ for the `M5-3TeVCut` and `M5-NoCut` samples. With $\Delta\phi = 0$ (between pair of jets, between pair of opposite sign leptons and finally between the other lepton and $E_T^{miss}$), results in these objects being very close to each other in the transverse plane as they are boosted. The impact of the cuts can be seen from the fact that the peak at $\Delta\phi = 0$ is slightly reduced for `M5-3TeVCut` and is non-existent for `M5-1TeVCut`. Due to the large gap at $\Delta\phi = 0$ when leptons are involved as compared to jets, the variables $\Delta\phi(\ell, \mathrm{MET})$ and $\Delta\phi(\ell, \ell)$ turns out to be a better discriminant than $\Delta\phi(j, j)$.

The Pseudo-Rapidity($\eta$) describes the angle of a particle relative to the beam axis. The Figure 4.28 displays $\Delta\eta$ between the pair of jets that constitute the hadronically decaying $W$ boson candidate, between the pair of leptons decaying from the $Z$ boson in Figures 4.29, 4.30 for the remaining lepton and $\nu$ for leptonically decaying $W$ boson respectively.

If $\theta = 0$, the particle is moving along the beam axis, and hence particles with high $|\eta|$ values are generally lost, escaping from the detector along with the beam. There are a large number of events at $\Delta|\eta| = 0$ for `M5-3TeVCut` and `M5-NoCut` samples. However, `SM` decays exponentially and overlaps with `M5-1TeVCut`. The impact of cuts can be seen from the fact that the peak at $\Delta\phi = 0$ is marginally reduced for `M5-3TeVCut` and significantly reduced for `M5-1TeVCut`. Similar to the case of $\Delta\phi$, the large gap at $\Delta|\eta| = 0$, when leptons are involved as compared to jets, the variables $|\Delta\eta|(\ell, \nu)$ and $|\Delta\eta|(\ell, \ell)$ turns out to be a better discriminant than $|\Delta\eta|(j, j)$.

The spatial distance $\Delta R$ is defined to be :

$$\Delta R = \sqrt{(\Delta\phi)^2 + (\Delta\eta)^2} \tag{4.2}$$

and is useful to obtain a measure of the distance between objects in three-dimensional space. It is shown in Figures 4.31, 4.32, 4.33. The $\Delta R$ parameter is a representation of combination of effects from both angular variables. Due to the imperfect resolution of boosted jets, they are closely clustered and is likely to be moving in the same direction, as can be confirmed from Figure 4.31, with low values of separation between the jets. However, the leptons suffer no issues in its resolution and continues to be clearly discriminating due to its large discriminant across the entire range of values.

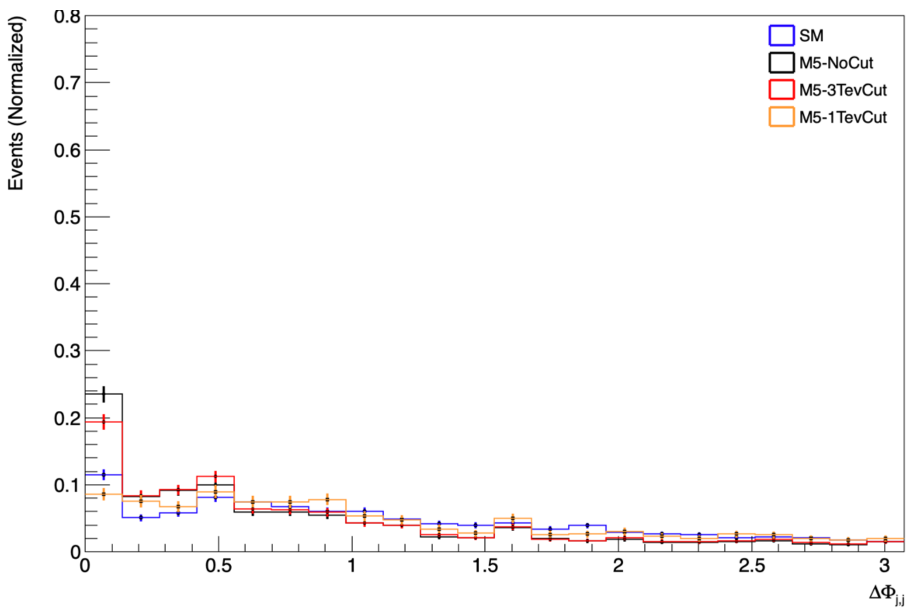


Figure 4.25: The $\Delta\phi$ between pair of jets for `SM` (blue), `M5-NoCut` (black), `M5-3TeVCut` (red) and `M5-1TeVCut` (orange) samples, with only the statistical uncertainties being displayed. The events are normalized to one.

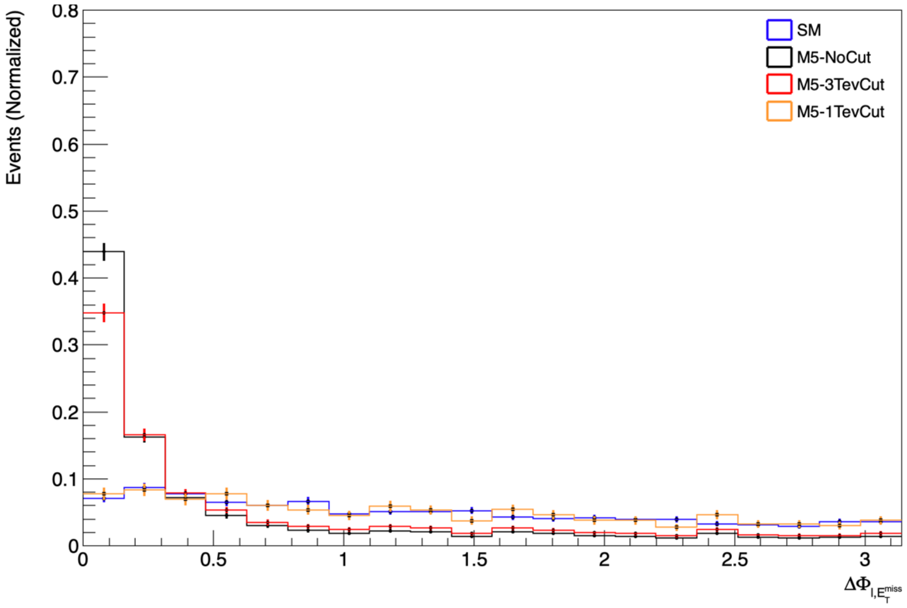


Figure 4.26: The $\Delta\phi$ between between remaining lepton and $E_T^{miss}$ for `SM` (blue), `M5-NoCut` (black), `M5-3TeVCut` (red) and `M5-1TeVCut` (orange) sampless, with only the statistical uncertainties being displayed. The events are normalized to one.

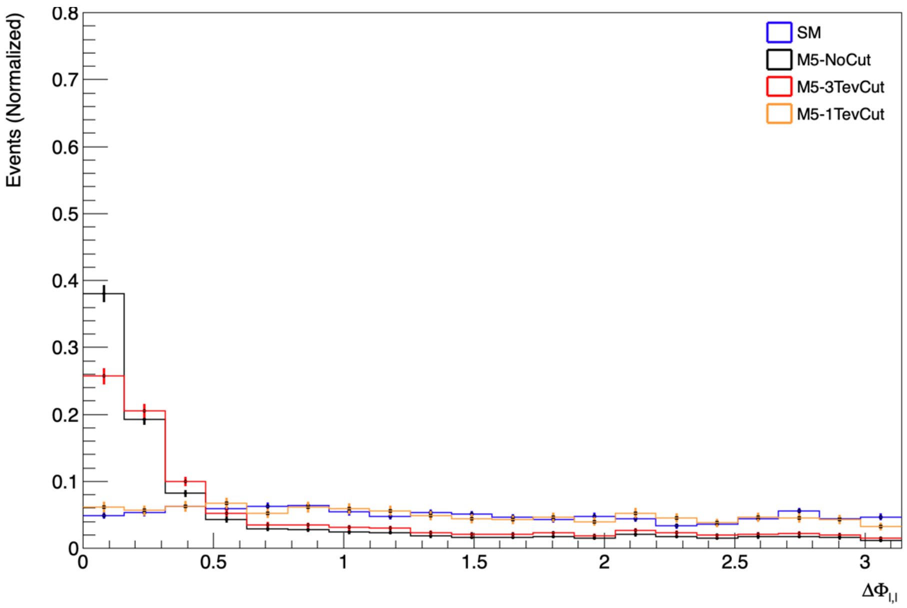


Figure 4.27: The $\Delta\phi$ between between pair of opposite sign same flavor leptons for `SM` (blue), `M5-NoCut` (black), `M5-3TeVCut` (red) and `M5-1TeVCut` (orange) samples, with only the statistical uncertainties being displayed. The events are normalized to one.

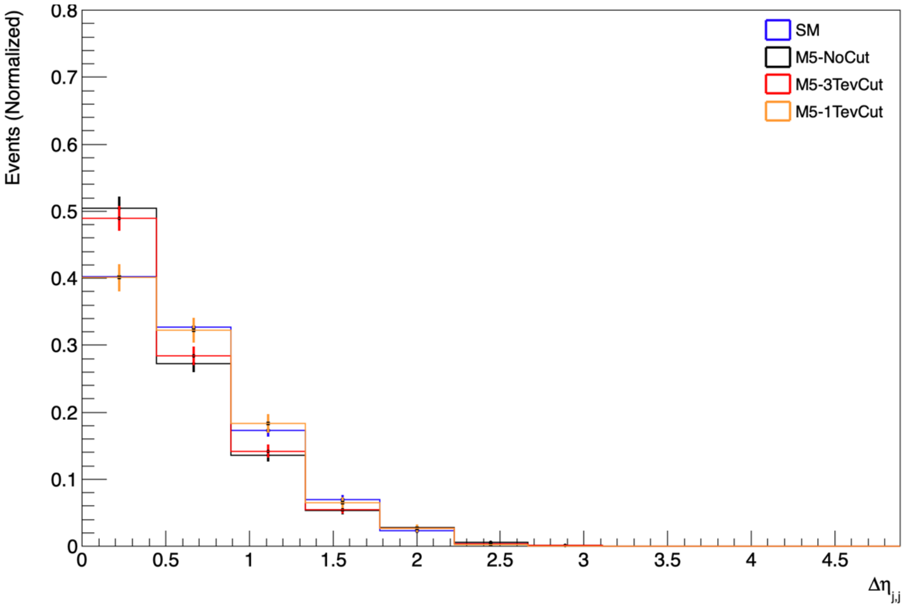


Figure 4.28: The $\Delta\eta$ between pair of jets for `SM` (blue), `M5-NoCut` (black), `M5-3TeVCut` (red) and `M5-1TeVCut` (orange) samples, with only the statistical uncertainties being displayed. The events are normalized to one.

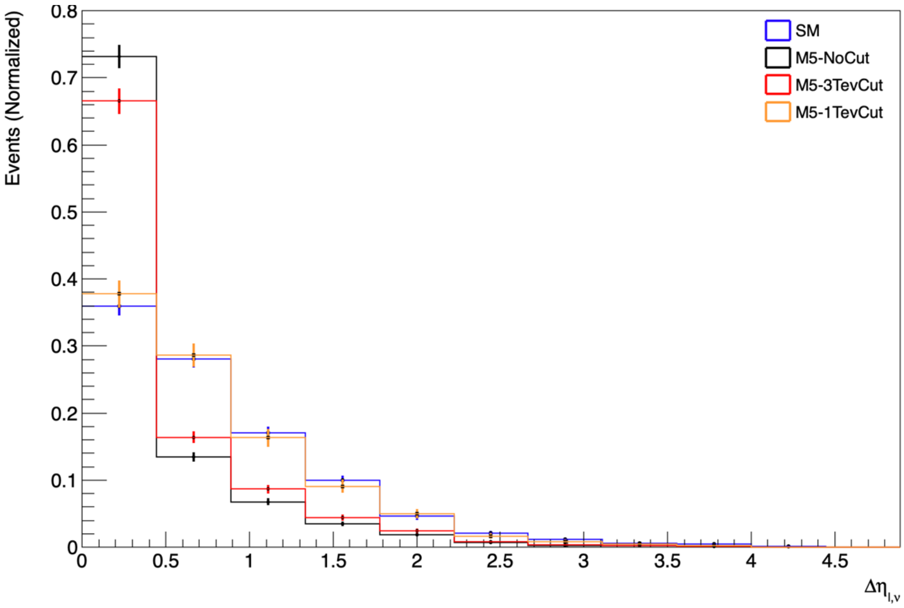


Figure 4.29: The $\Delta\eta$ between between remaining lepton and neutrino (with hardest $p_T$) for `SM` (blue), `M5-NoCut` (black), `M5-3TeVCut` (red) and `M5-1TeVCut` (orange) samples, with only the statistical uncertainties being displayed. The events are normalized to one.

### 4.5.4 Kolmogorov-Smirnov Test

The Komogorov-Smirnov (KS) test [55, 56] is a statistical test useful for determining the compatibility in shape between the two distributions. It can be inferred from the earlier subsections that the

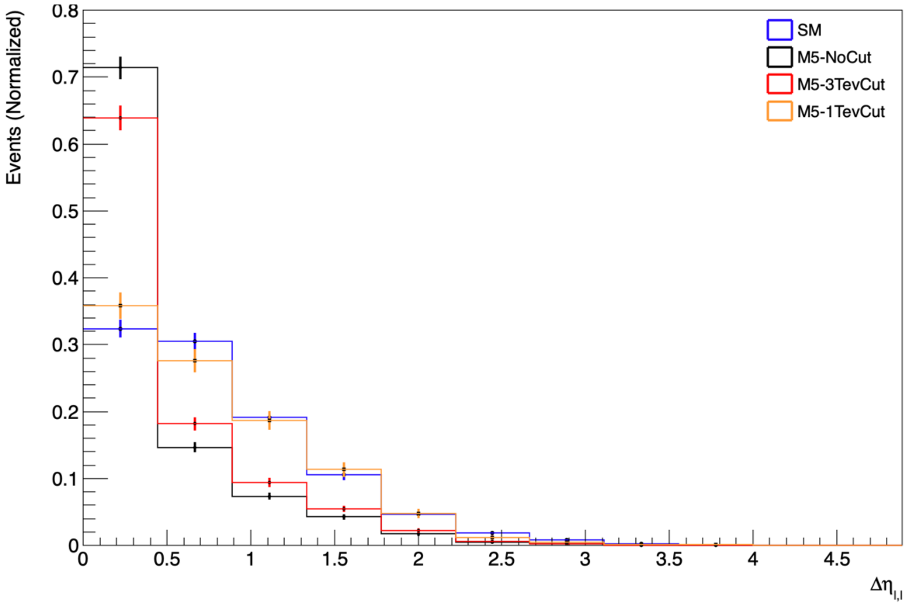


Figure 4.30: The $\Delta\eta$ between between pair of opposite sign same flavor leptons for `SM` (blue), `M5-NoCut` (black), `M5-3TeVCut` (red) and `M5-1TeVCut` (orange) samples, with only the statistical uncertainties being displayed. The events are normalized to one.

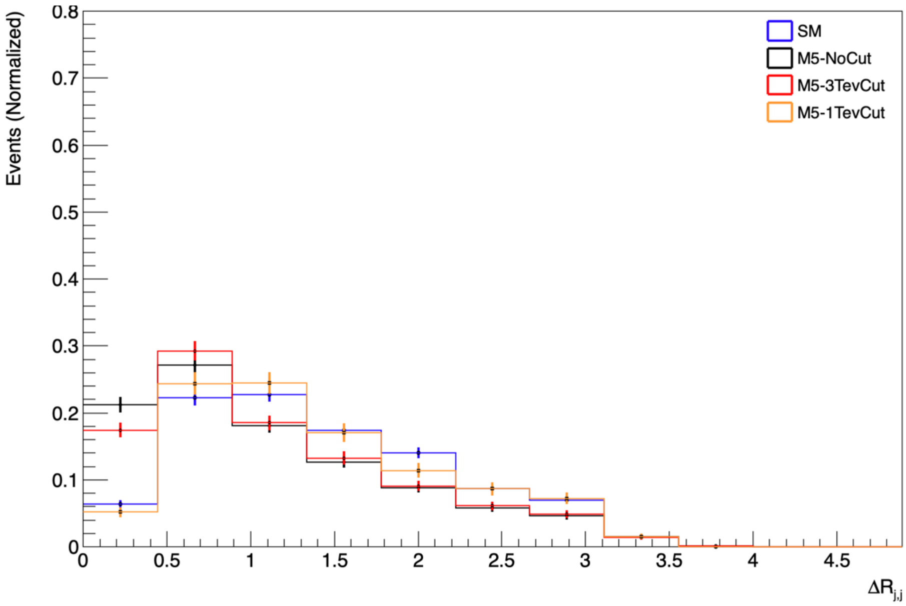


Figure 4.31: The ΔR between pair of jets for `SM` (blue), `M5-NoCut` (black), `M5-3TeVCut` (red) and `M5-1TeVCut` (orange) samples, with only the statistical uncertainties being displayed. The events are normalized to one.

`M5-NoCut` sample offers the largest discriminating power among the three samples, for a number of kinematic variables displayed so far. The objective of performing the KS test is to identify kinematic variables for each sample that offers the largest discriminant in comparison to the `SM` sample.

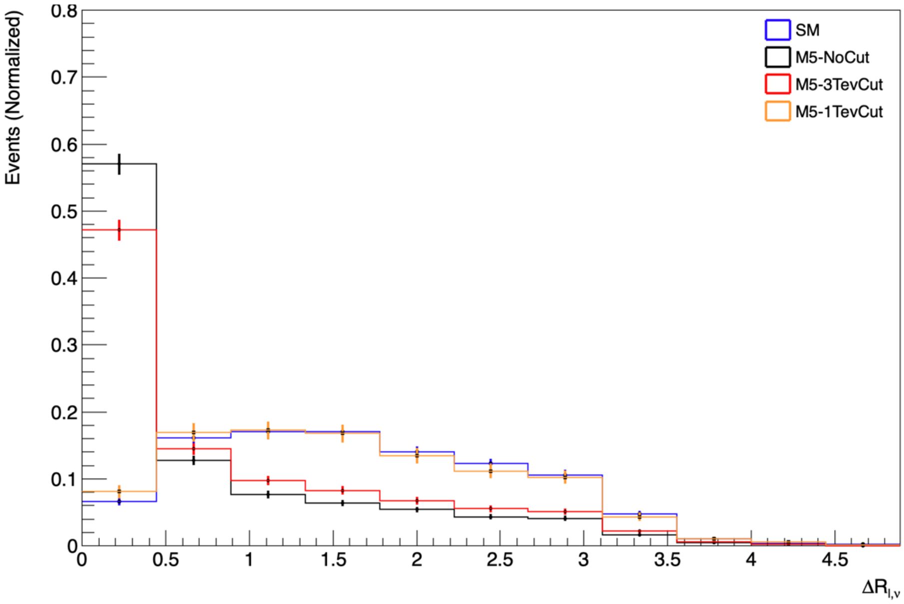


Figure 4.32: The ΔR between between remaining lepton and neutrino (with hardest $p_T$ ) for `SM` (blue), `M5-NoCut` (black), `M5-3TeVCut` (red) and `M5-1TeVCut` (orange) samples, with only the statistical uncertainties being displayed. The events are normalized to one.

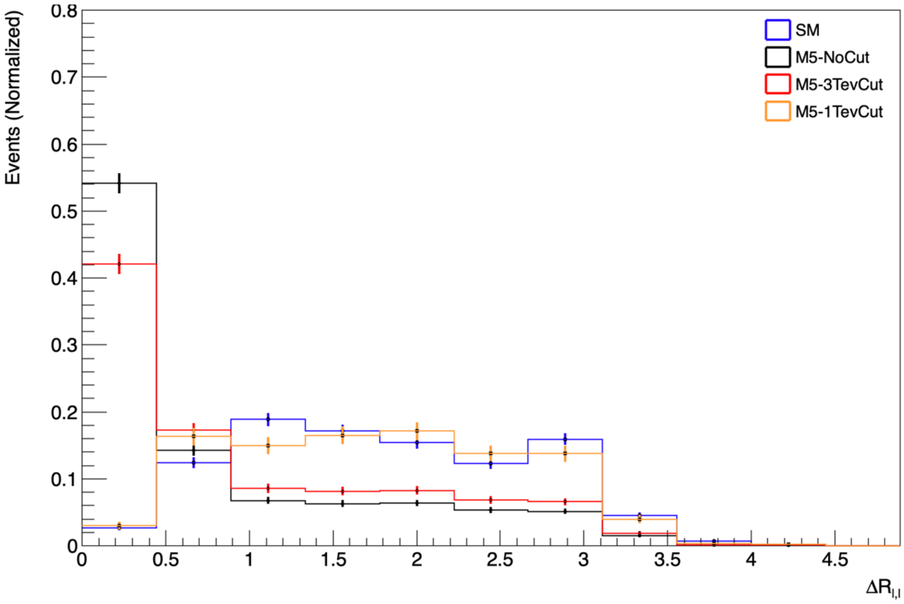


Figure 4.33: The ΔR between between pair of opposite sign same flavor leptons for `SM` (blue), `M5-NoCut` (black), `M5-3TeVCut` (red) and `M5-1TeVCut` (orange) samples, with only the statistical uncertainties being displayed. The events are normalized to one.

By performing the KS test between two figures, the test returns a value (by default) between 0–1, which is the probability of test (much less than one would mean that the figures are not compatible).

One must also bear in mind the remarks by Jan Conrad and Fred James in Reference [55] that "the returned value of probability is calculated such that it will be uniformly distributed between zero and one for compatible histograms, provided the data are not binned (or the number of bins is very large compared with the number of events)".

Similarly, it also possible to obtain the "Kolmogorov Distance" between the two figures, which is the chosen quantity for this study. A detailed review for calculating Kolmogorov Distance can be found in [57]. It is especially useful to quantify the distance (i.e. non-compatibility or non-overlap) between the two distributions and thereby helps in identifying the most suitable discriminating variable, for a given sample of events. Therefore, the most discriminating variable will have the largest values of the Kolmogorov distance.

The values of Kolmogorov distances obtained for `M5-NoCut`, `M5-3TeVCut` and `M5-1TeVCut` samples in comparison to `SM`, are enlisted in Table 4.2 for all studied discriminating variables. The transverse momenta of the $Z$ boson candidate is the best discriminant among all the variables considered in the study.

Among the angular variables, the $\Delta\phi$ between the pair of opposite sign same flavor leptons is the most discriminating variable, while the $\Delta\eta$ between pair of jets is not very well suited for the purpose of discriminating between SM and aQGC. Therefore, it can be concluded that leptons (which reconstruct $Z$ boson) offer the best discrimination among all variables considered.

The `M5-NoCut` sample offers the largest discrimination when comparing distributions. On the other hand, `M5-1TeVCut` is unsuitable for identifying discriminating variables. It must also be noted that though the KS test provides a means for quantifying the discriminating variables, only the values of KS distances will not be sufficient to conclude about the discriminating power of a given variable. It is important to ensure that the respective variables are also reconstructed efficiently.

| Variable (Reference) | `M5-NoCut` | `M5-3TeVCut` | `M5-1TeVCut` |
|---|---|---|---|
| **Transverse Momenta of Candidates of Bosons** | | | |
| Whad_pt_q_q (refer to Figure 4.18 ) | 0.398 | 0.333 | 0.027 |
| Wlep_pt_l_nu (refer to Figure 4.19 ) | 0.551 | 0.453 | 0.030 |
| Z_pt_l_l (refer to Figure 4.20) | 0.555 | 0.455 | 0.043 |
| **Transverse Momenta of Leading Objects** | | | |
| leadingjet_pt (refer to Figure 4.21 ) | 0.506 | 0.388 | 0.037 |
| leadingelectron_pt (refer to Figure 4.22 ) | 0.513 | 0.413 | 0.018 |
| leadingmuon_pt (refer to Figure 4.23 ) | 0.505 | 0.399 | 0.033 |
| $E_T^{miss}$ (refer to Figure 4.24) | 0.457 | 0.387 | 0.030 |
| **Angular Variables** | | | |
| **$\Delta\phi$ between objects** | | | |
| Whad_dPhi_q_q (refer to Figure 4.25 ) | 0.205 | 0.177 | 0.038 |
| Wlep_dPhi_l_MET (refer to Figure 4.26 ) | 0.443 | 0.356 | 0.013 |
| Z_dPhi_l_l (refer to Figure 4.27 ) | 0.489 | 0.396 | 0.024 |
| **$\Delta\eta$ between objects** | | | |
| Whad_dEta_q_q (refer to Figure 4.28 ) | 0.102 | 0.086 | 0.007 |
| Wlep_dEta_l_nu (refer to Figure 4.29 ) | 0.371 | 0.305 | 0.023 |
| Z_dEta_l_nu (refer to Figure 4.30 ) | 0.389 | 0.314 | 0.034 |

Table 4.2: Kolmogorov distances for variables associated with transverse momenta and angular variables of objects for the `M5-NoCut`, `M5-3TeVCut` and `M5-1TeVCut` samples in comparison to `SM`. The most discriminating variables are highlighted.

# CHAPTER 5

# Summary and Outlook

This phenomenological study involved a sensitivity study for *WWZ* production to the presence of aQGC operators. The *WWZ* events were generated at LO using the `MadGraph5` event generator for different aQGC operators in the three-lepton channel. The $\sigma_{\mathrm{SM}}$ for WWZ production was found to be 89 fb. The most constraints of limits for the operators from different analyses was compiled and these limits were utilized to obtain the $\sigma_{\mathrm{aQGC}}$ and their deviations were calculated in comparison to $\sigma_{\mathrm{SM}}$. The M5 operator was found to have the maximum deviation with respect to SM and was chosen for further phenomenological study.

Event selection and reconstruction of boson candidates was carried out based on the invariant mass criterion. The inclusion of EFT operators causes boosting of the bosons for the EFT samples. The $anti-k_T$ algorithm is not suitable for the resolution of collimated jets, obtained from hadronically decaying $W$ boson. Therefore, it would be beneficial to use alternative algorithms. The validity of the EFT power expansion is probed by placing kinematic cuts for the values of $\Lambda = 3$ TeVand $\Lambda = 1$ TeV. The net effect of placing cuts is that the boosting of bosons is reduced significantly. The 1 TeVcut proves to be a stringent cut and reduces the EFT sample to be a close approximation of SM.

In the efforts towards identifying discriminating variables, it was found that the samples without imposing cuts offer the largest discrimination, while comparing distributions. Also, invariant masses of candidates are not useful as discriminating variables. Transverse momenta and angular variables are more effective in this regard. The transverse momenta of boson candidates in general, and specifically the $p_{\mathrm{T}}$ of $Z$ boson candidate is found to be the most discriminating variable. A KS test is employed to quantify the discrimination (through the values of the Kolmogorov distance by comparing with the SM) of different variables for a given sample. It is confirmed through the KS test that variables related to $Z$ boson offer the best discrimination in the case of M5 operator for both samples - with and without cuts.

As a next step, detector simulation shall be included. Currently, only one operator is switched on for generating samples of the particular aQGC operator. In order to probe interference effects, multiple operators shall be considered simultaneously.

# Bibliography


[1] *The Road Not Taken*,
https://www.poetryfoundation.org/poems/44272/the-road-not-taken.

[2] *Aryabhatta*, https://en.wikipedia.org/wiki/Aryabhata.

[3] M. Thomson, *Modern Particle Physics*. Cambridge University Press, 2013.

[4] ATLAS Collaboration, G. Aad et al., *Evidence for the production of three massive vector bosons with the ATLAS detector*, arXiv:1903.10415 [hep-ex].

[5] Particle Data Group Collaboration,, *Review of Particle Physics*, Phys. Rev. D **98** (2018) 030001, https://link.aps.org/doi/10.1103/PhysRevD.98.030001.

[6] *SM-Wikipedia*, https://en.wikipedia.org/wiki/Standard_Model#/media/File:Standard_Model_of_Elementary_Particles.svg.

[7] M. E. Peskin and D. V. Schroeder, *An Introduction to quantum field theory*. Addison-Wesley, Reading, USA, 1995. http://www.slac.stanford.edu/~mpeskin/QFT.html.

[8] M. D. Schwartz, *Quantum Field Theory and the Standard Model*. Cambridge University Press, 2013.

[9] F. Halzen and A. D. Martin, *Quarks and Leptons: An Introductory Course in Modern Particle Physics*. Wiley, 1984.

[10] S. L. Glashow, *Partial-symmetries of weak interactions*, Nuclear Physics **22** no. 4, (1961) 579 – 588.

[11] S. Weinberg, *A Model of Leptons*, Phys. Rev. Lett. **19** (1967) 1264–1266.

[12] A. Salam, *Weak and Electromagnetic Interactions*, Conf. Proc. **C680519** (1968) 367–377.

[13] *Andrea Sciandra – PhD Thesis: Probing the Standard Model of particle physics with ttH,WWZ and WZZ multi-lepton final states*,.

[14] M. Cristinziani, M. Franklin, N. M. Gubbi, V. Kostyukhin, J. Liu, J. Metcalfe, A. Milic, G. Rabanal Bolanos, A. Sciandra, I. Siral, S. Sun, B. Tong, A. N. Tuna, A. M. Wang, W. Xu, L. Zhang, and J. Zhu, *Evidence for VVV production in pp collisions at* $\sqrt{s} = 13$ *TeV*, Tech. Rep. ATL-COM-PHYS-2018-1648, CERN, Geneva, Nov, 2018. https://cds.cern.ch/record/2649213.

[15] A. Sciandra, M. Cristinziani, V. Kostyukhin, and N. M. Gubbi, *Search for WWZ and WZZ production in pp collisions at* $\sqrt{s} = 13$ *TeV*, Tech. Rep. ATL-COM-PHYS-2018-420, CERN, Geneva, Apr, 2018. `https://cds.cern.ch/record/2314648`.

[16] A. Pich, *The Standard Model of Electroweak Interactions*, pp. , 1–50. 2012. `arXiv:1201.0537 [hep-ph]`. [1(2012)].

[17] J. Woithe, G. J. Wiener, and F. F. V. der Veken, *Let's have a coffee with the Standard Model of particle physics!*, Physics Education **52** no. 3, (2017) 034001.

[18] S. P. Martin, *A Supersymmetry primer*, `arXiv:hep-ph/9709356 [hep-ph]`, [Adv. Ser. Direct. High Energy Phys.18,1(1998)].

[19] T. Appelquist and J. Carazzone, *Infrared singularities and massive fields*, Phys. Rev., D, v. 11, no. 10, pp. 2856-2861.

[20] M. Baak et al., *Working Group Report: Precision Study of Electroweak Interactions*, `https://inspirehep.net/record/1261993`.

[21] O. Eboli and M. Gonzalez-Garcia, *Anomalous quartic electroweak gauge-boson interactions*, `http://feynrules.irmp.ucl.ac.be/wiki/AnomalousGaugeCoupling#no1`.

[22] N. P. Hartland, F. Maltoni, E. R. Nocera, J. Rojo, E. Slade, E. Vryonidou, and C. Zhang, *A Monte Carlo global analysis of the Standard Model Effective Field Theory: the top quark sector*, `arXiv:1901.05965 [hep-ph]`.

[23] R. Contino, A. Falkowski, F. Goertz, C. Grojean, and F. Riva, *On the validity of the effective field theory approach to SM precision tests*, J. High Energy Phys. **2016** no. 7, (2016) 144.

[24] D. Barducci et al., *Interpreting top-quark LHC measurements in the standard-model effective field theory*, `http://cds.cern.ch/record/2305783`.

[25] A. Alloul, N. D. Christensen, C. Degrande, C. Duhr, and B. Fuks, *FeynRules 2.0 — A complete toolbox for tree-level phenomenology*, Computer Physics Communications **185** no. 8, (2014) 2250 – 2300.

[26] *Mathematica*, `https://www.wolfram.com/mathematica/`.

[27] J. Alwall, M. Herquet, F. Maltoni, O. Mattelaer, and T. Stelzer, *MadGraph 5: going beyond*, Journal of High Energy Physics **2011** no. 6, (2011) 128.

[28] T. Gleisberg, S. Hoeche, F. Krauss, M. Schonherr, S. Schumann, F. Siegert, and J. Winter, *Event generation with SHERPA 1.1*, JHEP **02** (2009) 007.

[29] J. Reuter, F. Bach, B. Chokoufe, W. Kilian, T. Ohl, M. Sekulla, and C. Weiss, *Modern Particle Physics Event Generation with WHIZARD*, J. Phys. Conf. Ser. **608** (2015) 012063.

[30] C. Degrande, C. Duhr, B. Fuks, D. Grellscheid, O. Mattelaer, and T. Reiter, *UFO – The Universal FeynRules Output*, Computer Physics Communications **183** no. 6, (2012) 1201 – 1214.

[31] *Python*, `https://www.python.org/`.

[32] J. Bellm et al., *Herwig 7.0/Herwig++ 3.0 release note*, Eur. Phys. J. **C76** no. 4, (2016) 196.

[33] *Rivet Home Page*, `https://rivet.hepforge.org/`.

[34] A. Buckley, J. Butterworth, L. Lonnblad, D. Grellscheid, H. Hoeth, J. Monk, H. Schulz, and F. Siegert, *Rivet user manual*, Comput. Phys. Commun. **184** (2013) 2803–2819.

[35] *Rivet Tutorial*, `https://indico.cern.ch/event/281744/attachments/517488/713992/rivet-tutorial.pdf`.

[36] F. Maltoni and T. Stelzer, *MadEvent: automatic event generation with MadGraph*, Journal of High Energy Physics **2003** no. 02, (2003) 027–027, `https://doi.org/10.1088%2F1126-6708%2F2003%2F02%2F027`.

[37] *MG5-Tutorial*, `https://twiki.cern.ch/twiki/bin/view/CMSPublic/MadgraphTutorial`.

[38] *aQGC-GitProject*, `https://gitlab.cern.ch/ngubbi/aQGC`.

[39] P. Artoisenet, R. Frederix, O. Mattelaer, and R. Rietkerk, *Automatic spin-entangled decays of heavy resonances in Monte Carlo simulations*, JHEP **03** (2013) 015.

[40] T. Sjöstrand, S. Ask, J. R. Christiansen, R. Corke, N. Desai, P. Ilten, S. Mrenna, S. Prestel, C. O. Rasmussen, and P. Z. Skands, *An introduction to PYTHIA 8.2*, Computer Physics Communications **191** (2015) 159 – 177.

[41] A. Buckley, J. Ferrando, S. Lloyd, K. Nordström, B. Page, M. Rüfenacht, M. Schönherr, and G. Watt, *LHAPDF6: parton density access in the LHC precision era*, Eur. Phys. J. C **75** no. 3, (2015) 132.

[42] *Official LHAPDF 6.2 PDF sets*, `https://lhapdf.hepforge.org/pdfsets`.

[43] R. Placakyte, *Parton Distribution Functions*, in *Proceedings, 31st International Conference on Physics in collisions (PIC 2011): Vancouver, Canada, August 28-September 1, 2011*. 2011.

[44] *Limits on anomalous triple and quartic gauge couplings*, `https://twiki.cern.ch/twiki/bin/view/CMSPublic/PhysicsResultsSMPaTGC`.

[45] The CMS collaboration, *Measurement of vector boson scattering and constraints on anomalous quartic couplings from events with four leptons and two jets in proton–proton collisions at s=13 TeV*, Physics Letters B **774** (2017) 682 – 705.

[46] The CMS collaboration, *A search for electroweak-induced production of Wgamma with two jets and constraints on anomalous quartic gauge couplings in pp collisions at sqrt(s) = 8 TeV*, Tech. Rep. CMS-PAS-SMP-14-011, CERN, Geneva, 1900.

[47] The CMS collaboration Collaboration,, *Search for WW$\gamma$ and WZ$\gamma$ production and constraints on anomalous quartic gauge couplings in pp collisions at* $\sqrt{s} = 8$ TeV, Phys. Rev. D **90** (2014) 032008.

[48] CMS Collaboration, T. C. collaboration, *Study of Vector Boson Scattering and Search for New Physics in Events with Two Same-Sign Leptons and Two Jets*, Phys. Rev. Lett. **114** (2015) 051801.

[49] T. C. collaboration, *Evidence for exclusive $\gamma\gamma \rightarrow W^+W^-$ production and constraints on anomalous quartic gauge couplings in pp collisions at $\sqrt{s} = 7$ and 8 TeV*, J. High Energy Phys. **08** (2016) 119.

[50] D. R. Green, P. Meade, and M.-A. Pleier, *Multiboson interactions at the LHC*, Rev. Mod. Phys. **89** no. 3, (2017) 035008.

[51] M. Cacciari, G. P. Salam, and G. Soyez, *The anti-ktjet clustering algorithm*, J. High Energy Phys. **2008** no. 04, (2008) 063–063.

[52] M. Cacciari, G. P. Salam, and G. Soyez, *FastJet user manual*, Eur. Phys. J. C **72** no. 3, (2012) 1896.

[53] *DressedLeptons*, `https://rivet.hepforge.org/code/dev/classRivet_1_1DressedLeptons.html`.

[54] *PDG-ID-Code*, `http://pdg.lbl.gov/2007/reviews/montecarlorpp.pdf`.

[55] *Kolmogorov Test*, `https://root.cern.ch/doc/v608/classTH1.html#aeadcf087afe6ba203bcde124cfabbee4`.

[56] *Description of Kolmogorov Test*, `https://www.itl.nist.gov/div898/handbook/eda/section3/eda35g.htm`.

[57] *Average Kolmogorov-Smirnov Distance between Two Distributions*, `http://www.aorda.com/html/PSG_Help_HTML/ksm_avg.htm`.

# Appendix

## APPENDIX A

# Additional Figures

## A.1 Matching Jets and Leptons for M5 Operator

The procedure for identifying and obtaining matching jets and matching leptons are very similar to each other. From the array of jets or leptons, the matching objects are obtained through the index of the lepton or the jet, that is being utilized for reconstructing the best candidate in each iteration for the candidate of respective boson.

The transverse momenta of these individual jets are shown in Figures A.1, A.2. From the invariant mass of the individual jets matched to hadronically decaying $W$ boson, as displayed in Figures A.3 and A.4. It is clear that the boosting of jets in EFT samples due to the inclusion of EFT operators causes imperfect resolution of jets by the $Antik_T$ algorithm. Therefore, it is necessary to prevent contamination of such low-$p_T$ jets during the reconstruction of $W$ boson candidate. This was reason behind a nuanced and stringent during both jet selection and reconstruction of $W$ boson. Alternatively, it would be beneficial to use a different algorithm than $Antik_T$ for resolution of jets.

The transverse momenta of the matching same flavor and opposite sign leptons are shown in Figures A.5 and A.6. The transverse momenta of the remaining lepton matched to leptonically decaying $W$ boson is shown in Figure A.7.

## A.2 Sensitivity of *WWZ* to Other Operators

The samples for M2 operator is defined as follows (similar to Table 4.1):

| Sample | Kinematic Cut | Color (In Figures) | Definition (in text) |
|---|---|---|---|
| SM | No Cut | Blue | `SM` |
| M2 | No Cut | Black | `M2-NoCut` |
| M2 | 3 TeV | Red | `M2-3TeVCut` |
| M2 | 1 TeV | Orange | `M2-1TeVCut` |

Table A.1: The table defining the samples for M2 operator after imposing kinematic cuts.

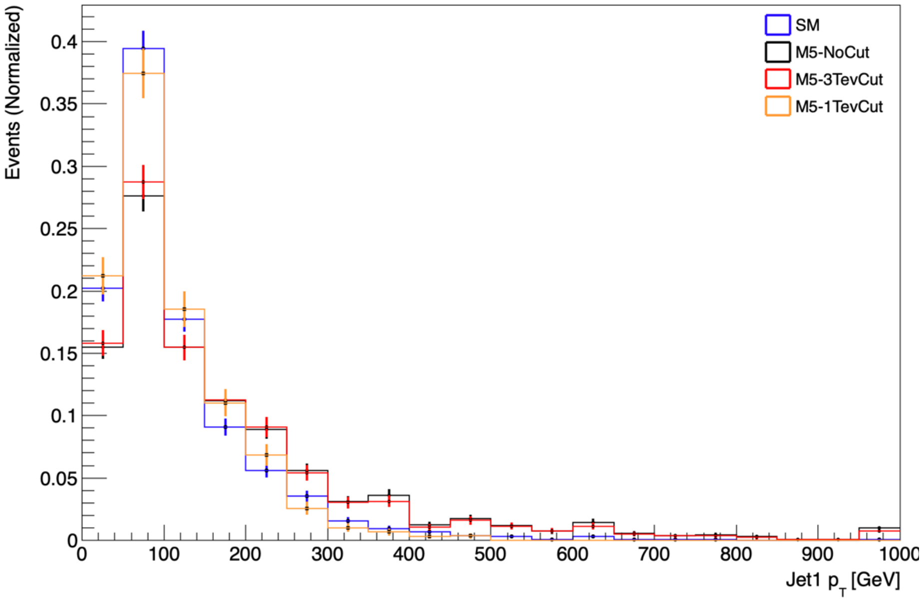


Figure A.1: The transverse momenta of the first matching jet for hadronically decaying $W$ boson for SM (in blue), `M5-NoCut` (in black), `M5-3TeVCut` (in red) and `M5-1TeVCut` (in orange) samples, with only the statistical uncertainties being displayed. The last bin contains overflow.

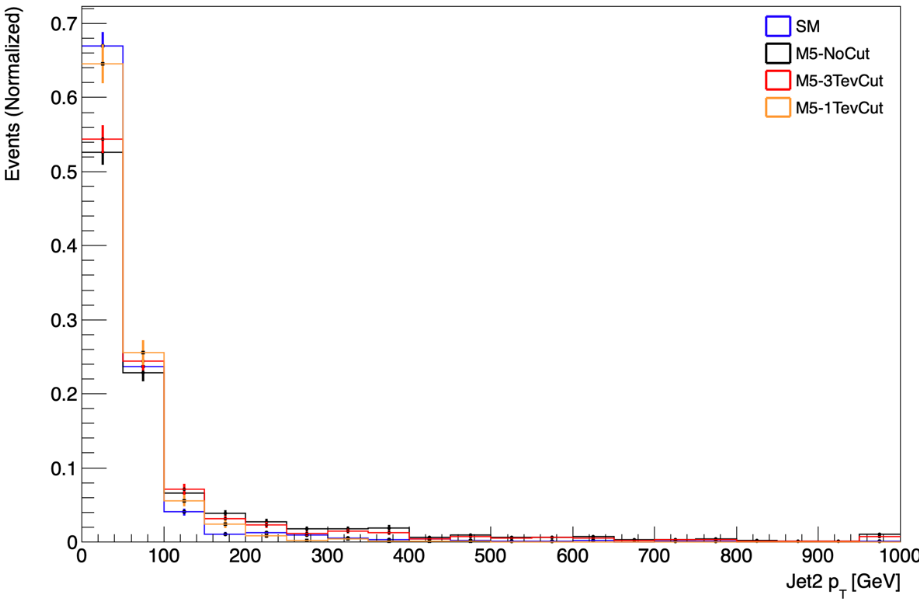


Figure A.2: The transverse momenta of the second matching jet for hadronically decaying $W$ boson for SM (in blue), `M5-NoCut` (in black), `M5-3TeVCut` (in red) and `M5-1TeVCut` (in orange) samples, with only the statistical uncertainties being displayed.The last bin contains overflow.

## A.3 Sensitivity of *WWZ* from T5 Operator

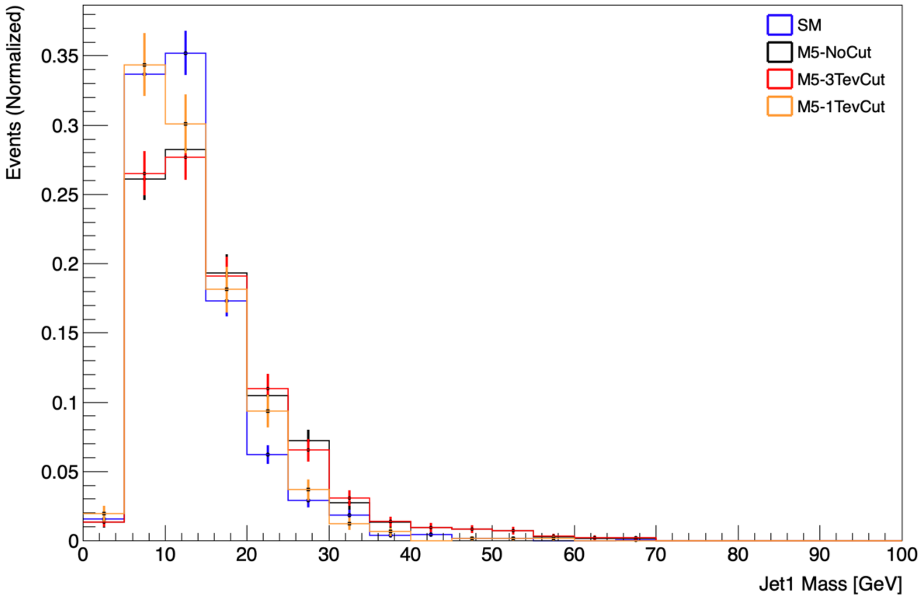


Figure A.3: The invariant mass of the first matching jet for hadronically decaying $W$ boson for SM (in blue), `M5-NoCut` (in black), `M5-3TeVCut` (in red) and `M5-1TeVCut` (in orange) samples, with only the statistical uncertainties being displayed. The last bin contains overflow.

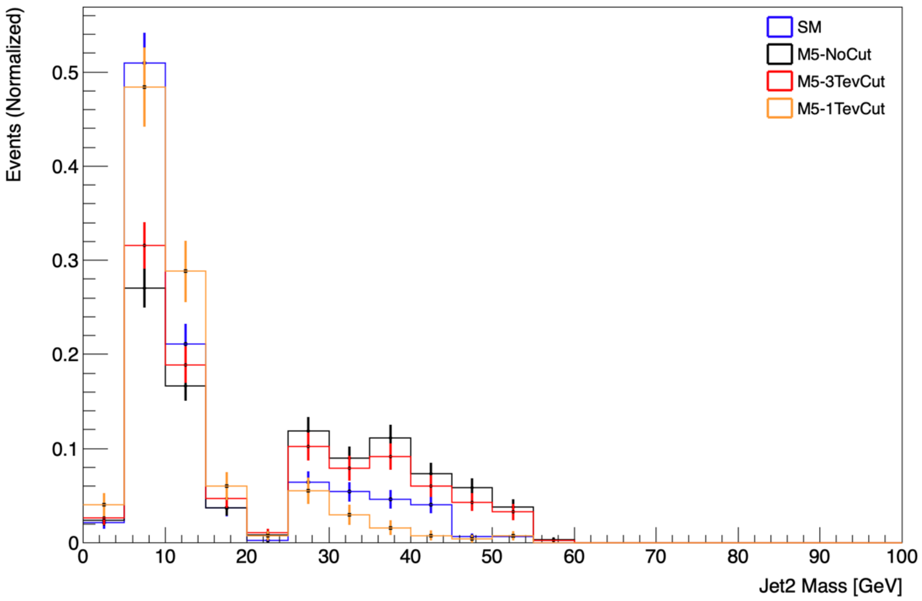


Figure A.4: The invariant mass of the second matching jet for hadronically decaying $W$ boson for SM (in blue), `M5-NoCut` (in black), `M5-3TeVCut` (in red) and `M5-1TeVCut` (in orange) samples, with only the statistical uncertainties being displayed. The last bin contains overflow.

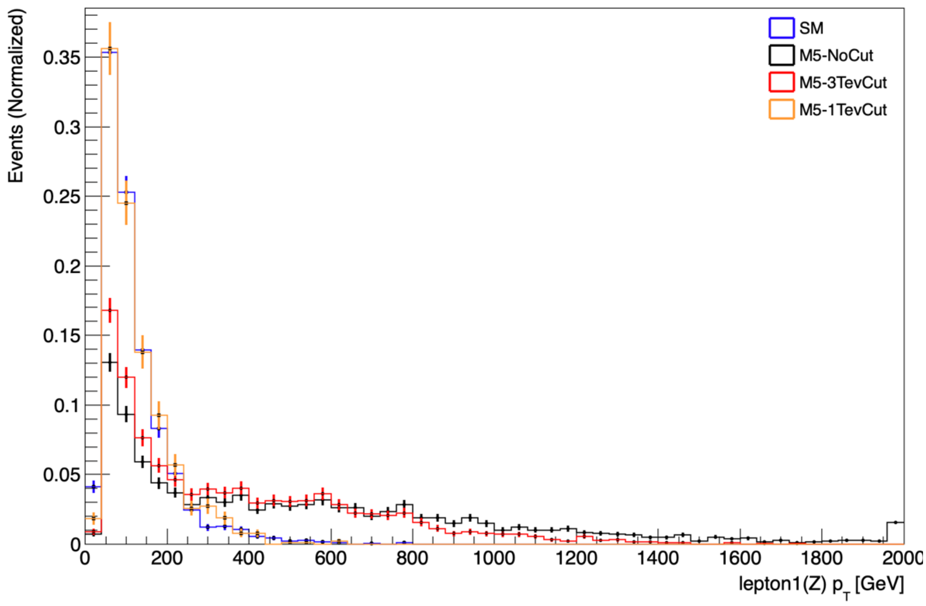


Figure A.5: The transverse momenta of the first matching same flavor, opposite sign lepton for leptonically decaying $Z$ boson for SM (in blue), `M5-NoCut` (in black), `M5-3TeVCut` (in red) and `M5-1TeVCut` (in orange) samples, with only the statistical uncertainties being displayed. The last bin contains overflow.

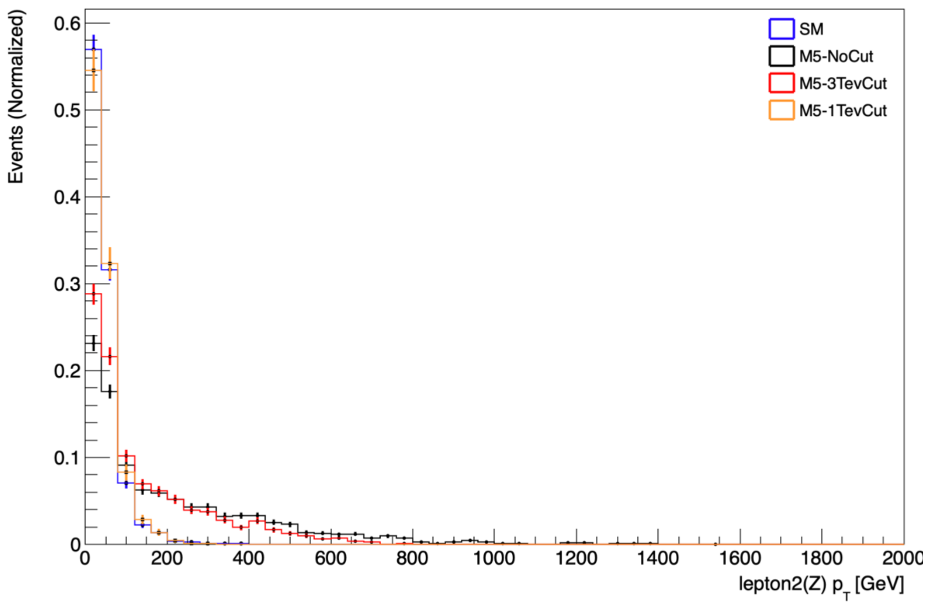


Figure A.6: The transverse momenta of the second matching same flavor, opposite sign lepton for leptonically decaying $Z$ boson for SM (in blue), `M5-NoCut` (in black), `M5-3TeVCut` (in red) and `M5-1TeVCut` (in orange) samples, with only the statistical uncertainties being displayed. The last bin contains overflow.

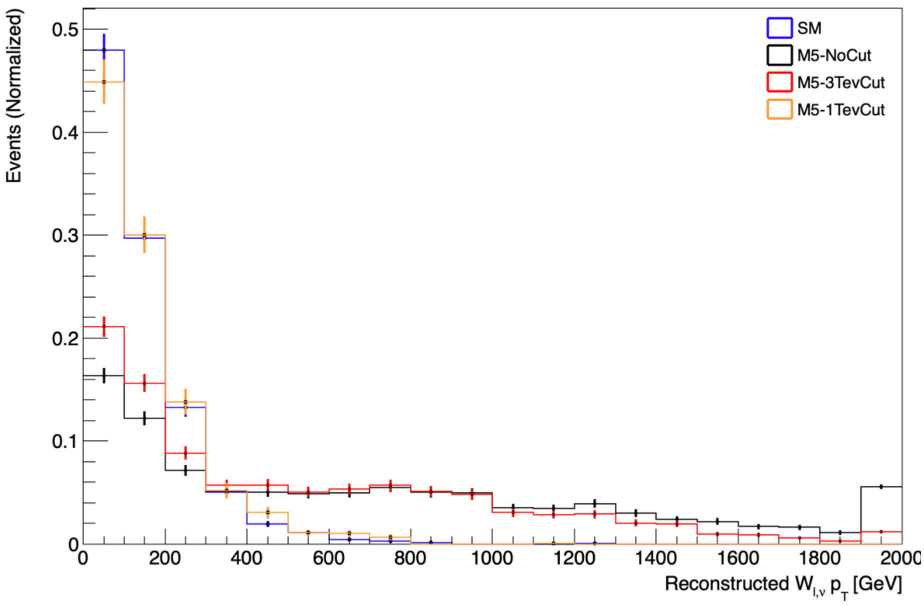


Figure A.7: The transverse momenta of the other remaining lepton for leptonically decaying $W$ boson for SM (in blue), `M5-NoCut` (in black), `M5-3TeVCut` (in red) and `M5-1TeVCut` (in orange) samples, with only the statistical uncertainties being displayed. The last bin contains overflow.

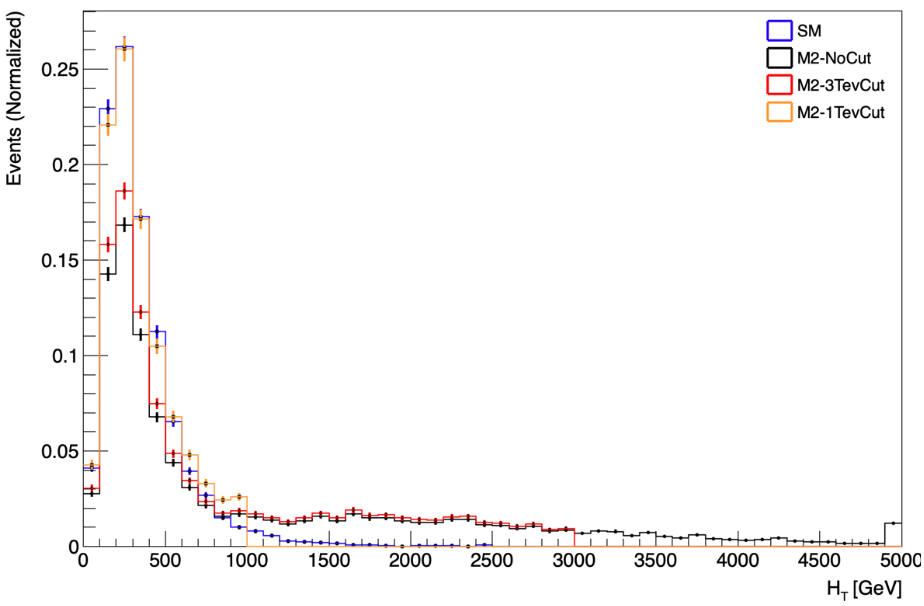


Figure A.8: $H_T$ for SM (in blue), `M2-NoCut` (in black), `M2-3TeVCut` (in red) and `M2-1TeVCut` (in orange) samples, with only the statistical uncertainties being displayed. The last bin contains the overflow. The events are normalized to one.

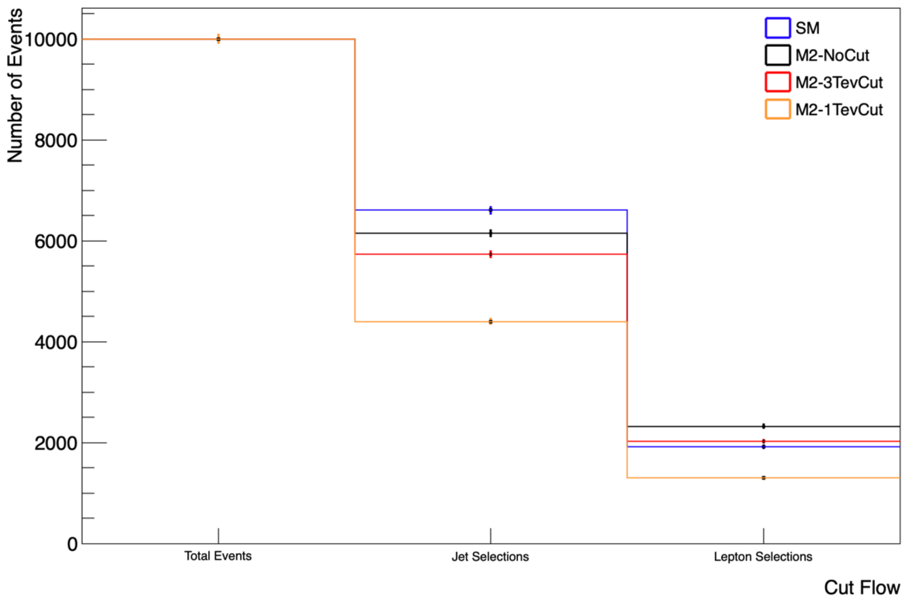


Figure A.9: The total number of events in the first bin, events passing jet constraints in the second bin and after lepton requirements in the third bin for `SM` (in blue), `M2-NoCut` (in black), `M2-3TeVCut` (in red) and `M2-1TeVCut` (in orange) samples, with only the statistical uncertainties being displayed.

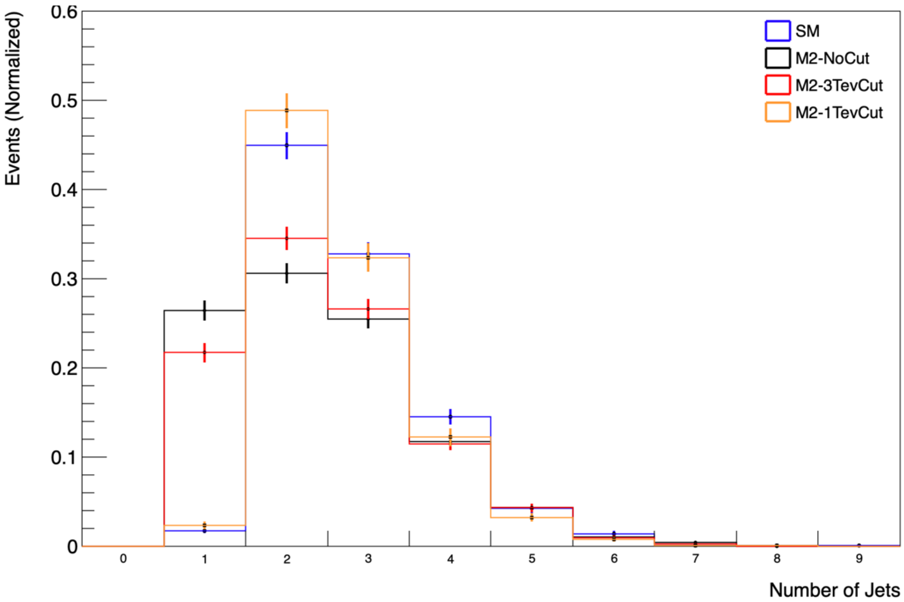


Figure A.10: The number of jets after requiring at least one jet and $p_{T,jet} > 25$ GeV for `SM` (in blue), `M2-NoCut` (in black), `M2-3TeVCut` (in red) and `M2-1TeVCut` (in orange) samples, with only the statistical uncertainties being displayed. The events are normalized to one.

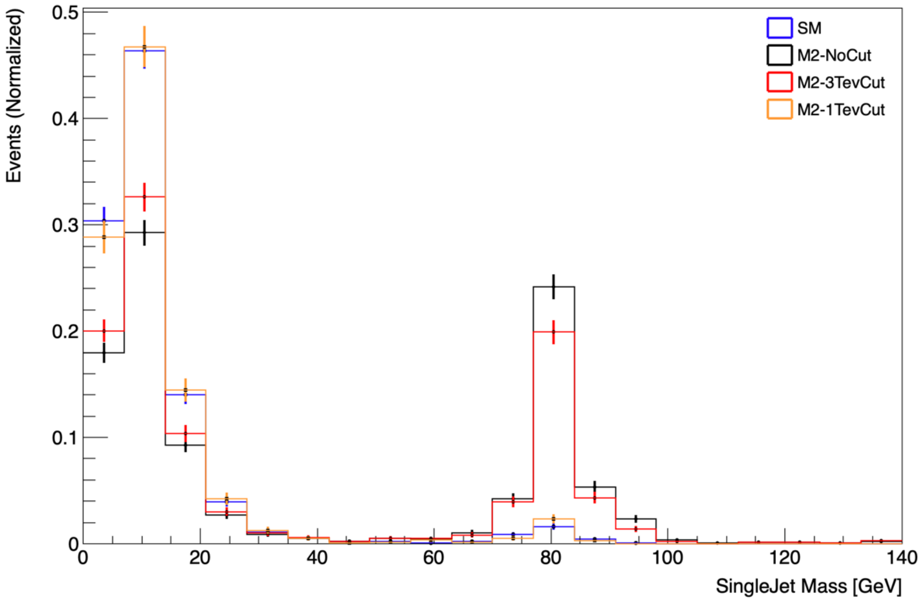


Figure A.11: The invariant mass of a single-jet after requiring $p_{T,jet} > 25$ GeV for `SM` (in blue), `M2-NoCut` (in black), `M2-3TeVCut` (in red) and `M2-1TeVCut` (in orange) samples, with only the statistical uncertainties being displayed. The last bin contains overflow. The events are normalized to one.

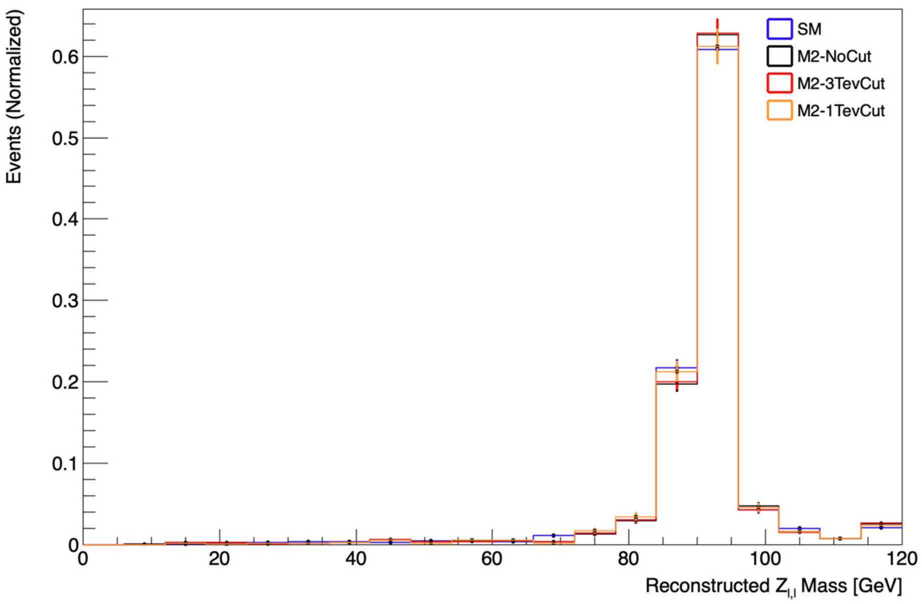


Figure A.12: The invariant mass of all possible pairs of opposite-sign-same-flavored leptons, for `SM` (in blue), `M2-NoCut` (in black), `M2-3TeVCut` (in red) and `M2-1TeVCut` (in orange) samples, with only the statistical uncertainties being displayed. The events are normalized to one.

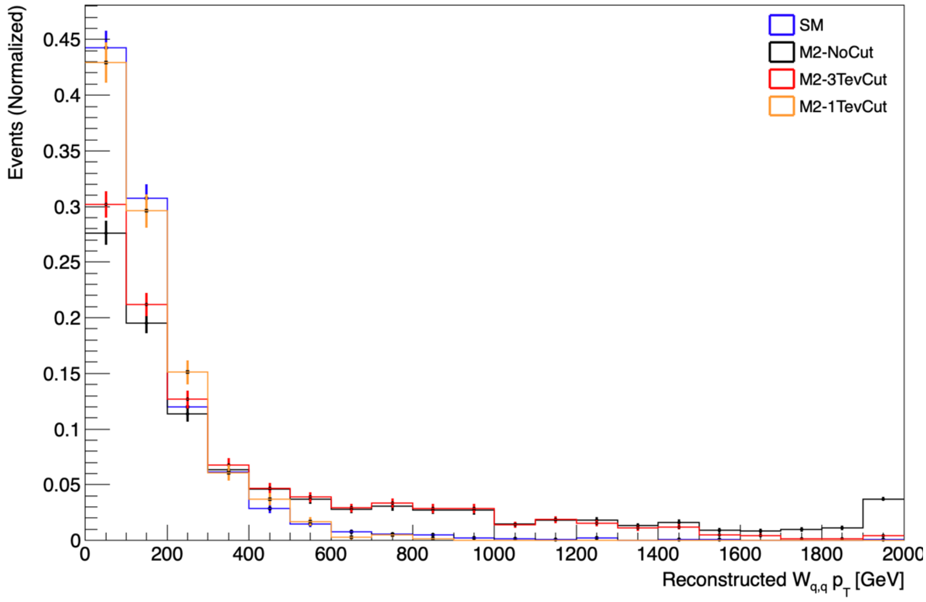


Figure A.13: The transverse momenta of the candidates for hadronically decaying $W$ boson for `SM` (in blue), `M2-NoCut` (in black), `M2-3TeVCut` (in red) and `M2-1TeVCut` (in orange) samples, with only the statistical uncertainties being displayed. The last bin contains overflow. The events are normalized to one.

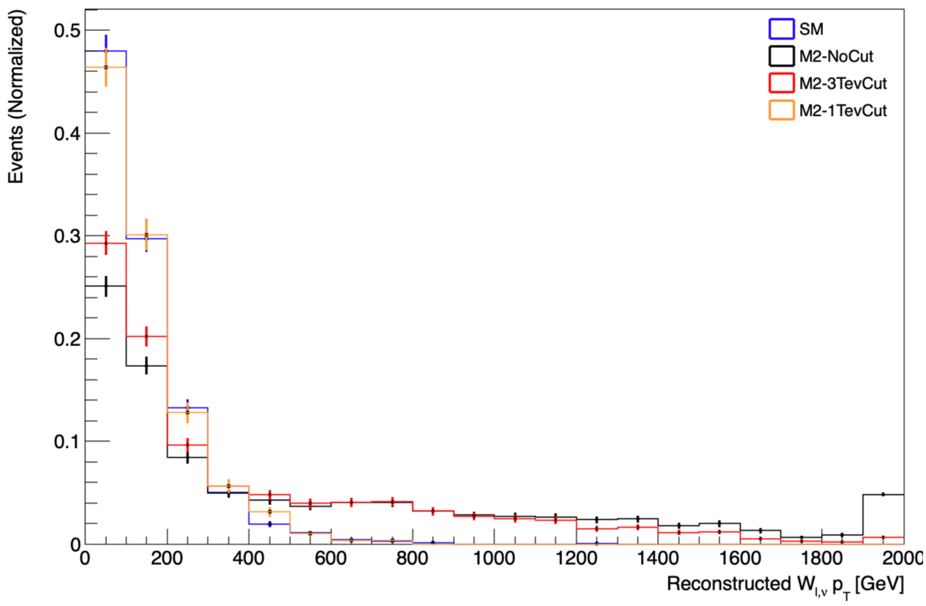


Figure A.14: The transverse momenta of the candidates for leptonically decaying $W$ boson for `SM` (in blue), `M2-NoCut` (in black), `M2-3TeVCut` (in red) and `M2-1TeVCut` (in orange) samples, with only the statistical uncertainties being displayed. The last bin contains overflow. The events are normalized to one.

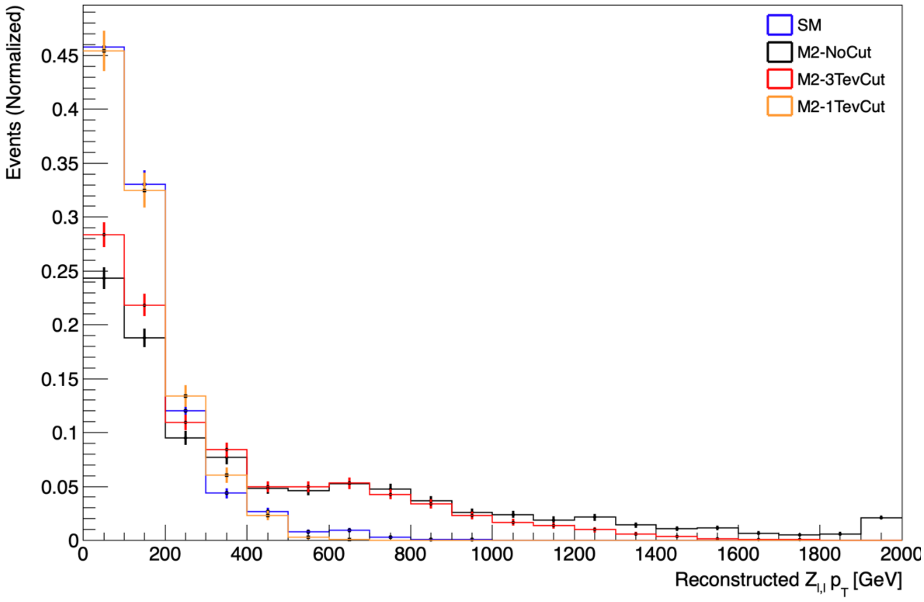


Figure A.15: The transverse momenta of the candidates for leptonically decaying $Z$ boson for `SM` (in blue), `M2-NoCut` (in black), `M2-3TeVCut` (in red) and `M2-1TeVCut` (in orange) samples, with only the statistical uncertainties being displayed. The last bin contains overflow. The events are normalized to one.

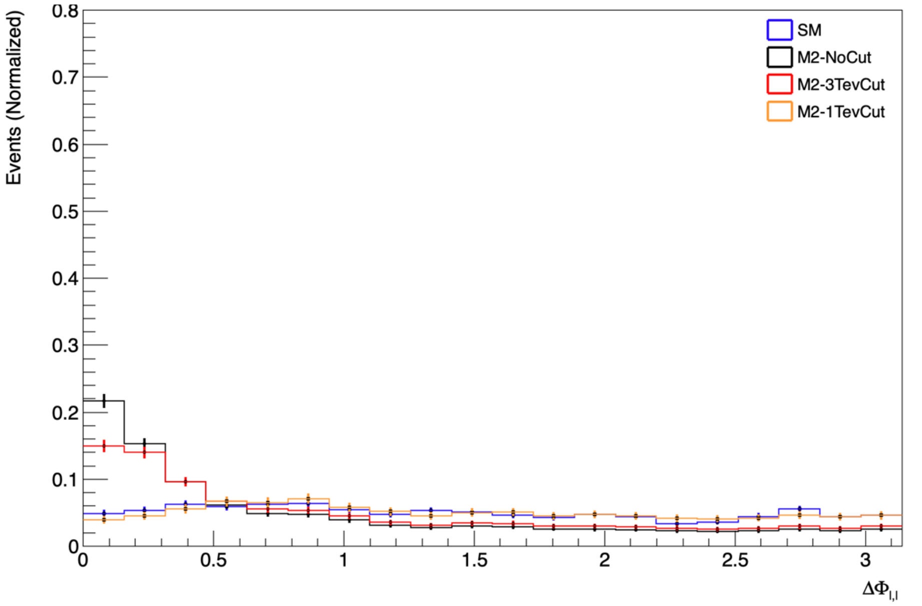


Figure A.16: The $\Delta\phi$ between between pair of opposite sign same flavor leptons for `SM` (in blue), `M2-NoCut` (in black), `M2-3TeVCut` (in red) and `M2-1TeVCut` (in orange) samples, with only the statistical uncertainties being displayed. The events are normalized to one.

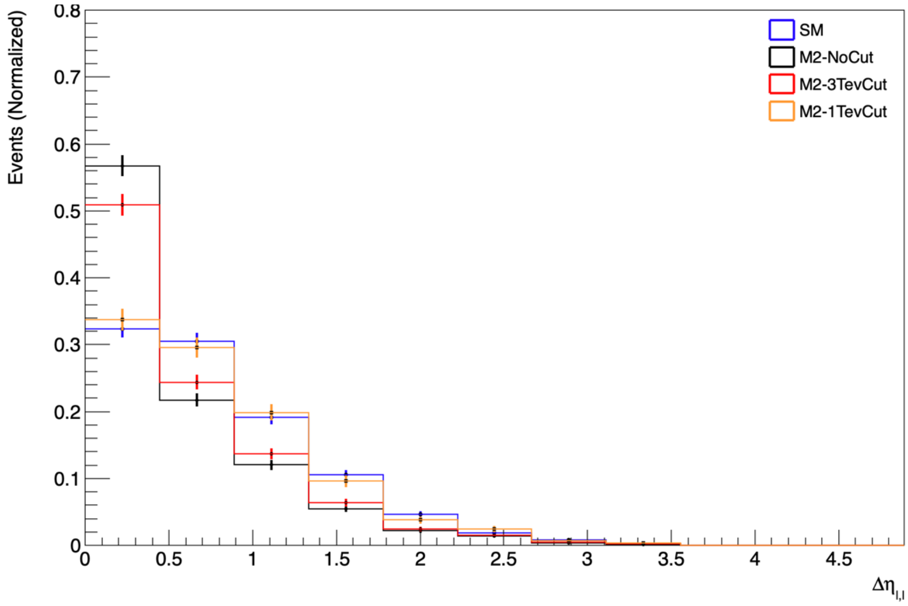


Figure A.17: The $\Delta\eta$ between between pair of opposite sign same flavor leptons for `SM` (in blue), `M5-NoCut` (in black), `M5-3TeVCut` (in red) and `M5-1TeVCut` (in orange) samples, with only the statistical uncertainties being displayed. The events are normalized to one.

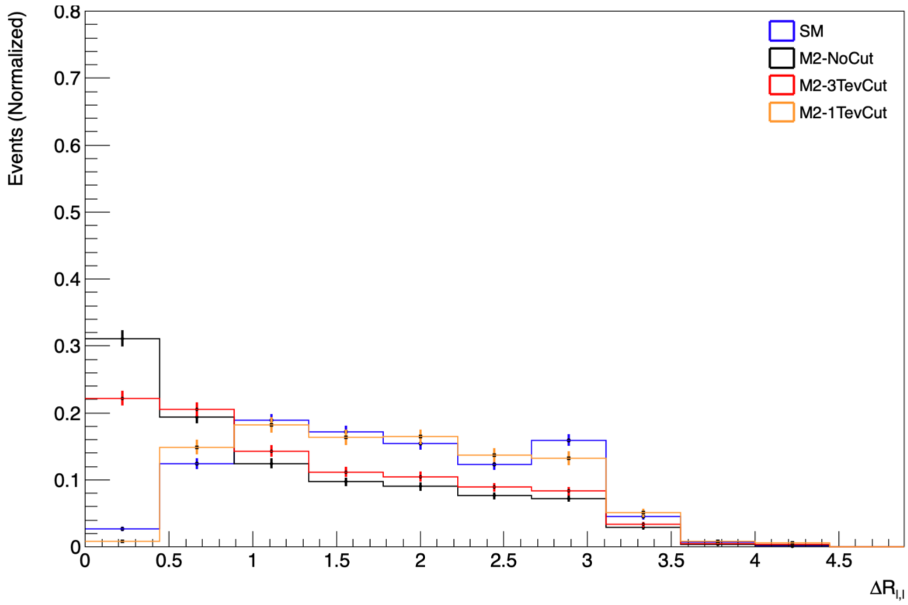


Figure A.18: The ΔR between between pair of opposite sign same flavor leptons for `SM` (in blue), `M5-NoCut` (in black), `M5-3TeVCut` (in red) and `M5-1TeVCut` (in orange) samples, with only the statistical uncertainties being displayed. The events are normalized to one.

| Sample | Kinematic Cut | Color (In Figures) | Definition (in text) |
|---|---|---|---|
| SM | No Cut | Blue | `SM` |
| T5 | No Cut | Black | `T5-NoCut` |
| T5 | 3 TeV | Red | `T5-3TeVCut` |
| T5 | 1 TeV | Orange | `T5-1TeVCut` |

Table A.2: The table defining the samples for T5 operator after imposing kinematic cuts.

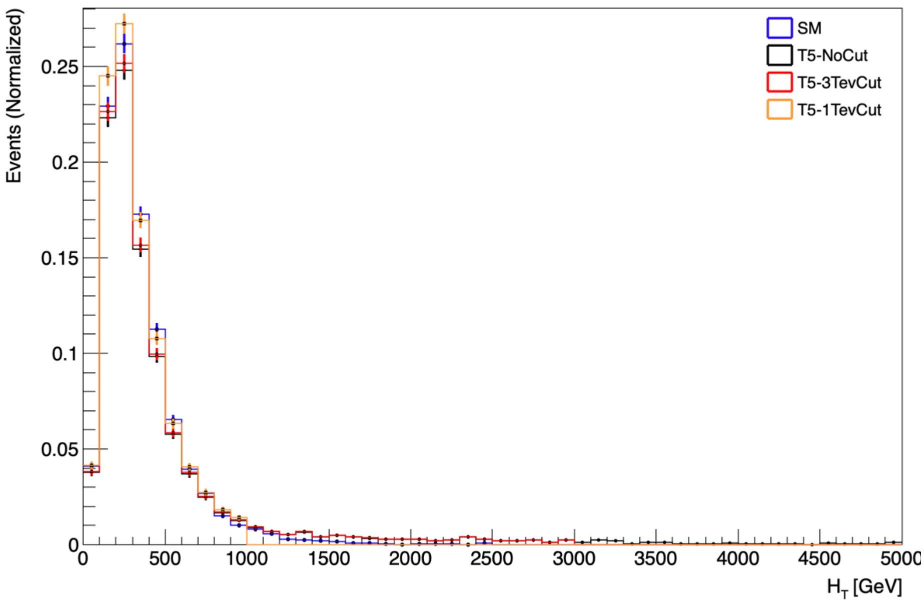


Figure A.19: $H_T$ for SM (in blue), `T5-NoCut` (in black), `T5-3TeVCut` (in red) and `T5-1TeVCut` (in orange) samples, with only the statistical uncertainties being displayed. The last bin contains the overflow. The events are normalized to one.

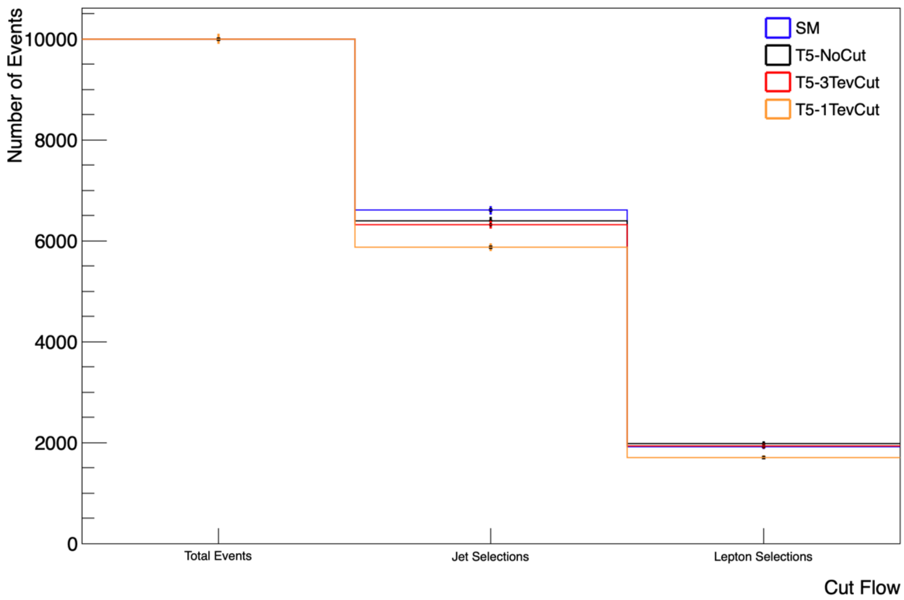


Figure A.20: The total number of events in the first bin, events passing jet constraints in the second bin and after lepton requirements in the third bin for `SM` (in blue), `T5-NoCut` (in black), `T5-3TeVCut` (in red) and `T5-1TeVCut` (in orange) samples, with only the statistical uncertainties being displayed.

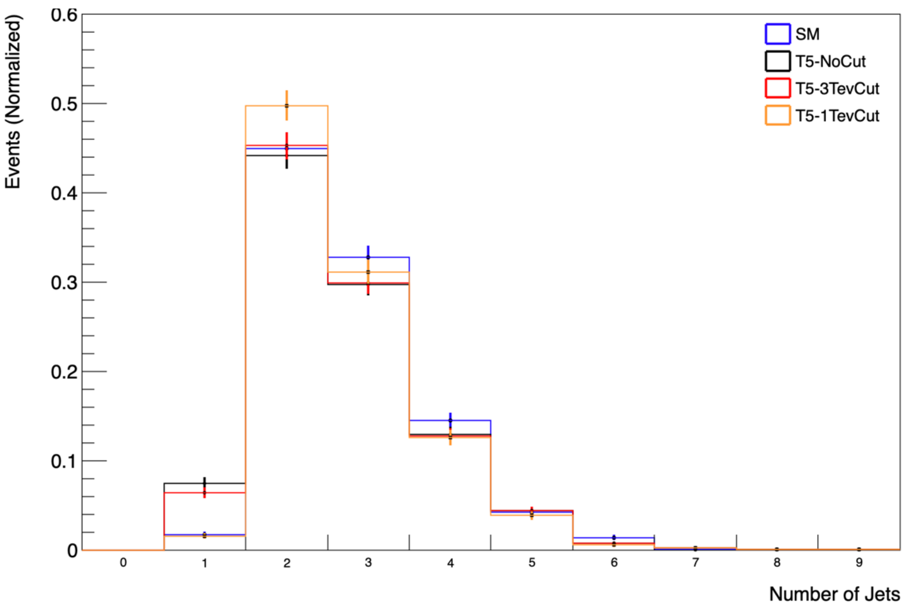


Figure A.21: The number of jets after requiring at least one jet and $p_{T,jet} > 25$ GeV for `SM` (in blue), `T5-NoCut` (in black), `T5-3TeVCut` (in red) and `T5-1TeVCut` (in orange) samples, with only the statistical uncertainties being displayed. The events are normalized to one.

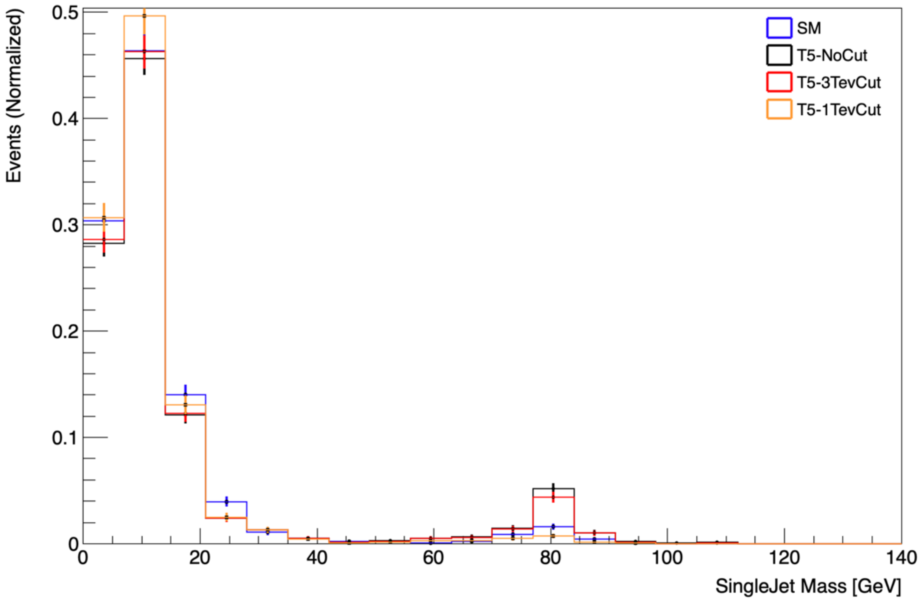


Figure A.22: The invariant mass of a single-jet after requiring $p_{T,jet} > 25$ GeV for `SM` (in blue), `T5-NoCut` (in black), `T5-3TeVCut` (in red) and `T5-1TeVCut` (in orange) samples, with only the statistical uncertainties being displayed. The last bin contains overflow. The events are normalized to one.

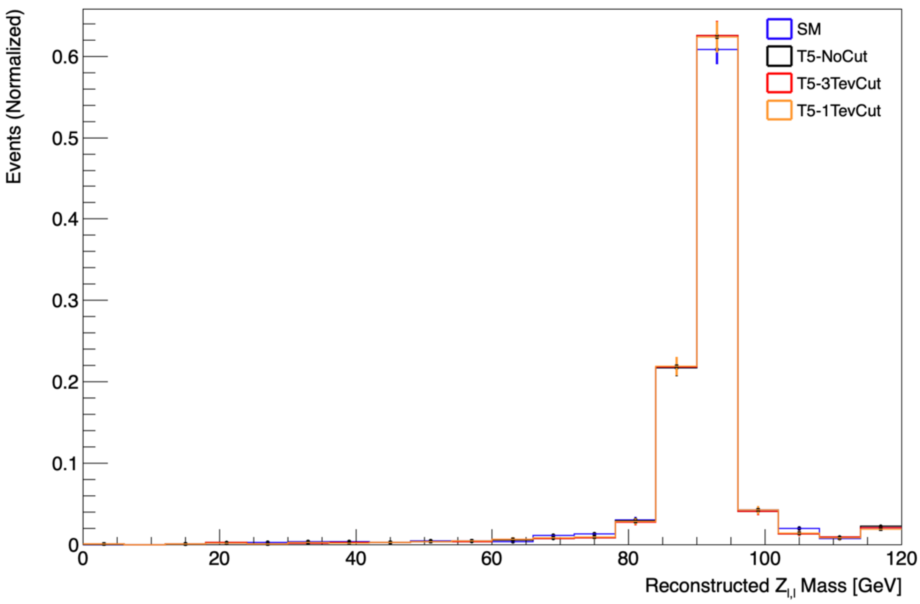


Figure A.23: The invariant mass of all possible pairs of opposite-sign-same-flavored leptons, for `SM` (in blue), `T5-NoCut` (in black), `T5-3TeVCut` (in red) and `T5-1TeVCut` (in orange) samples, with only the statistical uncertainties being displayed. The events are normalized to one.

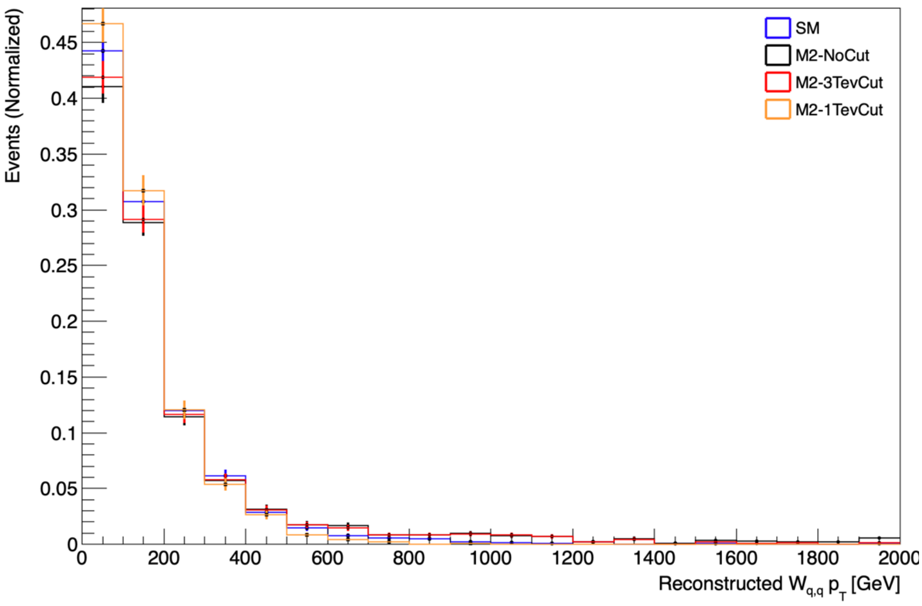


Figure A.24: The transverse momenta of the candidates for hadronically decaying $W$ boson for `SM` (in blue), `T5-NoCut` (in black), `T5-3TeVCut` (in red) and `T5-1TeVCut` (in orange) samples, with only the statistical uncertainties being displayed. The last bin contains overflow. The events are normalized to one.

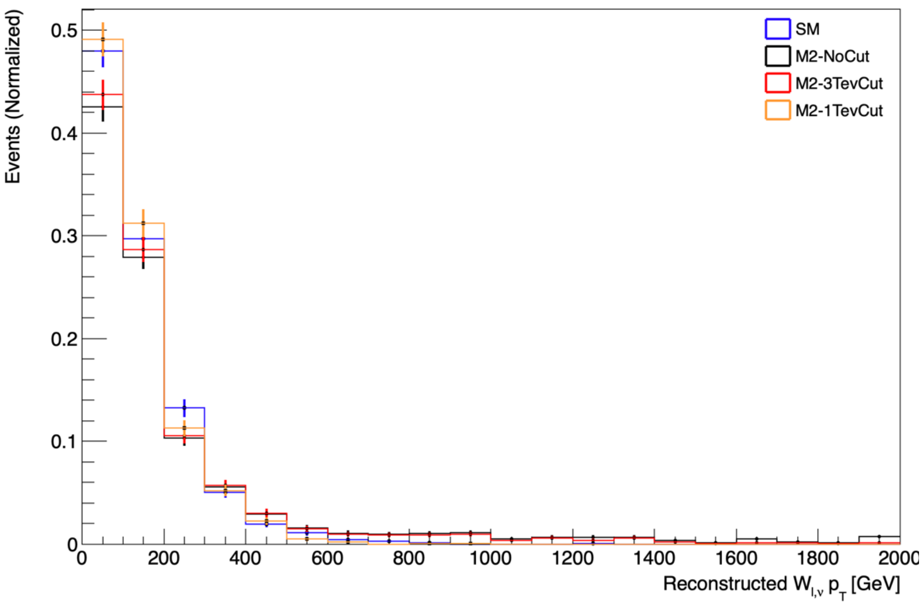


Figure A.25: The transverse momenta of the candidates for leptonically decaying $W$ boson for `SM` (in blue), `T5-NoCut` (in black), `T5-3TeVCut` (in red) and `T5-1TeVCut` (in orange) samples, with only the statistical uncertainties being displayed. The last bin contains overflow. The events are normalized to one.

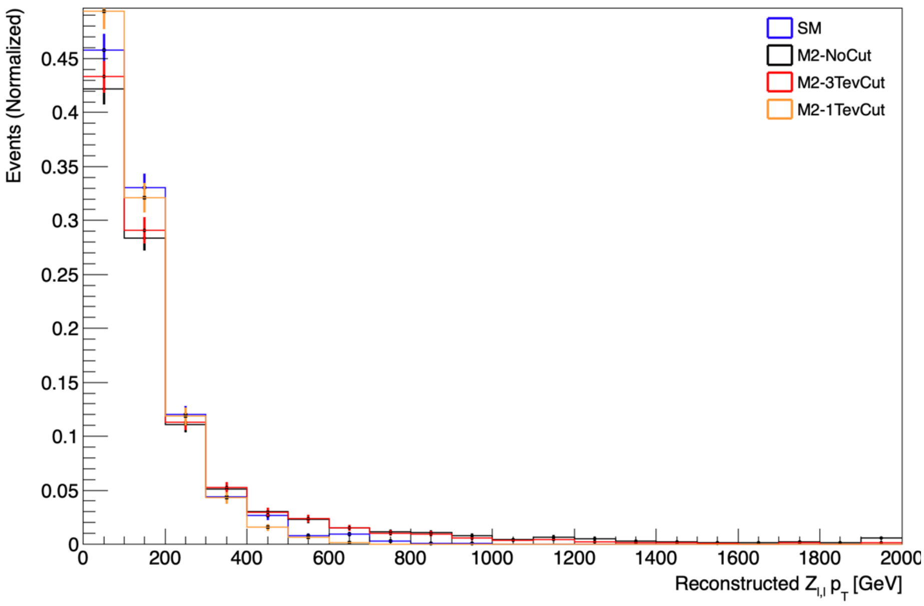


Figure A.26: The transverse momenta of the candidates for leptonically decaying $Z$ boson for `SM` (in blue), `T5-NoCut` (in black), `T5-3TeVCut` (in red) and `T5-1TeVCut` (in orange) samples, with only the statistical uncertainties being displayed. The last bin contains overflow. The events are normalized to one.

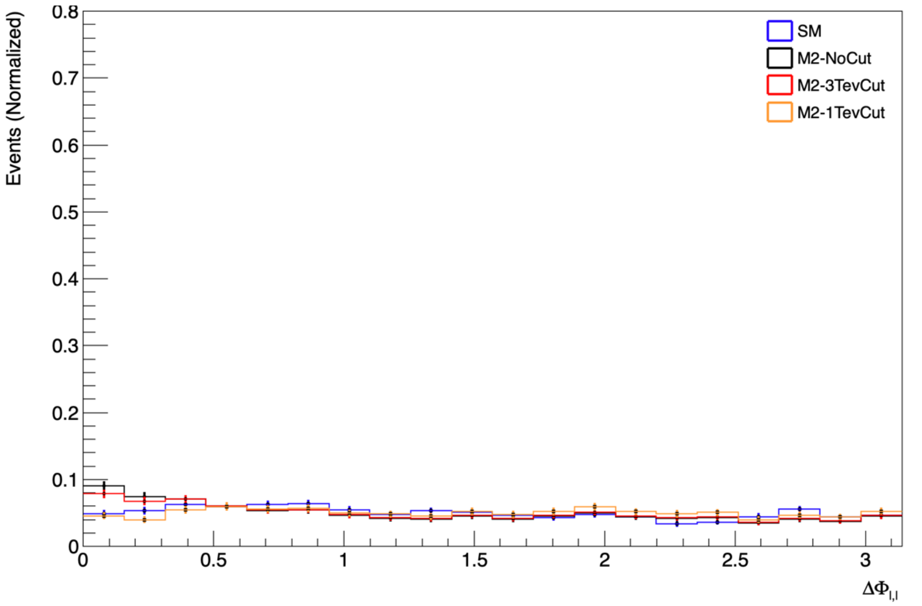


Figure A.27: The $\Delta\phi$ between between pair of opposite sign same flavor leptons for `SM` (in blue), `T5-NoCut` (in black), `T5-3TeVCut` (in red) and `T5-1TeVCut` (in orange) samples, with only the statistical uncertainties being displayed. The events are normalized to one.

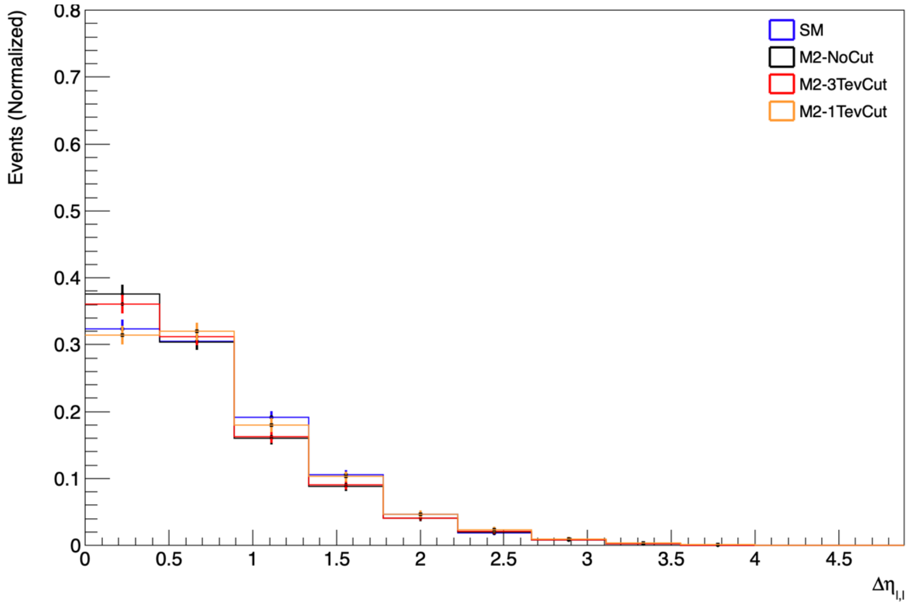


Figure A.28: The $\Delta\eta$ between between pair of opposite sign same flavor leptons for `SM` (in blue), `T5-NoCut` (in black), `T5-3TeVCut` (in red) and `T5-1TeVCut` (in orange) samples, with only the statistical uncertainties being displayed. The events are normalized to one.

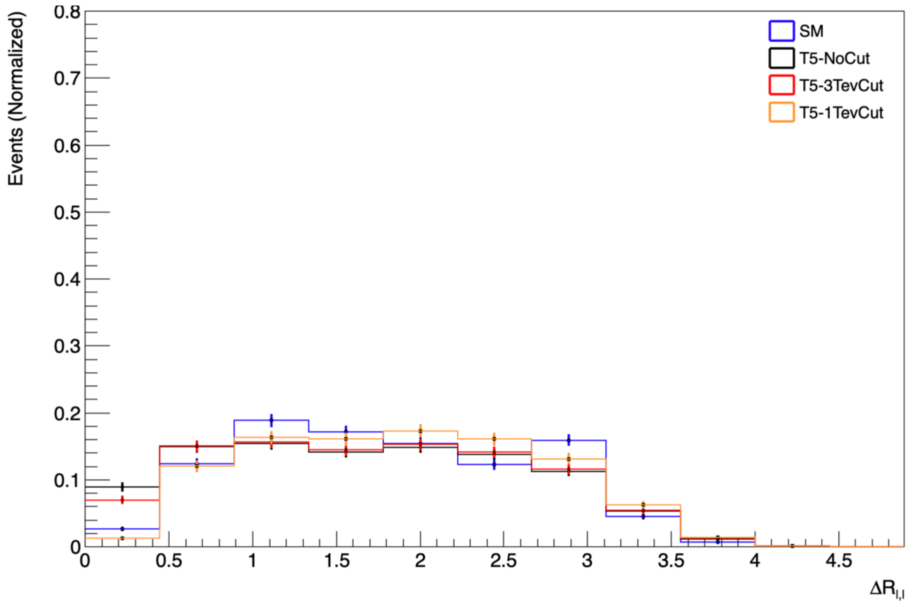


Figure A.29: The ΔR between between pair of opposite sign same flavor leptons for `SM` (in blue), `T5-NoCut` (in black), `T5-3TeVCut` (in red) and `T5-1TeVCut` (in orange) samples, with only the statistical uncertainties being displayed. The events are normalized to one.

APPENDIX B

# Scripts and Job Options (JO)

1. The setup shell script is available at : https://gitlab.cern.ch/ngubbi/aQGC/blob/master/setup.sh
2. The JO for generation of events (T0 operator as an example) is available at :https://gitlab.cern.ch/ngubbi/aQGC/blob/master/jo_T0.py
3. The JO for generation of events on the grid is available at : https://gitlab.cern.ch/ngubbi/aQGC/blob/master/aQGC-Rivet.py
4. The run card is available at : https://gitlab.cern.ch/ngubbi/aQGC/blob/master/new_run_card.dat
5. The parameter card is available at : https://gitlab.cern.ch/ngubbi/aQGC/blob/master/param_card_T0.dat
6. The script for Rivet routine is available at : https://gitlab.cern.ch/ngubbi/aQGC/blob/master/WWZ-Carlo.cc
7. The script for JO for running rivet locally is available at : https://gitlab.cern.ch/ngubbi/aQGC/blob/master/RunLocalRivet.py

# List of Figures

# List of Tables